3-10-2008

Extending CFD Modeling to Near-Continuum Flows Using Enhanced Thermophysical Modeling

Abram E. Claycomb

Extending CFD Modeling to Near-Continuum Flows Using Enhanced Thermophysical Modeling

THESIS

Abram E. Claycomb, Captain, USAF

AFIT/GAE/ENY/08-M04

DEPARTMENT OF THE AIR FORCE
AIR UNIVERSITY

AIR FORCE INSTITUTE OF TECHNOLOGY

Wright-Patterson Air Force Base, Ohio

The views expressed in this thesis are those of the author and do not reflect the official policy or position of the United States Air Force, Department of Defense, or the United States Government.

AFIT/GAE/ENY/08-M04

Extending CFD Modeling to Near-Continuum Flows Using Enhanced Thermophysical Modeling

THESIS

Presented to the Faculty

Department of Aeronautics and Astronautics

Graduate School of Engineering and Management

Air Force Institute of Technology

Air University

Air Education and Training Command

In Partial Fulfillment of the Requirements for the

Degree of Master of Science in Aeronautical Engineering

Abram E. Claycomb, BS

Captain, USAF

March 2008

AFIT/GAE/ENY/08-M04

Extending CFD Modeling to Near-Continuum Flows Using Enhanced Thermophysical Modeling

Abram E. Claycomb, BS
Captain, USAF

Approved:

/signed/	10 March 2008
Dr. Robert Greendyke (Chairman)	date
/signed/	10 March 2008
Dr. José Camberos (Member)	date
/signed/	10 March 2008
Lt Col Raymond Maple (Member)	date
/signed/	10 March 2008
Maj Richard Branam (Member)	date

AFIT/GAE/ENY/08-M04

Abstract

The constitutive relations found in traditional Navier-Stokes-based computational fluid dynamics solvers are known to be limited in altitude. The presence of nonequilibrium phenomena beyond what these methods are able to predict becomes more prevalent at higher altitudes, or increasing Knudsen number. The bulk viscosity, normally assumed to be zero in most computational fluid dynamics applications, is examined as a means of increasing the range of applicability of computational fluid dynamics. The bulk viscosity model used was from recent calculations available in the literature, from a new anisotropic potential energy surface, and is restricted to temperatures below 2000 K. The normal shock problem was solved for Mach numbers up to ten, using the bulk viscosity model. The bulk viscosity provided improvement in the agreement with observations of normal shock thickness for Mach numbers up to ten. Two axisymmetric, experimentally observed flows were solved with and without the bulk viscosity, and compared to DSMC solutions of a previous work. Improvement of surface heat transfer agreement with observation was found for a hollow-cylinder flare axisymmetric body. Improvement of separation point prediction was found for an axisymmetric double cone.

Acknowledgements

The author would like to thank Dr. Robert Greendyke for his guidance on this project. The sponsorship of this work by Dr. José Camberos, and funding from AFRL/RBSD is gratefully acknowledged. The helpful suggestions and assistance of Lt Col Maple during this work are also gratefully acknowledged. The author would like to thank Lt Ryan Carr for his encouragement and assistance throughout this project. Finally, the author gratefully acknowledges the sacrifice of his wife and son during this course of study.

Abram E. Claycomb

Table of Contents

Page

List of Figures

List of Tables

List of Abbreviations

Extending CFD Modeling to Near-Continuum Flows Using Enhanced Thermophysical Modeling

I. Introduction

THE concepts of maneuver and mass have been redefined by the sheer speed air and space vehicles have brought to warfare. In this area, major technological battles have played out for speed and range. The advantage afforded by speed in the battlespace is well known [3:9–11; 4:8]. Air Force Chief of Staff, General Michael Moseley, puts speed in the context of the greater mission of the service:

> The Air Force exists to fly, fight and win—to achieve strategic, operational and tactical objectives—unhindered by time, distance or geography. . . . We provide *Global Vigilance, Global Reach, and Global Power*. . .
> - ***Global Vigilance*** is the persistent, world-wide capability to keep an unblinking eye on any entity. . .
> - ***Global Reach*** is the ability to move, supply, or position assets—with unrivaled velocity and precision—anywhere on the planet
> - ***Global Power*** is the ability to hold at risk or strike any target, anywhere in the world, and project swift, decisive, precise effects.
>
> [5:1]

Hypersonic vehicles, which move through the atmosphere much faster than the speed of sound, have provided *Global Vigilance* through space launch, and *Global Power* through intercontinental ballistic missiles. Both these applications have very high-speed, short-duration flights, and depend on rocket propulsion. As successful as these types of vehicle are, there has long been a quest for air-breathing hypersonic vehicles. As imagined by designers, these vehicles could be operated from runways or underwing stores stations, not launchpads. Global power, in providing more precise effects than the strategic counterpart mentioned above, may become the domain of these new vehicles.

Global vigilance may be augmented by hypersonic vehicles. With peer-competitors flexing their muscles in space, the Chief of Staff has this to say: "We need to deploy

high-altitude, high-speed, air-breathing systems to mitigate risks to space-based capabilities." [5:8]. The high-altitude, high-speed flight regime is the focus of this work.

In producing hypersonic vehicles, design activities, computer simulations and analyses are performed. Ground tests are conducted, matching as many of the proposed flight conditions as possible. Actual flight research, when budgeted, is performed to validate analytical and computer models and reduce their uncertainty.

The importance of research to develop this technology, and more importantly to understand the physical phenomena associated with flying at high speeds and high altitudes cannot be stressed enough. The United States Air Force (USAF) must be able to honestly assess the effectiveness, cost and risk of proposed investments in hypersonic vehicles and weapons. Through these research programs, data for testing flow models are obtained, and better models can be built. Better models provide more accurate predictions. More accurate predictions can reduce risk, uncertainty, and cost. Models which agree with a particular set of experiments or analysis should not be treated as finished works. They should instead be subject to refinement, and re-validation, especially in cases where vehicles begin to be used beyond their original operating envelope, or beyond their expected life.

Now is an exciting time for hypersonics research in the USAF. The X-51, a vehicle designed to demonstrate the feasibility of supersonic combustion, a hypersonics-enabling technology, is being prepared for flight test. The USAF is leading the world in hypersonics research. In fact, at the 46th Aerospace Sciences Meeting of the American Institute of Aeronautics and Astronautics (AIAA), eight hypersonics-related sessions were chaired by Air Force personnel [6]. A joint Australian-USAF program, the Hypersonics International Flight Research Experimentation (HiFIRE), is currently in ground testing, and will be flown within the year. Ground testing done at National Air and Space Administration (NASA) Langley Research Center (LaRC) and the Calspan University of Buffalo Research Center (CUBRC), combined with computational fluid dynamics, is being used to determine the geometry of the flight test vehicle [7].

1.1 Continuum Assumption and Altitude

Most aerodynamicists are used to thinking of air as a continuous medium, infinitely divisible into smaller pieces with identical behavior. The reality is, in fact, much more complicated. Air is made up of N_2, O_2, and smaller amounts of CO_2, Ar, and other 'trace' components. Transfer of mass, momentum, and energy in various forms happen on a molecular, and therefore discrete, level. Continuum representations are built from the microscopic, making assumptions and simplifications about the collisional processes and molecular energy transfer.

A "rough guide" [2:665] for the definitions of the flight regimes discussed above can be found in Table 1

Table 1: Rarefied Flow Regimes [2:665]

Flight regime	Range
collisionless, near-collisionless:	$10.0 \leq Kn$
transition:	$0.1 \leq Kn \leq 10.0$
near-hydrodynamic:	$0.01 \leq Kn \leq 0.1$
hydrodynamic:	$Kn \leq 0.01$

By this guide, using body dimension as the basis for Kn, the present work will be confined to the hydrodynamic regime. Thus, this work, being a small step toward the near-continuum regime will start from within the continuum regime. The definition of high Knudsen number will be $Kn \geq 0.001$. The reason for this definition will be explained in more detail in Chapter II. Figure 1 depicts mean free path, as calculated from the 1976 US Standard Atmosphere as a function of altitude. With this figure, and a local length scale, a Knudsen number can be determined.

1.2 Near-Continuum Flow Considerations

The continuum model, traditionally used from the earth's surface to around 80km, is based on the familiar continuum formulations of conservation of mass, momentum and energy, hereinafter referred to collectively as the Navier-Stokes equations.

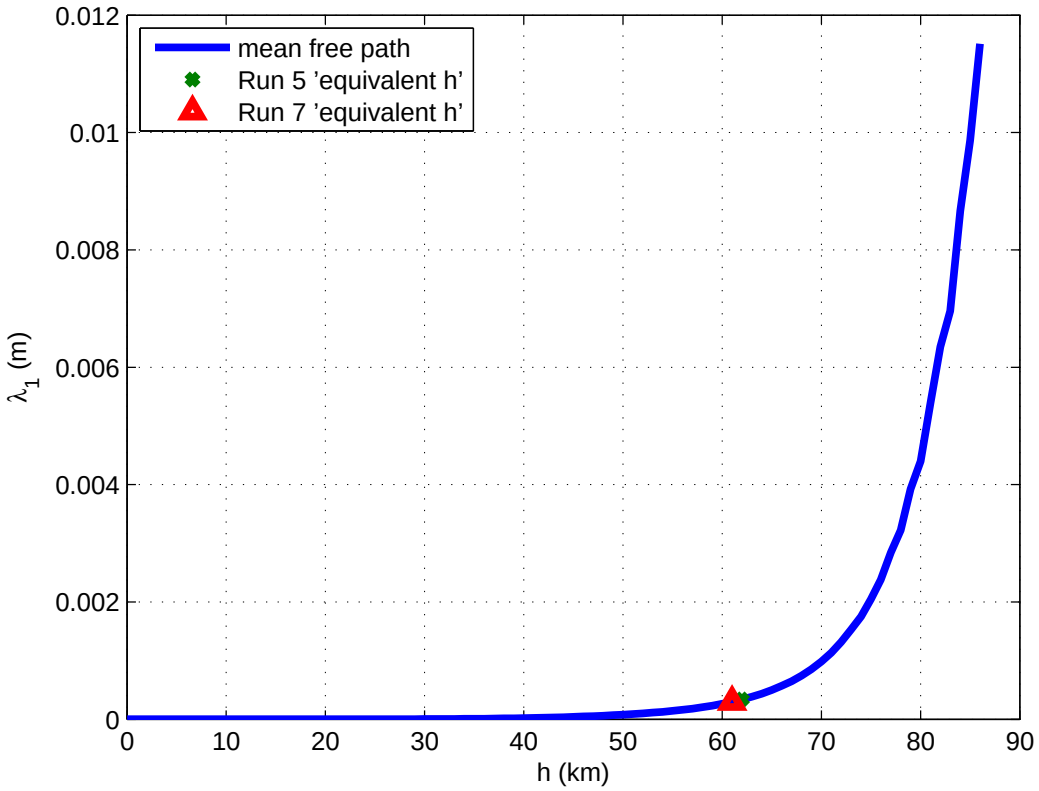

Figure 1: Mean free path from 1976 US Standard Atmosphere [8]

The higher altitude, more rarefied regime has been the domain of the Boltzmann equation. One method very popular today of solving this equation is the Direct Simulation Monte Carlo (DSMC) method due to Bird [9]. The main problem keeping this method from being applied to lower altitude problems is one of computational expense.

Recently, there has been progress in building hybrid methods [10], which solve the Navier-Stokes equations through the flowfield, and by a "continuum breakdown" parameter estimating local Knudsen number,

$$\mathrm{Kn} = \frac{\lambda'}{L} \tag{1.1}$$

a region of nonequilibrium flow is identified, and that region is solved by a DSMC solver, and the two are coupled. This characteristic length,L, is often based on density gradient:

$$\mathrm{Kn}_\rho = \frac{\lambda'}{\rho} \left| \frac{\partial \rho}{\partial x_i} \right| \tag{1.2}$$

Researchers at the Air Force Research Laboratory have shown that entropy generation can be used as a continuum breakdown parameter [11] for assessing the degree of non-equilibrium present in a flow.

Several researchers [12] [13] [14] have taken a different approach, developing generalized hydrodynamic theories which go beyond the Navier-Stokes equations. Most hydrodynamic models are developed from the Boltzmann equation by using some assumptions, simplifications, and series expansions on the Maxwell-Boltzmann distribution of particles in velocity-space. Chapman and Enskog [15] separately developed similar expansions showing that a zero-order expansion generates the Euler equations, while a first-order expansion generates the Navier-Stokes equations.

The natural first step in extending these equations has been to include more terms in the expansion, (e.g. Burnett, Super-Burnett, BGK-Burnett equations). The

problem with these methods is that most of them have been shown to violate the second law of thermodynamics in some areas [16]. The goal of this work is to provide designers with the simplest possible method or model for extending the current continuum computational fluid dynamics (CFD) solvers into the transition regime.

An additional consideration for high Knudsen number flows is the breakdown of the *no-slip* condition. This condition specifies $u = v = 0$ at the wall. As the gas becomes more rarefied, the velocity profile can be discontinuous, and the gas temperature can be different from the adjacent wall temperature.

1.3 Why DSMC?

As mentioned in [17], [18], flows with appropriately defined local Knudsen numbers greater than 0.3 cannot be appropriately modeled with the traditional Navier-Stokes approach. The continuum constitutive relations and their usual assumption of isotropic stresses do not adequately describe the physics of the flow.

Basing Kn on the overall length of the body is not really the right approach, as the mean free path varies throughout hypersonic flowfields. Bird [9] defines L for local Knudsen number as

$$L = \frac{\rho}{d\rho/dx} \tag{1.3}$$

The traditional continuum description of flow is based mostly on the idea that at standard conditions, there are enough molecules present that the flow can be treated in terms of properties averaged over the molecules, as conforming to smooth, well-behaved distribution functions. The "macroscopic" properties at a "point," such as density, pressure, temperature, velocity, et cetera are actually spatially and/or time-averaged properties, over a "differential" volume. According to Bird, when constructing gradients in this description, what is actually required is a finite change in that property over several mean free paths. When this is not the case, the standard continuum model breaks down [9:2].

Bird [9:4], suggests a continuum breakdown parameter (steady flow version):

$$P = \frac{\pi^{1/2}}{2} s \frac{\lambda'}{\rho} \left| \frac{d\rho}{dx} \right| \tag{1.4}$$

where λ' is mean free path, s is a 'speed ratio' of velocity to the most probable speed, $(2RT)^{1/2}$. Bird sets $P = 0.2$ as a value at which initial breakdown occurs.

The problem of predicting breakdown in near-continuum flow is still of interest today, at AFRL [11]. Even DSMC has low Knudsen-number limit: a point at which there are significant fluctuations in the statistics of the algorithm [9:21].

1.4 Molecular Description of Flows

The molecular description of flow has long been studied as the N-body problem. The major difficulty is the fact that N is a large number, and modeling forces of all the bodies on each other is extremely computationally expensive.

Hamiltonian dynamics gives very interesting results for these types of problems, however typically very few molecules are used in any analytical work. Many have attempted analytical solutions to the problem for gases in a flow of interest to aerodynamicists, to no avail.

Simulations have provided some insight, especially in the area of molecular dynamics, see [19], for example. The problem again being, that except for flows with very few molecules or those treated without wall interactions, the vast number of bodies needed for simulation makes problems of interest in hypersonics intractable.

1.5 Boltzmann's Equation

Boltzmann's ideas prompted the derivation of an integro-differential equation, now referred to as Boltzmann's Equation, here for a dilute gas:

$$\frac{\partial}{\partial t}(nf) + \mathbf{c} \cdot \frac{\partial}{\partial \mathbf{r}}(nf) + \mathbf{F} \cdot \frac{\partial}{\partial \mathbf{c}}(nf) = \int_{-\infty}^{\infty} \int_{0}^{4\pi} n^2 (f^* f_1^* - f f_1) c_r \sigma d\Omega d\mathbf{c}_1 \qquad (1.5)$$

where starred quantities are post collision, n is the number density, $\mathbf{c}$ is the velocity class of one collision partner, $\mathbf{c}_1$ is the velocity class of the other (this is a two-body collision), f is the distribution of molecules over velocity space, associated with $\mathbf{c}$, f_1 is the same, associated with $\mathbf{c}_1$, σ is the cross-section, and $d\Omega$ is a differential solid angle. $\mathbf{F}$ is the net effect of external forces, such as an externally applied electric field.

The term on the right hand side of (1.5) is called the collision integral, itself a very difficult quantity to compute. Some researchers [20] have computed this integral over actual velocity space using Monte Carlo integration, and treated the left hand side somewhat similarly to modern CFD approaches, to study normal shock structure.

The Boltzmann equation relates collisions sampled from continuous velocity distribution functions to time and spatial rates of change of those continuous velocity distribution functions. One could imagine then, that there may be a low-density limit on the usefulness of the Boltzmann equation, collisionless Boltzmann equation, or DSMC, in terms of a situation where there are not enough molecules present in the volume of interest to compute a continuous velocity distribution which had any meaning. There is also an idea of *ergodicity* inherent in this equation. That is to say, spatial and time derivatives of averaged quantities are equated.

1.6 Processes of DSMC

The basic idea in DSMC is not to solve the Boltzmann Equation directly by an analytic process, but rather to use a stochastic model to simulate the Boltzmann Equation, with statistics and collision processes which try to match kinetic theory.

The first operation in DSMC is the discretization of the geometry of the flowfield into cells and assignment of boundary conditions just as in CFD. The next step is gathering information about the flow constituents, such as molecular weight, rotation

and vibration characteristic temperatures, moments of inertia, dissociation energies, and other parameters pertaining to the flow of interest. The third step is initializing the flow, usually to some equilibrium distribution about the mean freestream velocity, using a pseudorandom number generator. Pseudorandom number generators will be discussed further in the next section.

Rather than integrating trajectories deterministically, the main algorithm applies a stochastic model to determine how many collisions occur within each cell, how much energy is transferred to the various modes (translational, rotational, vibrational), and which molecules will move to adjacent cells. Of course, this model should be subject to constraints of conservation of particles, momenta, and energy. Critics of DSMC point out that it is very difficult to prove within the simulation that these quantities are actually conserved.

Molecules (or atoms) in wall-bounded cells are treated according to an accomodation coefficient, with one extreme being diffuse reflection (somewhat akin to a no-slip condition) and the other extreme being specular reflection. Most simulations discussed in [9] are accomplished with pure diffuse reflection. Diffuse reflection refers to the situation of the outgoing velocity of the collision being assigned a Maxwellian (or Rayleigh in the normal direction) distribution referenced to the wall, whereas specular reflection refers to the molecule being reflected in the normal direction with the same speed, and retaining its tangential speed. This model, though it may be beyond the no-slip treatment afforded by many CFD solvers, is quite a simplification of what may actually be happening at the wall, in terms of force potential and energy transfer. However, Bird [9] gives several examples where this is reasonable.

During this process, the program systematically takes samples of particle velocity and other parameters at user-defined intervals. The idea is, once the transients due to the initial conditions have died, the velocities (and time-averaged quantities based on them) reach some steady-state distribution.

From the law of large numbers, if some quantity obeys a particular distribution over the entire population, the cumulative distribution of samples approaches that of the population as the inverse root of the number of samples:

$$lim_{M\to large}| < x > -E[< x >]| \approx \frac{1}{M_s} \tag{1.6}$$

where M is the number of observations, $< x >$ is the average over the samples, and $E[< x >]$ is the expected value over many samples.

One can imagine this process getting computationally expensive. One thing DSMC does to reduce this problem, is to simulate "pseudoparticles," which represent many actual particles (molecules, atoms, etc.). There are assumptions which go along with this idea, the most common being that all the particles within each pseudoparticle are in equilibrium with each other. Bird gives data to support the idea that this works, in many cases.

1.7 Numerics

DSMC is highly dependent on a "good" pseudorandom number generator. Generators which repeat too often, and/or have "clumping" of the distributions of pseudorandom numbers can effect the results, or greatly increase the time required to obtain a solution with stationarity of the averages over the samples. Some workers refer to this behavior as convergence, but it bears no mathematical resemblance to convergence of an algorithm for solving a deterministic equation. Optimally, the grid should be such that the cell size is about one third of the mean free path.

In contrast to DSMC, in CFD, the solution is based on an iterative process. Cell size is related to the magnitude of gradients to be captured. Another big issue with CFD is measuring the numerical dissipation renders the converged solution different from the actual flow being modeled, where this dissipation is required by many CFD schemes for numerical stability. One can also speak of grid convergence, meaning the grid resolution at which the solution does not improve with grid refinement. In

the hypersonic situation, cell sizes have to make sense in terms of an appropriate breakdown parameter, as mentioned above. If the cells are smaller than a few mean free paths, the solution can become less physically meaningful [9:4].

It is the argument of Bird, developer of DSMC, that it is not physically meaningful to compute gradients in the continuum description in this case [9:4]. There are other arguments, e.g., Lumpkin [21:4], Carr [11:22-23] which submit that the constitutive model could be redefined for the continuum transition regime, and continuum solutions could be obtained from these. There is a field of study devoted to this, called generalized hydrodynamics [14], [12].

1.8 Computational Cost

Computational cost is time spent per solution, either in total CPU time , or "wall time." Of the three major computational methods mentioned, CFD is generally fastest. The molecular dynamics method is generally considered the slowest. One reason for this is the total number of computations performed per time step, which can be related to the number or grid points, and in the particle simulations, to the number of particles. The other consideration is the choice of a time step. Since molecular dynamics is a deterministic, mechanics-based solver, the time step must be small enough to allow integration of molecular trajectories. In DSMC, the time step is not as restrictive, but still must be less than the mean time between collisions. The movement is broken into two main steps, one for movement of particles, and a second for collision events, based on the distribution of particles at the end of the movement step. In explicit-integration CFD, the time step is based on the speed a wave can travel in the fluid and cell size. Information propagates through the grid through local calculation of the convective derivative. In implicit-integration CFD, the timestep can be theoretically be many times that of the explicit. Implicit integration solves the time derivative globally, allowing information to propagate much farther across the grid. The global time derivative can be thought of as an operator or matrix to be inverted to solve for the values in the grid at the next time step. The DSMC method

is more computationally intensive than CFD, however, it can potentially provide a more accurate answer in regions where the hydrodynamic equations being solved are not valid. Here it is assumed the DSMC software is given the input paramters and boundary conditions to most closely match the physical observations. As computers become more powerful, the higher computational expense of DSMC over CFD may make less difference to designers. Bird writes in his 1994 book [9] that all his simulations took less than 24 hours. Realistic flows of interest in hypersonic engineering are still more than one day per solution today.

Alternative solutions from the CFD world are beginning to show some success, however [22], [16]. There may be more overlap in the "transition region," meaning transition from "1st-order Navier-Stokes" methods to DSMC. These alternative solutions attempt to extend CFD to a higher order approximate solution of the Boltzmann equation, or a simplified version thereof, by either extending the computation of the dissipation terms, or rewriting them in terms of relaxation terms, and treating each mode of energy separately.

1.9 Bulk Viscosity and Nonequilibrium

It is useful to describe what we mean by nonequilibrium from the macroscopic sense. Here we are meaning there are no external forces on the gas, and thereby no gradients. In the absence of gradients and external forces, the gas is in an overall inertial rest state. No spatial changes occur (convective), nor are there any changes with advancing time. In a dilute, monatomic gas this is fairly simple. In a polyatomic gas, internal energy modes exist, which are excited and de-excite between quantized levels through collisional processes. That is to say, collisions with energy comparable to the difference between quantized energy states have a potential to trade some translational energy for the internal. These collisions are called "inelastic."

For a monatomic gas, the Boltzmann equation (1.5) can be used as a starting point for the microscopic. At rest, there should be no rate of change in the velocity distribution function. This state can in general be attained in a gas, when the right

hand side integrand is zero:

$$f^* f_1^* - f f_1 = 0 \tag{1.7}$$

This relationship is one of collisional invariance, and is, in fact, closely related to the formulation of the equilibrium distribution function, the principle of detailed balance, and the Boltzmann H-theorem (a microscopic version of the second law of thermodynamics). The principle of detailed balance states that for every collision, there is a corresponding inverse collision, restoring the system to the equilibrium distribution. The product of the starred quantities is known as the "gain term", and the unstarred the "loss term". It is interesting to note that quantum mechanics had not been developed by the time this principle was first derived. The principle is somewhat at odds with the Heisenberg uncertainty principle, which states that there is a finite lower bound on the precision one can observe both the momentum and position of a particle.

For a polyatomic gas, in general there is no *principle of detailed balance*. The presence of the internal modes complicates matters significantly. Generalized Boltzmann equations have been formulated to try to describe the momenta and positions of these particles, in both classical [23], and quantum mechanical versions [2:145].

The continuum description of the fluid can be obtained from the Boltzmann (in the case of a dilute monatomic gas) [15], or generalized Boltzmann equations (in the case of a polyatomic or electronically excited monatomic gas) [2:221-266]. The form of the equations, but also more importantly the transport coefficients can be calculated using the information contained in the intermolecular potential. For a monatomic gas, this is spherically symmetric. For the polyatomic, it is not. For translation-rotation energy exchanges, this anisotropy is very important. See, for example [2], [24] for greater detail.

This work follows that of Carr [11], and in his work, he suggests new temperature-dependent models for transport coefficients, and the inclusion of bulk viscosity in the Navier-Stokes Equations to extend their validity in altitude in the continuum and

near-continuum regimes. It is the goal of this work to treat rotational nonequilibrium in the Navier-Stokes equations as a way of improving the high-altitude accuracy of CFD solutions. This work does *not* attempt to solve all the problems of both translational and rotational nonequilibrium, but rather to gauge the effect of including bulk viscosity in the continuum CFD.

1.10 What is bulk viscosity?

Bulk viscosity is a resistance to a volumetric change in a gas, such as an expansion or contraction. Expansions and contractions are mathematically represented as the divergence of the velocity field. Bulk viscosity linearly relates the divergence to a difference in two pressures: thermodynamic equilibrium pressure and mechanical pressure, or one third of the trace of the stress tensor. In this way, any nonequilibrium phenomena that makes these two values different (rotation, vibration, other internal mode excitation) could be treated with bulk viscosity, assuming "small deviations" from equilibrium. The present work will consider only the rotational contribution to the bulk viscosity. Traditional Navier-Stokes equations, and the CFD built on them, assume that the rotational modes of energy are always in equilibrium with the translational (and completely neglects other internal energy modes). Several early works state that the equilibration is always within about 4-5 collisions, and therefore this assumption should not cause a problem, with the exception of the calculation of shock structure. The experimental data of Alsmeyer [25] tends to agree with this. Other experiments, e.g. Carnevale et al [26], Prangsma, et al [27],Belikov et al [28] and some models [29], [30] disagree with this, however. Alsmeyer's data was gathered from density profiles in Nitrogen, at room temperature, but very low pressure (and therefore density). Carnevale et al used ultrasonic measurements to calculate rotational relaxation time, and Belikov et al used a jet expanding into near-vacuum conditions.

Bulk viscosity can be found in the Navier-Stokes stress term, to be described in detail in Chapter II. Vincenti and Kruger [31:407-412] and McCourt et al [2]

(as volume viscosity, η_v, as is common in the Molecular Physics community) give arguments for its use. It should be noted that the bulk viscosity treatment has been the subject of controversy for quite some time [32]. A historical treatment of bulk viscosity (at least through 1999, from the aeronautical engineering perspective) can be found in Argrow and Graves [33]. Arguments for and against the validity of bulk viscosity as a physical relaxation parameter can be found in Meador [34], and Emanuel [35]. Some of the controversy is over the apparent frequency-dependence of sound attenuation. Volume viscosity, as it is seen in the molecular physics literature [2: 280], equation (6.2-24), is related to bulk viscosity, as

$$\frac{\alpha p}{\omega^2} = \frac{1}{2\gamma c_{ad}} \left[\frac{4}{3}\eta + \frac{\gamma + 1}{\gamma} \frac{m\lambda}{k} + \eta_v \right] \tag{1.8}$$

where ω is the sound frequency, η is shear viscosity, α is the absorption coefficient, c_{ad} is the adiabatic sound speed in the limit of zero frequency, λ is the thermal conductivity, k is Boltzmann's constant, and η_v is bulk viscosity. Using sound absorption experiments makes the value of bulk viscosity calculated from these kinds of experiments very sensitive to small errors in the measurement of α. Also, in [2:284], it is explained that ultrasonic sound absorption experiments only measure the rotational relaxation part of bulk viscosity. The reason for this is thought to be the much longer relaxation time of vibrational modes, and the high frequency of the sound. The requirement on ultrasonic measurements of absorption coefficient is $\pm 1\%$, to be considered useful for measuring bulk viscosity. Expansion measurements have been subject to this scrutiny as well.

1.11 Scope of the Thesis

In this work, Chapter II will outline the history, theory, and experimental results for rotational relaxation, the basic treatments for rotational relaxation within the hydrodynamics and DSMC frameworks. The recent rotational relaxation calculations

of Cappelletti, Vecchiocattivi, Pirani, Heck, and Dickinson [36:491] are discussed, and used as the basis for bulk viscosity in an axisymmetric CFD code, AFIT-2D.

Chapter III outlines the numerical methods within AFIT-2D, and the methods behind a one-dimensional Navier-Stokes solver for shock structure, based on the method of Gilbarg and Paolucci [37], used to show the effect of bulk viscosity on shock structure. It should be pointed out that translational nonequilibrium, beyond what limited amount is afforded by the Navier-Stokes equations, is beyond the present scope. Use and modification for the present work of an algebraic grid adaption routine, borrowed from Gnoffo, Hartung, and Greendyke [38:2-3] is presented. Description of the two-dimensional axisymmetric test cases from a 2003 code validation experiment [1] is described.

Chapter IV presents the results of the continuum calculations, comparing the zero bulk viscosity, constant bulk viscosity, and the bulk viscosity calculated from the data of Cappelletti et al. are compared in both 1D and 2D cases. Where applicable, DSMC data from Carr [11] is used for comparison.

Chapter V presents conclusions on the effect of including the bulk viscosity, and its usefulness in turning calorically perfect gas-based CFD into a preliminary design tool for high-altitude CFD. Recommendations for future work are presented.

II. Rotational Relaxation

IN classical kinetic theory, rotational energy is expressed in terms of 'degrees of freedom.' Here the number of axes about which the molecule can rotate, and posess a significant amount of energy is multiplied by $Tk_B/2$, which amounts to a maximum entropy state. This statement of course, is made assuming that the numbers of states available is continuous and proportional to temperature.

The typical continuum stress tensor for a Newtonian fluid is given by

$$\tau_{ij} = -p\delta_{ij} + \mu\left(\frac{\partial u_i}{\partial x_j} + \frac{\partial u_j}{\partial x_i}\right) + \delta_{ij}\lambda\left(\frac{\partial u_k}{\partial x_k}\right) \tag{2.1}$$

where λ is commonly labeled the second coefficient of viscosity, which is related to the bulk viscosity, μ_B by the definition

$$\lambda \equiv \mu_B - \frac{2}{3}\mu \tag{2.2}$$

Typically, a "mechanical pressure" is defined as the average of the dilatational stresses [2: 123], [31:410]:

$$\bar{p} = -\frac{1}{3}\tau_{kk} = p - \mu_B\frac{\partial u_k}{\partial x_k} \tag{2.3}$$

The "thermodynamic pressure" is defined by the equilibrium pressure for the given temperature:

$$p = \rho RT = nk_BT \tag{2.4}$$

where n is the number density, k_B is Boltzmann's constant. The two representations are related by $\rho = mn$ and $R = k_B/m$, where m is the molecular weight. From kinetic theory (see Vincenti and Kruger [31:410] or McCourt et al [2:122-123]):

$$p - \bar{p} = p - \frac{1}{3}\rho\bar{C^2} = \mu_B\frac{\partial u_j}{\partial x_j} \tag{2.5}$$

therefore if $p = \bar{p}, \rightarrow \mu_B = 0$ Thermal velocity, C_i, is defined as the molecular speed c_i minus the mean flow velocity u_i.

It should be mentioned that taking internal energy modes into account in the energy equation was first treated by Eucken [2:62,124]. This expression for Eucken factor relates the shear viscosity, isochoric (or constant volume) heat capacity, and thermal conductivity:

$$f_E = \frac{k}{\mu C_v} = \frac{km}{\mu c_v} \tag{2.6}$$

This result should look familiar to aerodynamicists as $(c_p/c_v)/Pr$. For monatomic gases, this value is 5/2. For polyatomic gases, approximate empirical relationships are often used [2:124]:

$$f_E = f_E^t \frac{c_v^t}{c_v} + f_E^i \frac{c_v^i}{c_v} \tag{2.7}$$

where i denotes internal energy, and t denotes translational energy, and [39:30]:

$$Pr = \frac{4\gamma}{7.08\gamma - 1.80} \tag{2.8}$$

Stokes' Hypothesis sets the bulk viscosity to zero, which effectively sets the two pressures always equal. This hypothesis therefore implies equilibrium conditions throughout the flow. It is experimentally and analytically verified for dilute monatomic gases. By dilute here we also are bringing in the idea of a low-density limit of the bulk viscosity. Even for a monatomic gas, the bulk viscosity is nonzero when the density is not sufficiently low. See Rah and Eu [40] for more detail. In fact, the other transport properties used in the Navier-Stokes description in terms of temperature alone are the low-density limit transport properties, and, in general, are density dependent [39:25-31].

The higher density gases also cease to be treatable by the ideal gas law

$$p = \rho RT = nk_BT \tag{2.9}$$

but are, rather by the van der Waals equation of state [41:22]

$$\left(p + \frac{a}{v^2}\right)(v - b) = RT \tag{2.10}$$

which is also known as the real gas equation of state. Bulk viscosity has its greatest effect in non-equilibrium situations, especially places like shocks where the translational modes of energy are the first to be excited, and there is a collisional process of exciting internal energy modes. In a monatomic gas, kinetic theory predicts zero bulk viscosity, as until quite high temperatures, there are no internal modes to be excited, and the only kind of nonequilibrium present in this situation is translational.

In a diatomic gas, such as N_2 or air, the rotational mode can lag the translational, but only by a few collisions. So, in a dense (say sea-level standard conditions) environment, the region of non-equilibrium in a supersonic flowfield is very small and can often be neglected. However, at high altitudes, in lower density, this effect can be more pronounced.

The idea of using bulk viscosity as a way of compensating for small degrees of nonequilibrium is not new [15], [31]. A paper by Graves and Argrow [33] outlines a history of the bulk viscosity, including its use to predict nonequilibrium behavior. The bulk viscosity has been reported to be frequency dependent by some in the field of acoustics. However, a search of the literature reveals little quantitative information about what a "small degree" of nonequilibrium really is. Heck et al. remark that there is a lack of data on the bulk viscosity, and that obtaining it is difficult.

Values of bulk viscosity due to Heck et al. [24] [42] will be used in this study. These are based on collision cross-sections calculated from a relatively new model of the intermolecular potentials for nitrogen. These potentials, unlike the hard sphere, Maxwell molecule, Sutherland, and Lennard-Jones, are *anisotropic*, since Nitrogen molecules are not spherically symmetrical. This anisotropy of the potential determines how rotational energy is transferred between colliding molecules.

2.1 The Boltzmann Equation for Dilute Monatomic Gases

The Boltzmann equation can be derived from the 6N-degree of freedom Liouville equation for the probability distribution function of a molecule's position and velocity

in an N-molecule system. This treatment is beyond the scope of this thesis, and can be found in Sone [43:257-269]. The Liouville equation itself is a result from the field of statistical mechanics.

It is somewhat a misnomer to call a physical gas dilute. A dilute gas is a mathematical construction, coming from an assumption that no more than two molecules interact (collide) at the same time [2:2]. This construction is also known as the *binary collision model*. The effect of other molecules during "free flight" and "collisions" are ignored. No matter the form of the intermolecular potential, that potential is treated as vanishing beyond some finite distance. In the physical, it is practically impossible to verify that this is ever the case. A dilute gas then could be defined as one for which predicted macroscopic behavior using the dilute assumption "agrees well" with measured macroscopic behavior. That is to say, one for which the amount of non-binary collisions has a negligible effect on the overall compared values.

In a gas at rest and in thermal equilibrium with its boundaries, the velocities of the molecules tend to be distributed according to a Maxwellian Distribution distribution [31:35]:

$$f(C_i) = f(C_1, C_2, C_3) = \left(\frac{m}{2\pi kT}\right)^{3/2} \exp\left[-\frac{m}{2kT}(C_1^2 + C_2^2 + C_3^2)\right] \tag{2.11}$$

Recall the Boltzmann Equation from chapter I [9:53]:

$$\frac{\partial}{\partial t}(nf) + \mathbf{c} \cdot \frac{\partial}{\partial \mathbf{r}}(nf) + \mathbf{F} \cdot \frac{\partial}{\partial \mathbf{c}}(nf) = \int_{-\infty}^{\infty} \int_{0}^{4\pi} n^2 (f^* f_1^* - f f_1) c_r \sigma d\Omega d\mathbf{c}_1, \tag{2.12}$$

where f is the pre-collision velocity distribution function of the molecule selected for collision, f_1 is the pre-collision velocity distribution function of the collision partner, and the starred versions are the post-collision representations of the same. $\mathbf{c}$ is the molecular velocity of the molecule associated with f. $\mathbf{F}$ is an external force (such as applied electric field).

Chapman and Enskog separately developed an expansion about the normal distribution, here as $f^{(0)}$ equation 2.11 [15:107]:

$$f = f^{(0)} + f^{(1)} + f^{(2)} + \dots \tag{2.13}$$

Enskog introduced a parameter θ, which can be related to Knudsen number [15:115]:

$$f = \frac{1}{\theta} f^{(0)} + f^{(1)} + \theta f^{(2)} + \theta^2 f^{(3)} + \dots \tag{2.14}$$

This process ends in an expansion of unknown functions ϕ^n and Knudsen number:

$$f = f^{(0)}(1 + Kn\phi_1 + Kn^2\phi_2 + \dots) \tag{2.15}$$

Lumpkin [21:15] points out this expansion, used in the Boltzmann equation can be shown to give the Euler equations when truncating at 0 order, the Navier-Stokes equations when carried to first order, and the Burnett equations when carried to second order, but in general, is asymptotic or divergent. Results can be obtained for small Kn, but the expansion exhibits nonconvergent behavior for $Kn \gg 1$. This behavior is often cited as the reason why the continuum assumption fails for large Kn.

2.2 Classical Rotational Relaxation Results

The rotational collision number Z_r is a measure of the ratio of rotational relaxation time τ, the time-constant for rotation to equilibrate with translation in a heat bath, to mean time between collisions τ_c:

$$Z_r = \frac{\tau}{\tau_c} \tag{2.16}$$

The rotational relaxation time is essentially a time constant in a simple, first-order ordinary differential equation, originally proposed by Jeans [44], as cited by

Lumpkin [21:52]:

$$\frac{de_r}{dt} = \frac{E^{eq}(T_t) - E_r}{\tau} \tag{2.17}$$

This equation has the same form as the Landau-Teller equation for vibrational relaxation. It assumes translational equilibrium, meaning the velocity distribution of molecules during this process is Maxwellian.

Parker [29:454] in his classic, well known article, solved a system of classical equations of motion analytically to obtain an expression for the rotational collision number, Z_r:

$$Z_r = \frac{Z_\infty}{1 + \pi^{\frac{3}{2}}(S/T)^{\frac{1}{2}} + \left(\frac{\pi^2}{4} + 2\right)(S/T)} \tag{2.18}$$

where Z_∞ is the maximum, or perhaps more appropriately, asymptotic rotational collision number, and S is known as *Sutherland's Constant* by White [39:28]. It is a measure of the "well depth" [29:458] of the intermolecular potential. Note that the coefficient of the (S/T) term has the correction of Brau and Jonkman [30:481] applied. One assumption of this work was that of a gas with initially nonrotating molecules. Another was one of "impulsive" or "sudden" collisions, where the duration of an intermolecular collision was treated as much shorter than the rotational period of the molecule.

This form of rotational collision number is still in use in DSMC today [45:2]. Brau and Jonkman re-solved this problem stochastically, first by removing Parker's first assumption, and obtained exactly one-half his result [30:481]. Then, they came to a solution assuming "adiabatic" collisions, that is to say, collisions for which the rotational period is much shorter than the collision time, and found that for this case, the idea of a single relaxation time is no longer valid.

2.3 Phenomenological and Semiclassical Results

Some insight into the definition of phenomenological model can be obtained from Bird [46:2,6]. The premise is a model which qualitatively agrees with phenomena observed in nature. The opposite end of the spectrum is the idea of *ab initio* or "from

first principles." In the case of molecular physics, the principles of quantum mechanics are treated as the first principles. In classical treatments, Newton's Laws are the first principles.

If the quantum mechanics are the more appropriate starting point in fluid flow, then the Navier-Stokes (here the meaning is the momentum conservation equations for which Navier and Stokes are strictly responsible) constitutive models are a very successful example of phenomenological modeling. Quantum mechanics were not available at the time, and microscopic, kinetic theory models were not used in their derivation.

The DSMC codes produced by Bird [9] use the Larsen-Borgnakke phenomenological model for internal energy relaxation. This model uses a constant rotational collision number, which for Nitrogen has a default value $Z_r = 5$ [47]. The DSMC code available to Carr [11] was MONACO, from Boyd's group, which uses Parker's model [45:2] for rotational relaxation. This model uses a rotational collision number of the form in equation (2.18). The default values of S and Z_∞ are those of the original Parker model. Carr [11:41] uses $Z_\infty = 15.7$, $S = 80$K in his solutions. The rotational collision number is related to the variable hard sphere model, as outlined in Lumpkin, Haas, and Boyd [48]. Wysong and Wadsworth give an assessment of phenomenological rotational relaxation models for DSMC [49].

2.4 Generalized Boltzmann Equation Rotational Relaxation Results

Cappelletti et al [36] compute a potential energy surface PES, modifying existing work by Heck and Dickinson [24], [42], and then compute transport coefficients using Heck and Dickinson's semiclassical solver based on a second-order Chapman-Enskog expansion of the generalized Boltzmann equation of Curtiss, Kagan, and Maksimov as described in [2:145-158]. One interesting feature of this work is a comparison between the new PES and an earlier surface, the AWJ potential. The AWJ potential was obtained from an *ab initio* short-range interaction. The new PES, deemed PES8 was a modification of the earlier AWJ potential, adjusted to better match observed

relaxation cross-sections. Both PES are of the form

$$V(\mathbf{R}, \hat{\mathbf{r}}_1, \hat{\mathbf{r}}_2) = (4\pi)^{3/2} \sum_{L_A, L_B, L} V_{L_A L_B L}(R) A_{L_A L_B L}(\hat{\mathbf{R}}, \hat{\mathbf{r}}_1, \hat{\mathbf{r}}_2) \tag{2.19}$$

where A is a set of orthormal functions, $\mathbf{R}$ is the vector from the center of molecule A to that of molecule B, and $\hat{\mathbf{r}}_1$ and $\hat{\mathbf{r}}_2$ [36:486].

The article of Cappelletti et al [36] does not explicitly discuss the form of the hydrodynamics equations which come from this particular application of the Chapman-Enskog expansion. The present work will use the results for μ_B in the Navier Stokes equations. The incorporation of bulk viscosity in the Navier-Stokes equations in this way could be considered "phenomenological modeling" by the definition of Bird [9].

It should be noted that the aerodynamics community is just starting to take interest in generalized Boltzmann equations, for example, see Cheremissin and Agarwal [50]. These workers report, as does [2], the Wang-Chang-Uhlenbeck-de Boer [51] equation, seen in the aerodynamics literature in the 1950s and 1960s, does not handle properly the degeneracy of rotational states. Cheremisin and Agarwal present one dimensional shock solutions, taking on the order of weeks to compute using the generalized Boltzmann equation they have been using.

2.5 Bulk viscosity from Z_r

The bulk viscosity is related to the the rotational relaxation time, τ, as

$$\mu_B = \frac{c_{rot} k_B}{c_v^2} p\tau \tag{2.20}$$

where c_v is the isochoric or constant-volume heat capacity, and c_{rot} is the isochoric rotational heat capacity [36]. The shear viscosity coefficient is defined by Parker [29] to be related to the mean time between collisions, τ_c, by

$$\tau_c = \frac{\pi \mu}{4p} \tag{2.21}$$

The rotational collision number, Z_r, is defined by equation 2.16. Solving equations (2.16), (2.20) and (2.21) for μ_B/μ, we obtain

$$\mu_B/\mu = \frac{\pi}{4}\left(\frac{c_{rot}k_B}{c_v^2}\right)Z_r \tag{2.22}$$

In the present work, $c_{rot} = k_B$ is assumed. It should be mentioned, however, that correlations for c_{rot} are available [36:491]. This assumption allows a simpler expression for the ratio of bulk to shear viscosity:

$$\mu_B/\mu = \frac{\pi}{4}(\gamma - 1)^2 Z_r \tag{2.23}$$

Z_r is fit to the reported values from [36:492] with a polynomial in temperature:

$$Z_r(T) = f_3T^3 + f_2T^2 + f_1T + f_0 \tag{2.24}$$

where $f_3 \approx 1.034\text{E}-9$, $f_2 \approx -3.835\text{E}-6$, $f_1 \approx 1.104\text{E}-2$ and $f_0 \approx 1.905$. This fit, along with the reported data, is depicted in Figure 2, along with the models due to Parker [29] and [30] for comparison. These models are commonly used in DSMC. Here, the Parker model has its original values of Z_∞ and S. Note, the newer work reports a higher rotational collision number, and therefore higher bulk viscosity. Also, though the data from Cappelletti et al is not reported above about 1400K, it does not suggest an asymptotic value at higher temperatures. The collision model used for determining Z_r uses the infinite-order sudden approximation. This approximation is not valid at high collision energies, and therefore is limited to this low temperature range. For more detail on the difference between sudden, adiabatic, and close-coupled approximations, the reader is referred to [2, 49, 52].

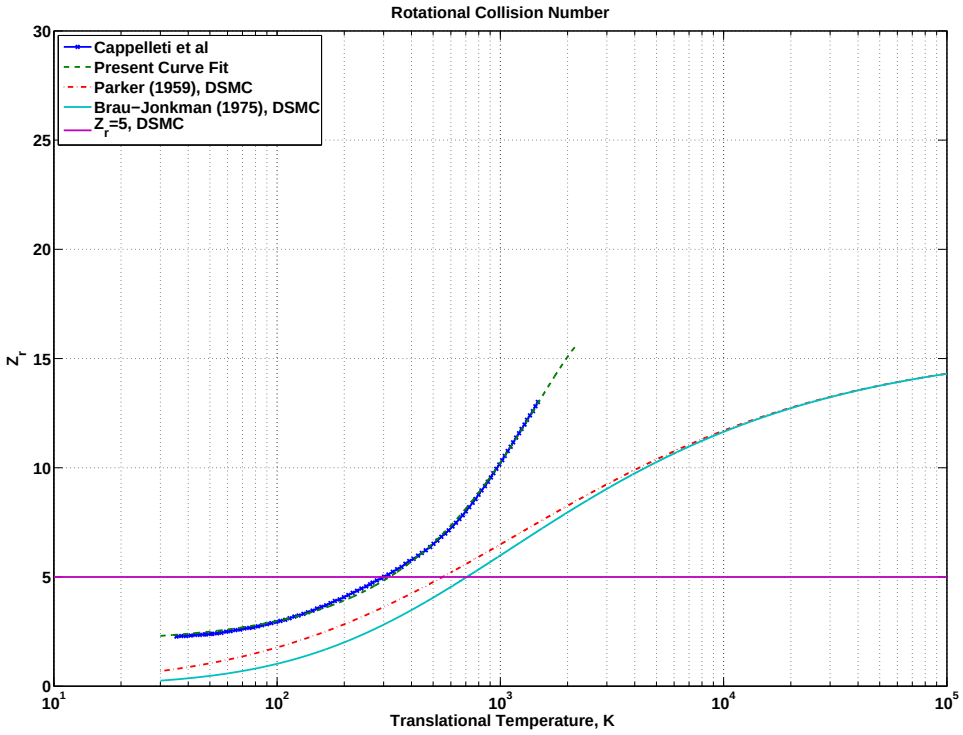

Figure 2: Rotational collision number

III. Numerical Methods

THE basic framework for testing the bulk viscosity in the continuum model is AFIT-2D, developed at the Air Force Institute of Technology. This code being small, flexible, and with all source code available, was the natural choice for this work.

3.1 History of AFIT-2D

AFIT-2D is a finite volume Navier-Stokes code for simulation of two dimensional compressible flows. The present work uses an augmented version for axisymmetric flow that retains the bulk viscosity in the viscous terms. The code has several user-selectable time integration schemes and flux schemes. The flow variables and transport coefficients are nondimensionalized by Mach number, Reynolds number and Prandtl number. Recall from Chapter II that the use of a constant Prandtl number is equivalent to Eucken's approximation for heat transfer. While the solver is written in Reynolds Averaged Navier Stokes form, which can compute eddy-viscosity-based turbulent flows, all solutions presented in this work were computed as laminar. The Reynolds numbers of the flows considered were all well within the laminar flow regime, as confirmed by experiment [1].

3.2 Methodology of AFIT-2D

Axisymmetric flow is included as a special case by means of a source term in the Navier-Stokes equations. The formulation in conserved variable vector form adapted from Hoffman and Chiang [53:Vol II, 456–457] is

$$\frac{\partial Q}{\partial t} + \frac{\partial E}{\partial x} + \frac{\partial F}{\partial y} + \alpha H = \frac{\partial E_v}{\partial x} + \frac{\partial F_v}{\partial y} + \alpha H_v \tag{3.1}$$

where

$$Q = \begin{bmatrix} \rho \\ \rho u \\ \rho v \\ E_t \end{bmatrix}, \quad E = \begin{bmatrix} \rho u \\ \rho u^2 + p \\ \rho uv \\ (E_t + p)u \end{bmatrix}, \quad F = \begin{bmatrix} \rho v \\ \rho uv \\ \rho v^2 + p \\ (E_t + p)v \end{bmatrix}, \quad H = \frac{1}{y} \begin{bmatrix} \rho v \\ \rho uv \\ \rho v^2 \\ (E_t + p)v \end{bmatrix}, \tag{3.2}$$

$$E_v = \begin{bmatrix} 0 \\ \tau_{xx} \\ \tau_{xy} \\ u\tau_{xx} + v\tau_{xy} - q_x \end{bmatrix}, \quad F_v = \begin{bmatrix} 0 \\ \tau_{xy} \\ \tau_{yy} \\ u\tau_{xy} + v\tau_{yy} - q_y \end{bmatrix} \tag{3.3}$$

where $\alpha = 0$ for the case of a 2D cartesian problem, $\alpha = 1$ for an axisymmetric problem,

$$H_v = \frac{1}{y} \begin{bmatrix} 0 \\ \tau_{xy} + \frac{y}{Re_\infty} \frac{\partial}{\partial x} \left(\frac{\lambda v}{y} \right) \\ \tau_{yy} - \tau_{\theta\theta} + \frac{\lambda}{Re_\infty} \left(\frac{v}{y} \right) + \frac{y}{Re_\infty} \frac{\partial}{\partial y} \left(\frac{\lambda v}{y} \right) \\ u\tau_{xy} + v\tau_{yy} - q_y + \frac{\lambda}{Re_\infty} \frac{v^2}{y} + \frac{y}{Re_\infty} \frac{\partial}{\partial y} \left(\frac{\lambda v^2}{y} \right) + \frac{y}{Re_\infty} \frac{\partial}{\partial x} \left(\frac{\lambda uv}{y} \right) \end{bmatrix} \tag{3.4}$$

and

$$\tau_{xx} = \frac{1}{Re_\infty} \left[(2\mu + \lambda) \frac{\partial u}{\partial x} + \lambda \frac{\partial v}{\partial y} \right] \tag{3.5}$$

$$\tau_{yy} = \frac{1}{Re_\infty} \left[(2\mu + \lambda) \frac{\partial v}{\partial y} + \lambda \frac{\partial u}{\partial x} \right] \tag{3.6}$$

$$\tau_{xy} = \frac{\mu}{Re_\infty} \left(\frac{\partial u}{\partial y} + \frac{\partial v}{\partial x} \right) \tag{3.7}$$

$$\tau_{\theta\theta} = \frac{1}{Re_\infty} \left[(2\mu + \lambda) \frac{v}{y} + \lambda \left(\frac{\partial u}{\partial y} + \frac{\partial v}{\partial x} \right) \right] \tag{3.8}$$

$$q_x = -k \frac{\partial T}{\partial x} \tag{3.9}$$

$$q_y = -k \frac{\partial T}{\partial y} \tag{3.10}$$

where λ is defined by equation (2.2).

In typical, calorically perfect gas-based CFD,

$$k = \frac{\mu}{Re_\infty Pr(\gamma - 1)M_\infty^2}, \quad \text{and} \quad E_t = \frac{\rho}{2}(u^2 + v^2) + \frac{p}{\gamma - 1} \tag{3.11}$$

Sutherland's model for shear viscosity is often used in CFD:

$$\frac{\mu}{\mu_{ref}} = \left(\frac{T}{T_{ref}}\right)^{3/2} \frac{T_{ref} + S}{T + S} \tag{3.12}$$

The grid transformation presented by Gnoffo, Hartung and Greendyke [38] will be used to cluster cells in the vicinity of the shock and the wall, where gradients are highest. Bulk viscosity will be first calculated from curve-fit equation 2.24.

3.3 Calculation of Convective Flux

For convective flux calculation in AFIT-2D, the flux difference splitting method of Toro, Spruce and Speares [54] (HLLC) is used, selecting wavespeeds as described in the paper by Batten et al [55]. This scheme restores the contact discontinuity to the HLL scheme of Harten, Lax, and van Leer [56]. The HLLC flux-difference splitting method is defined in [55] as

$$F_{hllc} = \begin{cases} F_L & : \quad S_L \geq 0 \\ F_L^* & : \quad S_L < 0 < S^* \\ F_R^* & : \quad S^* \leq 0 < S_R \\ F_R & : \quad S_R \leq 0 \end{cases} \tag{3.13}$$

The recommended wave speeds from [55] are used:

$$S_L = \min\left[\lambda_1(U_l), \lambda_1(U^{Roe})\right] \tag{3.14}$$

and

$$S_R = \max\left[\lambda_m(U^{Roe}), \lambda_m(U_r)\right] \tag{3.15}$$

Also,

$$U^{Roe} \equiv \hat{Q} \tag{3.16}$$

$$\lambda_1 = \tilde{U}_l - a_l \rightarrow \lambda_1(\hat{Q}) = \tilde{U}_{Roe} - a_{Roe} \tag{3.17}$$

and

$$\lambda_m = \tilde{U} + a \tag{3.18}$$

Starred values are defined as

$$F_i^* = F_i + S_i(Q_i^* - Q_i), \quad i = L, R \tag{3.19}$$

where F_L, F_R are the exact fluxes in cells adjacent to the face of interest. Rearranged, this is the same as

$$S_i Q_i^* - F_i^* = S_i Q_i - F_i \tag{3.20}$$

which for the first term in Q and F, was demonststrated as

$$\begin{aligned} S_i\rho_i^* - \rho_i^*\tilde{U}_{l(R=L)}^* &= S_i\rho_i - \rho_i\tilde{U}_i \\ \rho_i^*(S_i - S^*) &= \rho_i(S_i - \tilde{U}_i) \\ \rho_i^* &= \rho_i\frac{S_i - \tilde{U}_i}{S_i - S^*} \end{aligned} \tag{3.21}$$

The other lines are substituted into (3.20) as well. For u-momentum:

$$\begin{aligned} S_i(\rho_i u_i)^* - (\rho_i u_i)^*\cancel{\tilde{U}_i^*}^{\tilde{U}^* = S^*} - p_i^* n_x &= S_i(\rho_i u_i) - (\rho_i u_i)\tilde{U}_i - p_i n_x \\ (\rho_i u_i)^* &= (\rho_i u_i)\frac{S_i - \tilde{U}_i}{S_i - S^*} + \frac{(p^* - p_i)n_x}{S_i - S^*} \qquad (3.22) \\ u_i^* &= \frac{(\rho_i u_i)(S_i - \tilde{U}_i)}{\rho_i^*(S_i - S^*)} + \frac{(p^* - p_i)n_x}{\rho_i^*(S_i - S^*)}. \qquad (3.23) \end{aligned}$$

Substituting (3.21) into (3.23),

$$u_i^* = u_i + \frac{(p^* - p_i)n_x}{\rho_i(S_i - \tilde{U})}. \tag{3.24}$$

Similarly,

$$(\rho_i v_i)^* = (\rho_i v_i)\frac{S_i - \tilde{U}_i}{S_i - S^*} + \frac{(p^* - p_i)n_y}{S_i - S^*} \tag{3.25}$$

or

$$v_i^* = v_i + \frac{(p^* - p_i)n_y}{\rho_i(S_i - \tilde{U})}. \tag{3.26}$$

Now, for the fourth line:

$$\begin{aligned} S_i E_{t_i}^* - (E_{t_i}^* + p^*)\tilde{U}^{\overset{S^*}{\nearrow}} &= S_i E_{t_i} - (E_{t_i} + p_i)\tilde{U}_i \\ E_{t_i}^*(S_i - S^*) - p^* S^* &= E_{t_i}(S_i - \tilde{U}_i) - p_i \tilde{U}_i \\ E_{t_i}^* &= E_{t_i}\frac{S_i - \tilde{U}_i}{S_i - S^*} + \frac{p^* S^* - p_i U_i}{S_i - S^*}. \end{aligned} \tag{3.27}$$

S^* is defined by

$$S^* = U_{hll}^* = \frac{\rho_R \tilde{U}_R(S_R - \tilde{U}_R) - \rho_L \tilde{U}_L(S_L - \tilde{U}_L) + p_L - p_R}{\rho_R(S_R - \tilde{U}_R) - \rho_L(S_L - \tilde{U}_L)}. \tag{3.28}$$

p^* is given by

$$p^* = \rho_i(\tilde{U}_i - S_i)(\tilde{U}_i - S^*) + p_i. \tag{3.29}$$

The Roe-Averaged Variables are defined by

$$
\begin{aligned}
R &= \sqrt{\frac{\rho_R}{\rho_L}} && (3.30)\\
\rho_{Roe} &= R\rho_L && (3.31)\\
u_{Roe} &= \frac{Ru_R + u_L}{1+R} && (3.32)\\
v_{Roe} &= \frac{Rv_R + v_L}{1+R} && (3.33)\\
\tilde{U}_{Roe} &= u_{Roe}n_x + v_{Roe}n_y && (3.34)\\
h_{0_{Roe}} &= \frac{Rh_{0_L} + h_{0_R}}{1+R} && (3.35)\\
a^2_{Roe} &= (\gamma-1)\left[h_{0_{Roe}} - \frac{1}{2}(u^2_{Roe} + v^2_{Roe})\right] && (3.36)
\end{aligned}
$$

where

$$h_0 = \frac{E_t + p}{\rho} \tag{3.37}$$

3.4 Calculation of Viscous Flux

3.4.1 Gradients – Green-Gauss Approach. The procedure for calculating a flux involves a diamond-shaped control volume, shown in Fig. 3(for an i-face). while

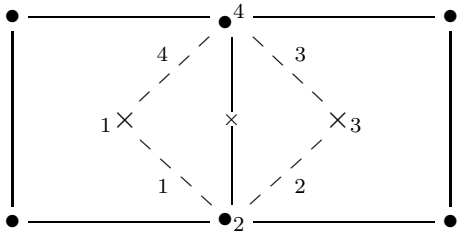

Figure 3: Control volume for viscous flux at an face of constant i

that for a j-face is depicted in Fig. 4. For i-faces, 1 and 3 are cell values, and 2 and 4 are node values. For j-faces, 1 and 3 are node values, and the 2 and 4 faces are cell values. Repeated here is the Green-Gauss Theorem:

$$\int_S \frac{\partial F_2}{\partial x} - \frac{\partial F_1}{\partial y} dS = \oint F_1 dx + F_2 dy \tag{3.38}$$

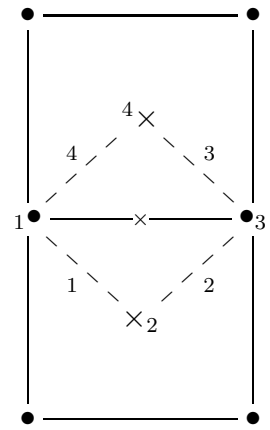

Figure 4: Control volume for viscous flux at an face of constant j

With $F_1 = 0$, $F_2 = G$ (G is a property within the flow such as u, v or T) and approximating the right hand side with constant values of u at each face, and, on realizing that in 2 dimensions $S \equiv \underline{V}$, (3.38) becomes

$$\int_S \frac{\partial F_2}{\partial x} dS = \overline{\frac{\partial G}{\partial x}} \underline{V} \approx \sum_{faces} G_{face,avg} \Delta y_{face} \tag{3.39}$$

where $\underline{V} = \frac{1}{2}(\Delta x_{13}\Delta y_{24} - \Delta x_{24}\Delta y_{13})$ Evaluating on the dotted control volume, this expression yields

$$\overline{\frac{\partial G}{\partial x}} \approx \frac{1}{\underline{V}} \left[\frac{1}{2}(G_1 + G_2)(y_2 - y_1) + \frac{1}{2}(G_2 + G_3)(y_3 - y_2) + \frac{1}{2}(G_3 + G_4)(y_4 - y_3) + \frac{1}{2}(G_4 + G_1)(y_1 - y_4) \right] \tag{3.40}$$

Expanding, obtain:

$$\begin{aligned} \overline{\frac{\partial G}{\partial x}} \approx \frac{1}{2\underline{V}} [\quad & - \cancel{G_1 y_1} + G_1 y_2 - G_2 y_1 + \cancel{G_2 y_2} - \cancel{G_2 y_2} + G_2 y_3 - G_3 y_2 + \cancel{G_3 y_3} - \cancel{G_3 y_3} + G_3 y_4 - G_4 y_3 \\ & + \cancel{G_4 y_4} - \cancel{G_4 y_4} + G_4 y_1 + \cancel{G_1 y_1} - G_1 y_4] \end{aligned} \tag{3.41}$$

Simplifying,

$$\overline{\frac{\partial G}{\partial x}} \approx \frac{1}{2\underline{V}} \left[(G_3 - G_1)\Delta y_{24} - (G_4 - G_2)\Delta y_{13} \right] \tag{3.42}$$

With $F_1 = G$, $F_2 = 0$ and approximating the right hand side with constant values of u at each face, and realizing that in 2 dimensions $S \equiv \underline{V}$, (3.38) becomes

$$\int_S \frac{\partial G_1}{\partial x} dS = \overline{\frac{\partial G}{\partial y}} \underline{V} \approx - \sum_{faces} G_{face,avg} \Delta x_{face} \tag{3.43}$$

and, by the same process as above,

$$\overline{\frac{\partial G}{\partial y}} \approx \frac{1}{2\underline{V}} \left[-(G_3 - G_1)\Delta x_{24} + (G_4 - G_2)\Delta x_{13} \right] \tag{3.44}$$

On substituting flow variables for (3.44), (3.42),

$$\overline{\frac{\partial u}{\partial x}} \approx \frac{1}{2\underline{V}} \left[(u_3 - u_1)\Delta y_{24} - (u_4 - u_2)\Delta y_{13} \right] \tag{3.45}$$

$$\overline{\frac{\partial u}{\partial y}} \approx \frac{1}{2\underline{V}} \left[-(u_3 - u_1)\Delta x_{24} + (u_4 - u_2)\Delta x_{13} \right] \tag{3.46}$$

$$\overline{\frac{\partial v}{\partial x}} \approx \frac{1}{2\underline{V}} \left[(v_3 - v_1)\Delta y_{24} - (v_4 - v_2)\Delta y_{13} \right] \tag{3.47}$$

$$\overline{\frac{\partial v}{\partial y}} \approx \frac{1}{2\underline{V}} \left[-(v_3 - v_1)\Delta x_{24} + (v_4 - v_2)\Delta y_{13} \right] \tag{3.48}$$

$$\overline{\frac{\partial T}{\partial x}} \approx \frac{1}{2\underline{V}} \left[(T_3 - T_1)\Delta y_{24} - (T_4 - T_2)\Delta y_{13} \right] \tag{3.49}$$

and

$$\overline{\frac{\partial T}{\partial y}} \approx \frac{1}{2\underline{V}} \left[-(T_3 - T_1)\Delta x_{24} + (T_4 - T_2)\Delta x_{13} \right] \tag{3.50}$$

The reader is reminded $\mu_B = \lambda - 2/3\mu$. Also, this expression is divided by reference Reynolds number, and the substitution

$$k = \frac{1}{(\gamma - 1)} \left(\frac{\mu_L}{Pr_L} + \frac{\mu_T}{Pr_T} \right) \tag{3.51}$$

is made, where for the present work $\mu_T = 0$

Now, if G represents a property within the domain, such as T, u, v, μ, then we can find a relationship for node values in terms of an average of surrounding cells. Figure 5 contains a diagram for reference.

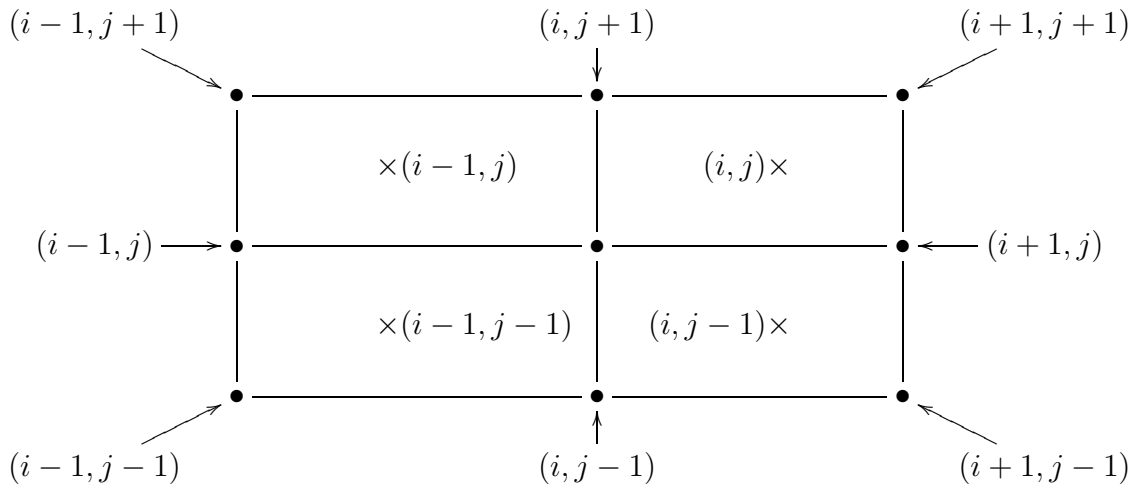

Figure 5: Viscous flux stencil diagram

One way to get the value at a node, which will be used, is by simple averaging

$$G_{node,i,j} = \frac{1}{4}(G_{cell,i-1,j} + G_{cell,i,j} + G_{cell,i-1,j-1} + G_{cell,i,j-1}) \tag{3.52}$$

Now for an i-face, in this case the left face of cell (i, j), by Fig 3:

$$G_1 = G_{cell,i-1,j} \tag{3.53}$$

$$G_2 = G_{node,i,j} \tag{3.54}$$

$$G_3 = G_{cell,i,j} \tag{3.55}$$

$$G_4 = G_{node,i,j+1} \tag{3.56}$$

$$\text{and } G_{i-face,i,j} = \frac{1}{2}(G_2 + G_4) \tag{3.57}$$

For a j-face, in this case the bottom face of cell (i, j)

$$
\begin{aligned}
G_1 &= G_{node,i,j} && (3.58)\\
G_2 &= G_{cell,i,j-1} && (3.59)\\
G_3 &= G_{node,i+1,j} && (3.60)\\
G_4 &= G_{cell,i,j} && (3.61)\\
\text{and } G_{j-face,i,j} &= \frac{1}{2}(G_1 + G_3) && (3.62)
\end{aligned}
$$

Now, we can write the viscous fluxes as defined in §2.4 of Blazek [57], trading n_x and n_y for A_x and A_y, since area-scaled fluxes are used in AFIT-2D:

$$
f_{i,j} = \begin{bmatrix} 0 \\ A_x\tau_{xx} + A_y\tau_{xy} \\ A_x\tau_{xy} + A_y\tau_{yy} \\ A_x\Theta_x + A_y\Theta_y \end{bmatrix} \tag{3.63}
$$

All information needed for either an i-face or j-face in (3.45)-(3.62) is now available.

3.5 Calculation of Time Step

The time step of the simulation in the case of an explicit time integration scheme such as the second order Runge-Kutta total variation diminishing scheme is computed in cell (i, j) according to

$$
\Delta t_{i,j} = \frac{\Omega^{i,j}}{(\hat{\Lambda}_c^I + \hat{\Lambda}_c^J)_{i,j} + C(\hat{\Lambda}_v^I + \hat{\Lambda}_v^J)_{i,j}} \tag{3.64}
$$

where $\Omega^{i,j}$ is the volume cell (i, j). $\hat{\Lambda}_c$ is the maximum eigenvalue of the convective flux jacobian (the spectral radius).

3.6 Viscosity in the Implicit Operator of the LUSGS Scheme

The implicit time integration scheme of Yoon and Jameson [58] is employed for this work. In this scheme the implicit operator is approximately factored in three parts:

$$(D+L)D^{-1}(D+U)\Delta\vec{W}^n = -\vec{R}_I^n \tag{3.65}$$

where D represents the diagonal terms of the operator, L represents the lower triangular terms, U represents the upper triangular terms, $\Delta\vec{W}^n$ represents the change in the solution at time level n, and $\vec{R}_I^n$ represents the residual, or explicit spatial operator.

For the Euler equations, the D^{-1} term is computed as:

$$D^{-1} = \frac{1}{\frac{\underline{V}}{\Delta t} + \omega(\hat{\Lambda}_c^I + \hat{\Lambda}_c^J)} \tag{3.66}$$

(the identity matrix is implied/applied in the code).The average areas are used here and below for the visous case, in D^{-1}. The viscous form is that of equation (6.53) in Blazek [57:206]. First, computing viscous spectral radii:

$$\hat{\Lambda}_v^I = \max\left(\frac{4}{3\rho}, \frac{\gamma}{\rho}\right)\left(\frac{\mu_L}{Pr_L} + \frac{\mu_T}{Pr_T}\right)\frac{(A^I)^2}{\underline{V}} \tag{3.67}$$

$$\hat{\Lambda}_v^J = \max\left(\frac{4}{3\rho}, \frac{\gamma}{\rho}\right)\left(\frac{\mu_L}{Pr_L} + \frac{\mu_T}{Pr_T}\right)\frac{(A^J)^2}{\underline{V}} \tag{3.68}$$

where the code has taken $\gamma > 4/3$ as hard-coded. When adding bulk viscosity, $4\mu/3$ immediately becomes $4\mu/3 + \mu_B$. From this viscous spectral radius, D^{-1} becomes:

$$D_{visc}^{-1} = \frac{D_{lam}^{-1}}{1 + 2D_{lam}^{-1}(\hat{\Lambda}_v^I A^I + \hat{\Lambda}_v^J A^J)}. \tag{3.69}$$

By equations (6.51) in Blazek [57:205], and the spectral radius simplification, $L\Delta Q$ and $U\Delta Q$ become

$$L\Delta Q_{visc} = L\Delta Q_{lam} + \hat{\Lambda}_v^I \Delta Q_{i-1,j} + \hat{\Lambda}_v^J \Delta Q_{i,j-1} \tag{3.70}$$

and

$$U\Delta Q_{visc} = L\Delta Q_{lam} - \hat{\Lambda}_v^I \Delta Q_{i+1,j} - \hat{\Lambda}_v^J \Delta Q_{i,j+1}. \tag{3.71}$$

3.7 Grid Adaption

To align the cells with the shock the procedure of Gnoffo, Hartung, and Greendyke is used [38:2–3]. This simple, structured-grid, algebraic, line-by-line procedure assumes one of the curvilinear grid coordinates moves from the body surface to the freestream. One transformation is used to resolve the boundary layer, based on a user-input Reynolds number based on cell height. A second transformation is performed to normalize the far field "away from body" distance equal to one. The shock location is determined by sensing a user-input fraction above the freestream density, pressure or temperature, marching from the freestream to the body. The final transformation is made to pull grid points to this shock location. The free stream-side outer boundary is placed a user-specified distance beyond the sensed shock location. This procedure is carried out for every value of non-surface-normal grid coordinate, on the face centers, and the nodes are placed by simple averages of those face center positions.

To modify this procedure to accommodate concave geometries (such as will be used in this work, see section 3.10, rather than average the face centers directly, an additional constraint restricts motion of the nodes to the line on which they were originally placed. This option is specified in the input file as "`preserve vectors :: 1`." With this option, initial grids were constructed so as to avoid constant-η node lines crossing and causing a grid "folded over" on itself. This subroutine, in Fortran 95, can be found in Appendix A.

3.8 Boundary Conditions

The boundary conditions typically used for Navier-Stokes CFD involve no slip at the wall, and no pressure gradient at the wall. Then, the only property left to specify is the temperature gradient, or temperature of the wall. For the blow-down tunnel

experimental runs, the constant wall temperature boundary condition is appropriate.

$$\frac{dp}{dn} = 0 \tag{3.72}$$

$$u = v = 0 \tag{3.73}$$

$$T_w = \text{const} \tag{3.74}$$

In a cell-centered finite volume code such as AFIT-2D, the boundary conditions are not specified directly at the surface, but are rather specified at a "ghost cell" outside the flow domain. The cell interface is the wall, and the ghost cell properties can be set such that the flux scheme will match the condition of no mass flow through the cell face, or in this case, calculate zero flow velocity at the cell face. In AFIT-2D, the nondimensional pressure, temperature, and temperature are related by

$$T = \frac{\gamma p}{\rho} \tag{3.75}$$

To set the pressure gradient to zero is simply done by copying the interior cell pressure, p_i, to the ghost cell, p_g:

$$p_g = p_i = p \tag{3.76}$$

To set the temperature of the wall to the desired temperature, an extrapolation from inside the domain to outside is performed:

$$T_w = \frac{1}{2}(T_g + T_i) \tag{3.77}$$

or

$$T_g = 2T_w - T_i \tag{3.78}$$

or, in terms of pressure and temperatures

$$\frac{\gamma p}{\rho_g} = 2T_w - \frac{\gamma p}{\rho_i} \tag{3.79}$$

Rearranging for ρ_g, we obtain

$$\rho_g = \frac{\rho_i}{\frac{2T_w\rho_i}{(\gamma p)} - 1} \tag{3.80}$$

Immediately, one major problem can be seen with this scheme, in that a value of wall temperature of 1/2 the adjacent cell temperature will cause an undefined value, or in other words, this expression for the external density has a singularity, Also, lower temperatures lead to an unphysical negative density. To prevent this situation in the present work, the wall temperature will be set to a value no less than 3/4 of the temperature in the adjacent cell:

$$T_{w_{set}} = \max\left(T_w, \frac{3}{4}\left(\frac{\gamma p}{\rho_i}\right)\right) \tag{3.81}$$

3.9 One Dimensional Shock Solver

The first test of bulk viscosity will be a normal shock profile, using a one dimensional, direct integration of the Navier Stokes equations. The 1-D integration code follows the method outlined in Gilbarg and Paolucci [37].

To illustrate the effect of bulk viscosity on shock structure, the one-dimensional steady state Navier-Stokes equations are solved with the Runge-Kutta ODE solver. The results can then be compared to the observations of Alsmeyer [25] for shock thickness in low-density nitrogen. The procedure of Gilbarg and Paolucci [37, 59] as implemented by Camberos and Chen [60] is followed. where Navier-Stokes equations in one dimension are solved:

$$\frac{d}{dx}\begin{pmatrix} \rho u \\ \rho u^2 + p \\ (E_t + p)U \end{pmatrix} = \frac{d}{dx}\begin{pmatrix} 0 \\ (\frac{4}{3}\mu + \mu_b)\frac{du}{dx} \\ \frac{\mu}{(\gamma-1)Pr)}\frac{dT}{dx} + (\frac{4}{3}\mu + \mu_b)\frac{du}{dx}u \end{pmatrix} \tag{3.82}$$

which, on integrating, become

$$\rho u = A \tag{3.83}$$

$$\rho u^2 + \frac{\rho T}{\gamma} - \left(\frac{4}{3}\mu + \mu_b\right)\frac{du}{dx} = B \tag{3.84}$$

$$(E_t + p)u - \frac{\mu}{(\gamma-1)Pr}\frac{dT}{dx} - \left(\frac{4}{3}\mu + \mu_b\right)\mu u\frac{du}{dx} = C \tag{3.85}$$

rearranging these for $u_x = du/dx$ and $T_x = dT/dx$, we obtain

$$u_x = -\frac{3}{4\mu}\left(B - Au - \frac{AT}{2u}\right) \tag{3.86}$$

and

$$T_x = \frac{(\gamma-1)Pr}{\mu}\left(\frac{-1}{2}Au^2 + \frac{3}{4}AT - C + Bu\right) \tag{3.87}$$

These two ODEs are integrated using an adaptive Runge-Kutta scheme, such as `ODE45` in Matlab® or `NDSolve` in Mathematica®. The latter is used in this work.

The boundary conditions used are those of the familiar calorically perfect normal shock relations [41:86-94]:

$$\frac{\rho_2}{\rho_1} = \frac{(\gamma-1)M^2}{2 + (\gamma-1)M^2)} \tag{3.88}$$

$$\frac{u_2}{u_1} = \frac{\gamma-1}{\gamma+1} + \frac{2}{(\gamma+1)M^2} \tag{3.89}$$

Note that continuity, equation (3.83), requires equation (3.89) to be the reciprocal of equation (3.88).

$$\frac{p_2}{p_1} = \frac{2\gamma}{\gamma+1}M^2 - \frac{\gamma-1}{\gamma+1} \tag{3.90}$$

$$\frac{T_2}{T_1} = \frac{h_2}{h_1} = \frac{p_2}{p_1}\frac{\rho_1}{\rho_2} \tag{3.91}$$

Note that relationships for a more general case than the calorically perfect gas can also be written in terms of "thermodynamic variables" only, as shown in Anderson [41:98–

101], giving the commonly known Rankine-Hugoniot equation:

$$e_2 - e_1 = \frac{p_1 + p_2}{2}(\nu_1 - \nu_2) \tag{3.92}$$

where ν is the specific volume. This equation holds no matter the thermodynamic model, however, the states 1 and 2 are equilibrium states.

3.10 Axisymmetric Test Cases

The second two test cases involve run 5 and run 7 from the CUBRC [1], for which experimental wall data for pressure and heating is available. Solutions are computed with AFIT-2D, and compared to experiment and DSMC solutions from Carr [11]. The effect on the surface pressure and heating to changes in bulk viscosity will be analyzed. Freestream properties are listed in Table 2. The geometry of run 5 is depicted in Figure 6, and that of run 7 is depicted in Figure 7.

Table 2: Freestream, Wall Conditions for CUBRC Data

Run	Ma	Re	T_∞ (K)	P_∞ (Pa)	ρ_∞ (kg/m^3)	V_∞ (m/s)	T_{wall} (K)	Kn
5	15.3	23746	52.28	2.523	0.00016	2252.47	303.33	0.0014
7	15.6	26624	42.61	2.227	0.00018	2072.64	297.22	0.0014

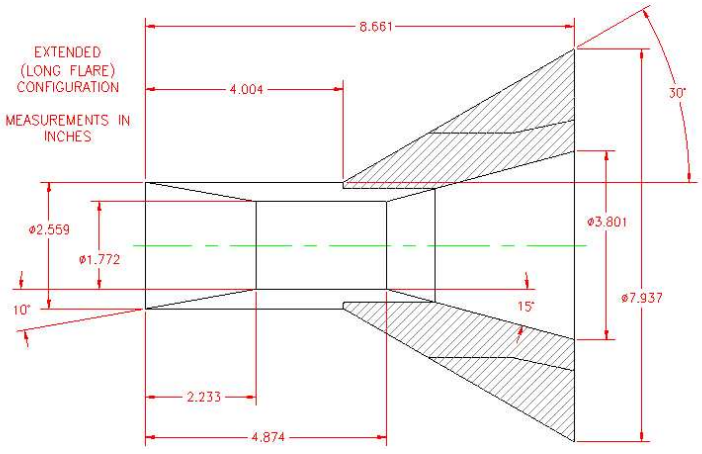

Figure 6: Geometry of Run 5, from Holden and Wadhams [1]

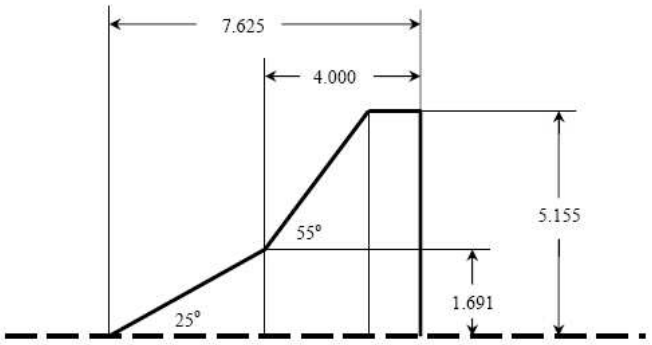

Figure 7: Geometry of Run 7, from Holden and Wadhams [1]

IV. Results

4.1 Shock Structure

The inclusion of the bulk viscosity model of Capelletti et al in the Navier-Stokes equations improves shock thickness, as can be seen in Figure 8. This figure shows inverse shock thickness, as defined by

$$\frac{1}{t_s} = \max \frac{d\rho_n}{dx/\lambda_1} \tag{4.1}$$

where

$$\rho_n = \frac{\rho - \rho_1}{\rho_2 - \rho_1} \tag{4.2}$$

Here, ρ_1 is the pre-shock density, ρ_2 is the post-shock density, and λ_1 is the pre-shock (or freestream) mean free path, defined by Alsmeyer [25:499-500]. The red line is the inverse shock thickness calculated from Alsmeyer's original electron-beam density observations. These observations were taken at $p = 50$ mTorr, or 6.67 Pa, and at a temperature of 300K. Note that the low Mach number shocks are relatively thick. The shock thickness decreases to a minimum between $Ma = 4$ and $Ma = 6$, and then increases again as the Mach number increases. The DSMC solution, from Bird, agrees quite well with these measurements. The Navier-Stokes solutions, calculated using the Sutherland model for shear viscosity, and no bulk viscosity predict a thinner shock than the observations. They predict a decreasing shock thickness with increasing Mach number, through the Mach number range of the observations. A large error is seen, comparing to the observations. The constant bulk viscosity solutions, while closer to the observations, still predict a thinning of the shock throughout the observed range. The Navier-Stokes solutions with the temperature-dependent bulk viscosity model from Cappelletti et al [36] present a significant improvement over the previous two, for Mach numbers up to 8. At $Ma = 9$ and $Ma = 10$, this model predicts thinner shocks, almost the same thickness as those of the constant bulk viscosity solutions. It should be noted the post-shock temperatures exceed the range of temperatures of the curvefit equation 2.24, and indeed, far exceed the temperature at which vibrational

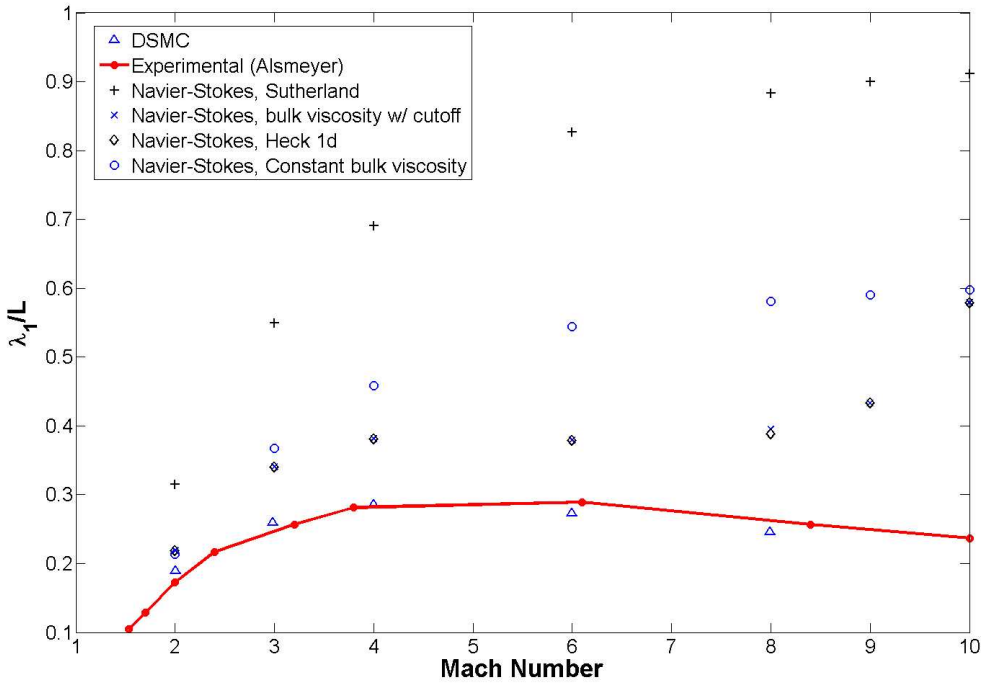

Figure 8: Effect of bulk viscosity on shock thickness

modes are expected to dominate the nonequilibrium behavior of the flow. This same problem does not occur with the two dimensional examples discussed below, due to their very low freestream temperature.

Figures 9 (a) and (b) show the normalized density profiles as defined by Eq (4.2), at $Ma = 4$ and $Ma = 6$. Here again, for the bulk viscosity models, the thicker shock can be seen, but also the distance of the shock from the downstream boundary condition can be seen. This distance can be though of as a "relaxation distance." The relaxation time present in the rotational collision number is physically visible in the shock solution. The two are related by convection. It is worth mentioning again that the jump conditions have not changed, including those for entropy. The thicker shock may give a lower peak entropy generation. A note of caution, however, is in order. Any claim of the validity of the bulk viscosity model based on continuum breakdown parameters, such as entropy generation, would be premature speculation without further study.

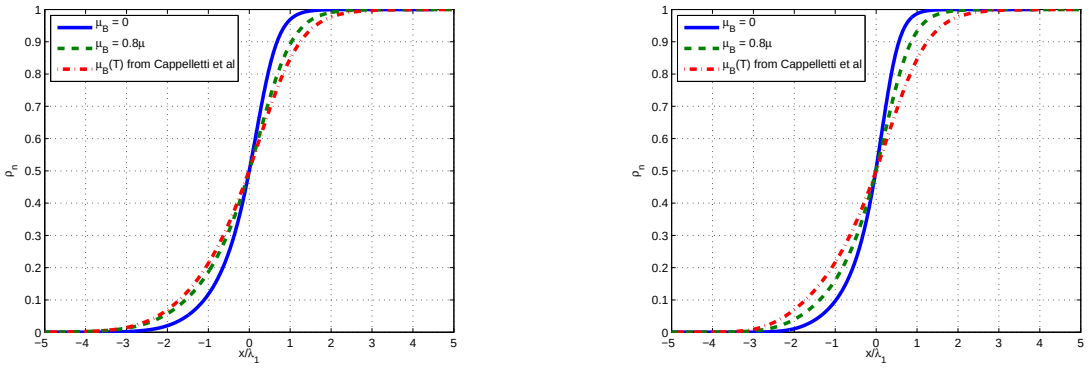

(a) $Ma = 4$ (b) $Ma = 6$

Figure 9: Normalized density profiles

4.2 Hollow Cylinder Flare Analysis

The hollow cylinder flare flow, in the cylinder region, is very similar to a flat plate flowfield. The surface of the body is aligned with the flow. The researchers at CUBRC have carefully created a sharp leading edge, sharp enough that no lip radius is given. This situation results in a nearly attached leading edge shock, accompanied by a very high temperature and heating rate. This portion of the body is where the constant temperature wall listed in the CUBRC run 5 conditions, shown in Table 2 would not be expected to hold. In fact, none of the thin-film heat transfer gauges or pressure sensors on the body are located near this point [1]. A boundary layer forms on the surface, with a weak shock bounding its upper surface. This boundary layer contains high temperatures, as the flow is slowed considerably in this boundary layer from the freestream, and the kinetic energy contained therein is converted to thermal and internal energy, here in the form of rotational energy. To be fair, the region near the stagnation point should be hot enough to excite some vibration, but its overall effect on the flow is here assumed to be small. The density predicted in the continuum simulations in this boundary layer is actually lower than that of the freestream. This feature can be seen in Figure 11 (a) through (c). In the calorically perfect gas assumption, the thermodynamic pressure, density, and temperature are

related by $T \propto \gamma p/\rho$, where γ is the ratio of specific heats. When temperature increases, at nearly the same pressure (see the boundary pressure contour plots in Figure 10), the density must decrease.

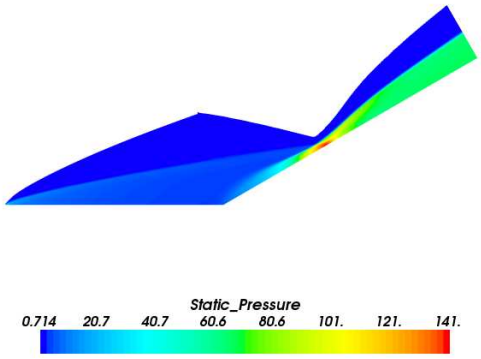

(a) $\mu_B = 0$

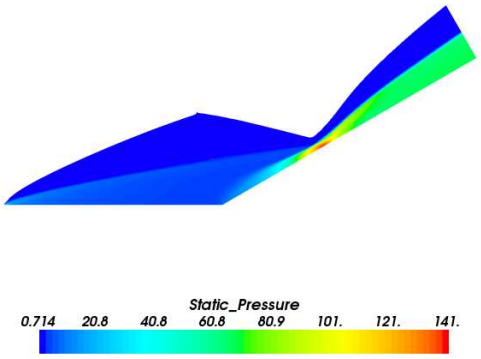

(b) $\mu_B = 0.8\mu$

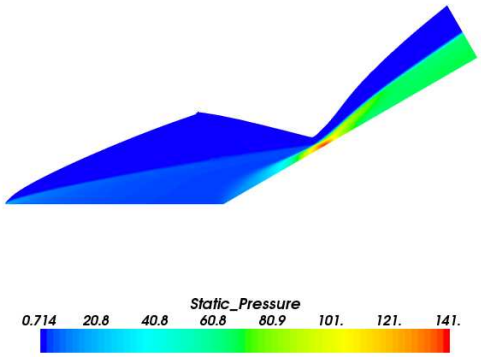

(c) μ_B from Cappelletti et al [36]

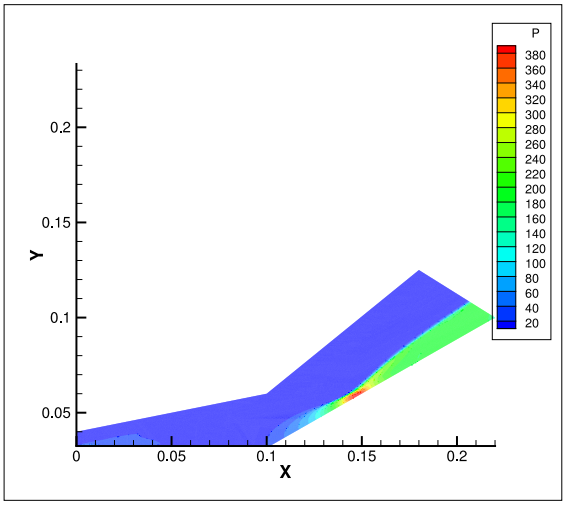

(d) DSMC from Carr [11]

Figure 10: Hollow cylinder pressure

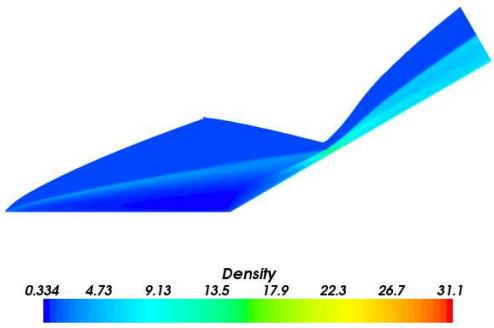

(a) $\mu_B = 0$

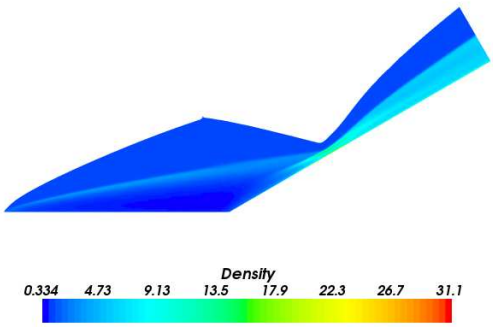

(b) $\mu_B = 0.8\mu$

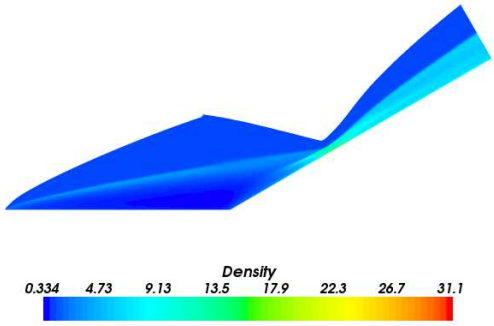

(c) μ_B from Cappelletti et al [36]

Figure 11: Hollow cylinder density

The next feature present in the continuum solutions, is a gradual increase in density and pressure as the boundary layer is turned at the start of the flare, as can be seen in Figures 11 and 10. The leading edge of this pressure and density increase, begins to exhibit a shock-like structure, when following it toward its apparent intersection with the boundary layer edge shock. This feature is best seen in the density contour plots of Figure 12. This region is an example of shock-boundary layer interaction. The problem of shock-boundary layer interaction at hypersonic speed has caused serious damage to vehicles. For example, the X-15, while testing a dummy ramjet attached a pylon on the bottom of the aircraft, experienced a loss of this pylon due the shock from the ramjet model impinging on the pylon boundary layer [17:562-565]. This region is one of very high pressure as can be seen in Figure 10. Figure 13 depicts pressure coefficient as a function of axial distance from the leading edge of the flare. The CFD predictions of surface pressure match those experimentally observed at CUBRC quite well in cylinder region. The pressure rise on the flare, through the shock impingement point is slightly underpredicted by all three CFD solutions. The portion of the surface aft of the impingement shows an underprediction of pressure in the expansion region. It should be noted that this feature was also predicted in a finer grid with AFIT-2D, and also in the much finer, unstructed grid FLUENT®solution of Carr [11:52]. From these observations, it can be speculated that the disagreement in pressure in this expansion region is less related to grid convergence, and more related to a shortcoming in the model of the physics of the CFD and DSMC solutions.

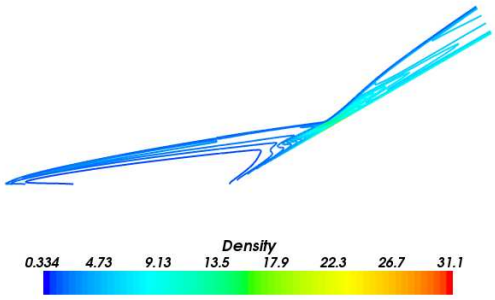

(a) $\mu_B = 0$

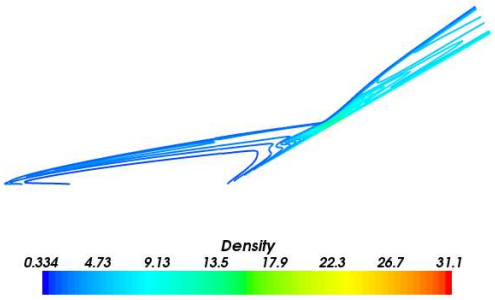

(b) $\mu_B = 0.8\mu$

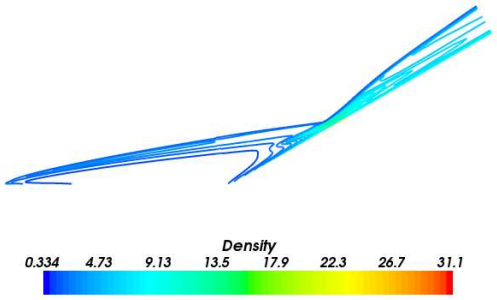

(c) μ_B from Cappelletti et al [36]

Figure 12: Hollow cylinder density contours

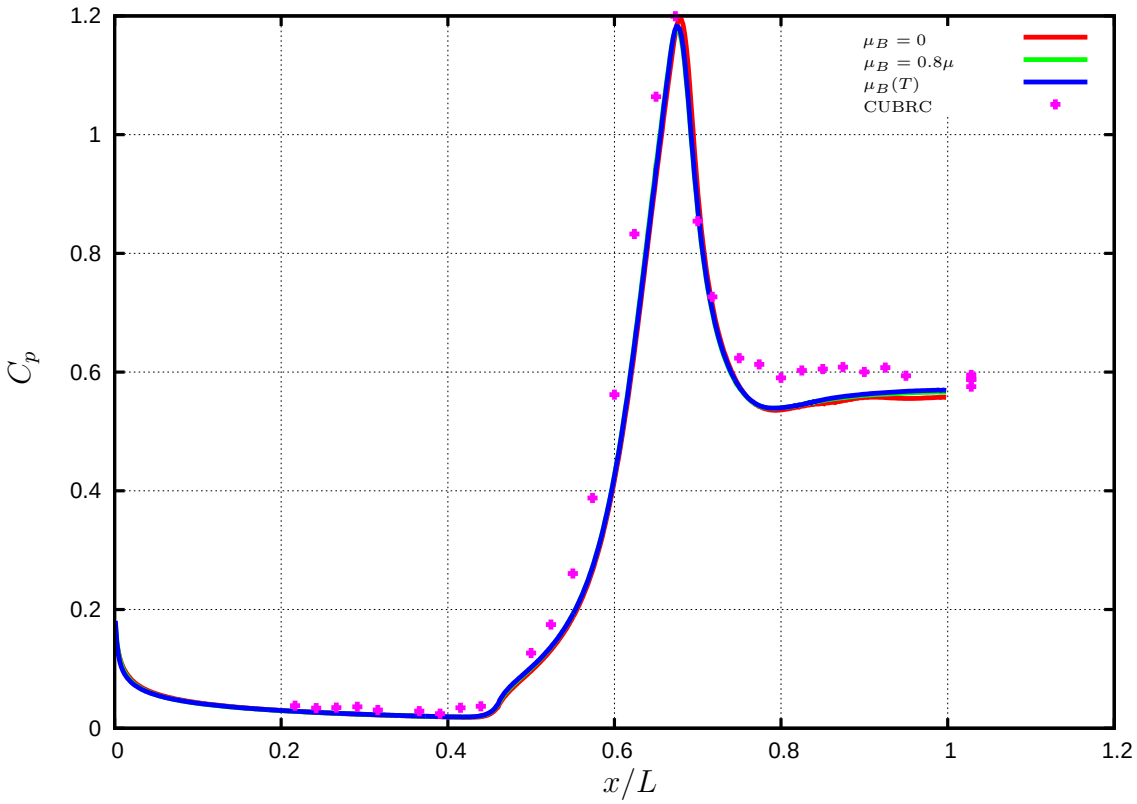

Figure 13: Hollow cylinder surface pressure coefficient

Figure 14 depicts Stanton number, or normalized heat transfer at the wall. In this figure can be seen that the CFD predictions of heat transfer are not far the experimentally observed. The bulk viscosity models both seem to provide some improvement in heat transfer prediction over the zero bulk viscosity CFD, in the forward side of the imingement point, and in heat transfer predicted in aft of the impingment point, near the end of the body.

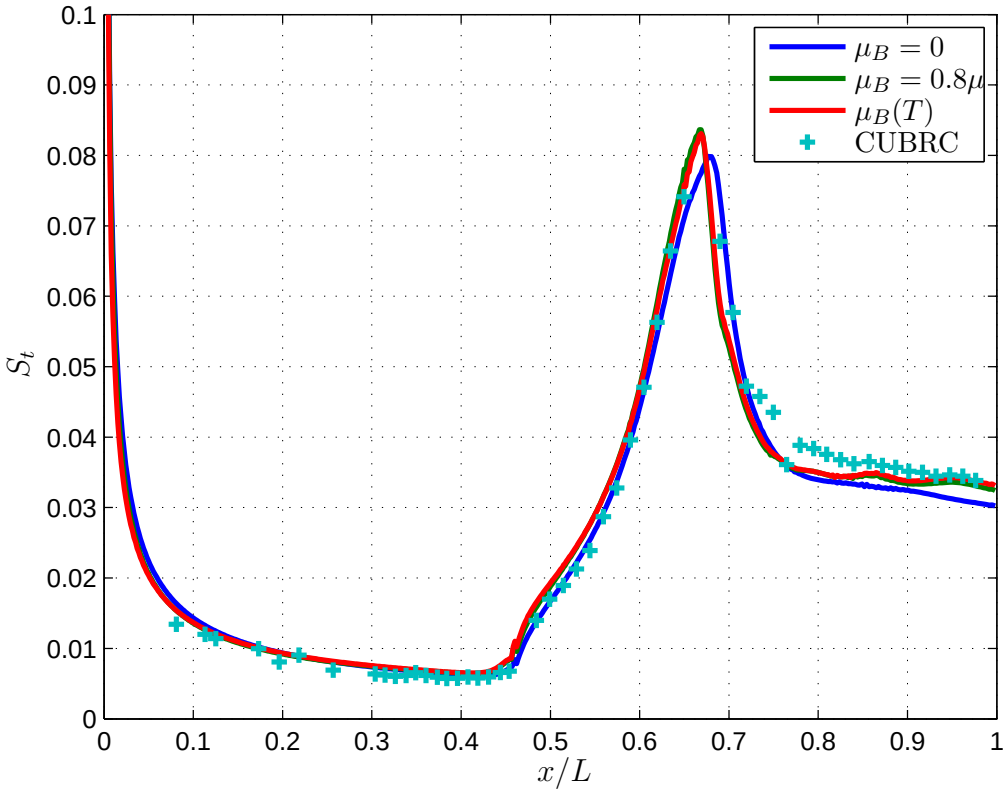

Figure 14: Hollow cylinder Stanton number

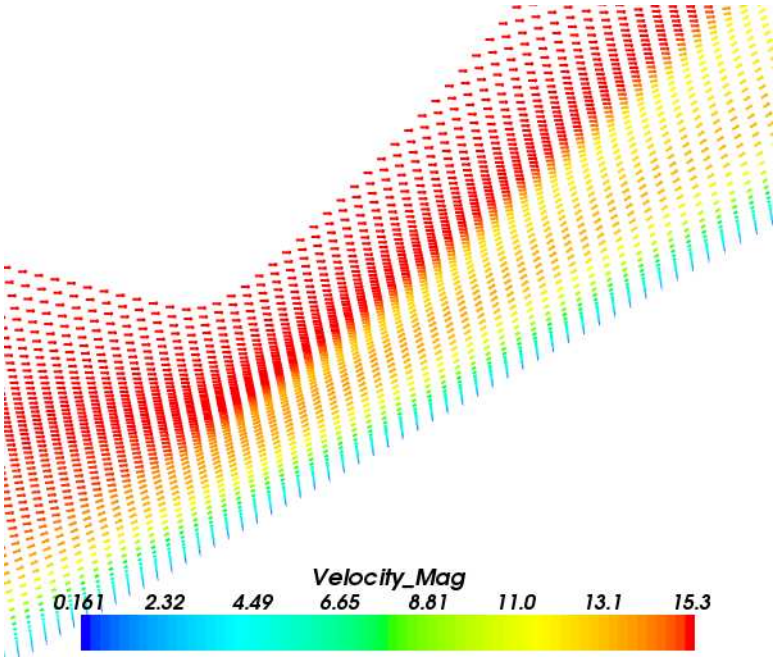

Figure 15: Hollow cylinder velocity vector detail: $\mu_B = 0$

The downstream side of the interaction point includes two features. The first being the outer edge of the shock layer, which appears to approach the slope of the shock developing out of the boundary layer, mentioned above. The second feature is less like a shock. The momentum and energy flowing through this area form a conical "sheet" of high-velocity flow, in the expanding region between the flare and the edge of the shock layer. The velocity vectors in the closeup of figure 15 show the detail of this feature. Traversing the flare portion of the shock layer edge, a higher than freestream density part of the flow can be seen at the interaction point. This region is the cylinder portion of the shock layer. A gradual relaxing of the shock angle can be seen moving downstream. This high pressure high density region expands and accelerates between the shock layer edge and the wall. The effect of bulk viscosity on these solutions is visible in Figures 12 and 16. Figures 12 (b) and (c) depict a wider shock at the edge of the shock layer than does Figure 12 (a). Also, the shock feature developing in the boundary layer, ahead of the interaction point is thicker. Overall shock layer thickness is not greatly affected.

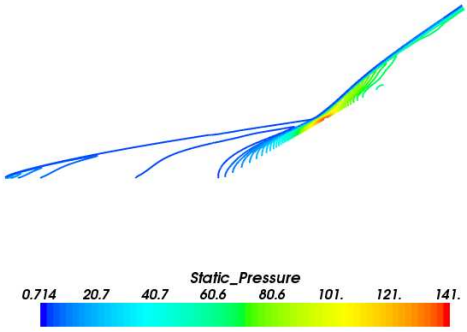

(a) $\mu_B = 0$

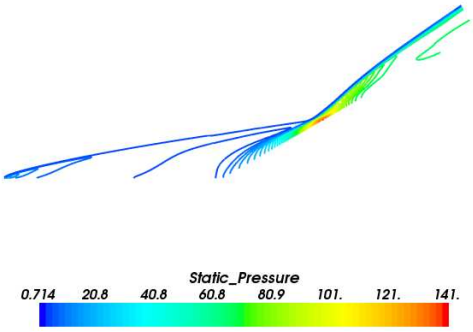

(b) $\mu_B = 0.8\mu$

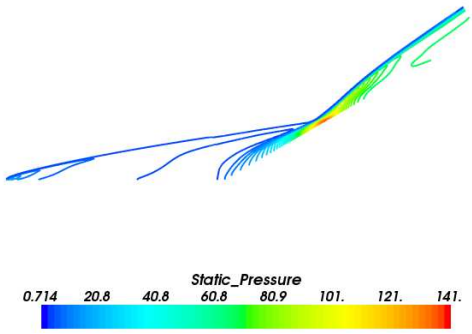

(c) μ_B from Cappelletti et al [36]

Figure 16: Hollow cylinder pressure contours

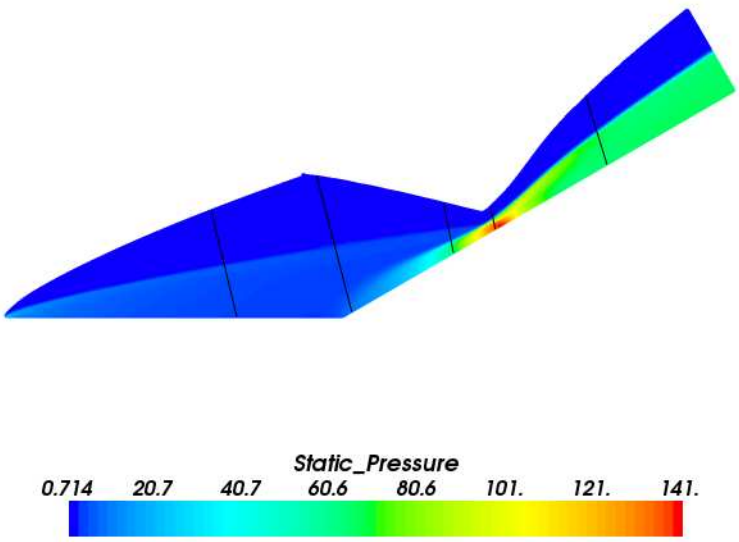

Figure 17: Hollow cylinder pressure comparison locations

Figure 17 depicts several grid line cuts, where pressure information has been extracted from both the CFD and the DSMC. The first cut is taken ahead of the compression corner. The second is taken just after the corner, where there should be higher pressure at the wall. The third cut is taken where the compression should be well-developed, just before the high pressure shock-impingement region. The fourth cut is near the maximum pressure point. The fifth cut is taken past the impingement, capturing the high-velocity "sheet."

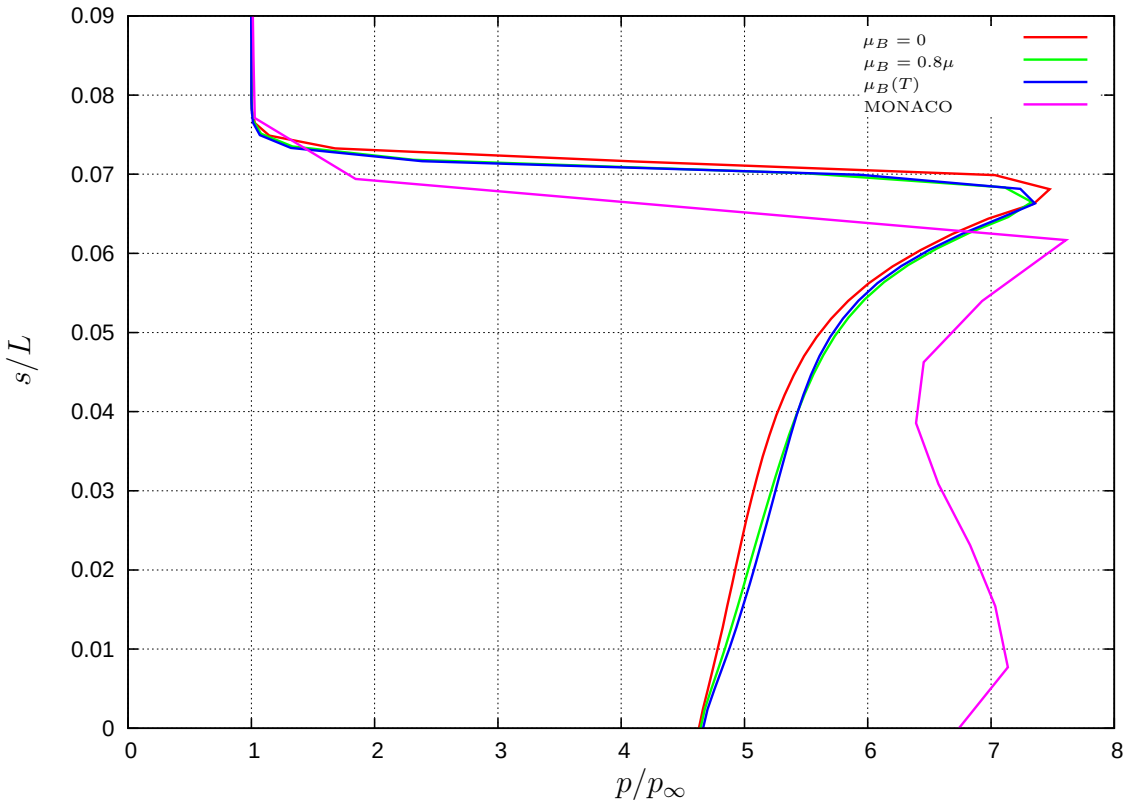

Figure 18: Extraction of pressure data, run 5, $x/L = 0.32$, $i = 175$

Figures 18 through 22 represent extractions of pressure contours taken on constant values of ξ, or i, shown in Figure 17, from the three CFD solutions, and the DSMC solutions from Carr [11]. Carr's DSMC solutions here presented were computed with Boyd's MONACO DSMC solver [61]. Figure 18 compares pressure profiles between the three CFD solutions, and the MONACO DSMC solution computed by Carr [11]. This extraction of pressure information was taken in the cylinder region, slightly ahead of the flare. The CFD solutions predict a slightly thicker shock layer, and an overall thinner shock than does MONACO. The CFD solutions computed with both constant bulk viscosity and the temperature dependent bulk viscosity predict a slightly thicker shock, and a slightly thinner shock layer than does the zero bulk viscosity CFD solution. The MONACO solution predicts a local pressure peak near the wall, a feature not predicted by the CFD solutions. Figure 19 compares pressure profiles along constant grid coordinate $i = 263$. This extraction of pressure informa-

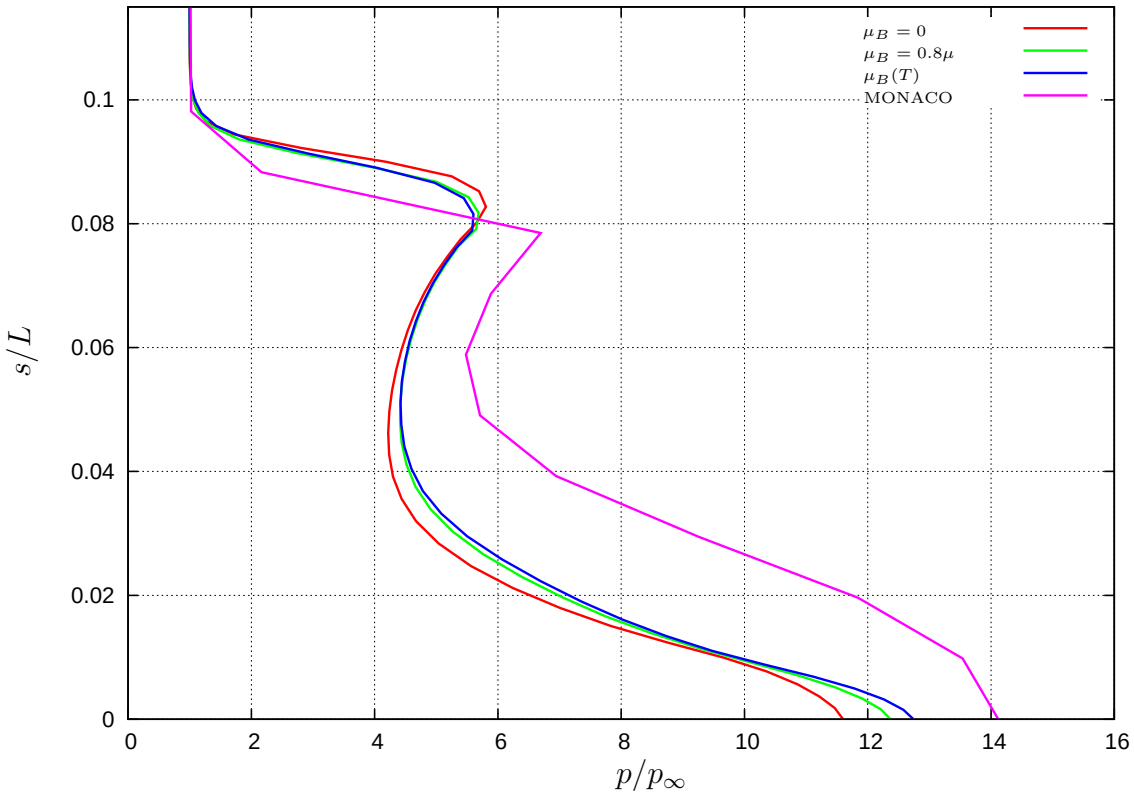

Figure 19: Extraction of pressure data, run 5, $x/L = 0.48$, $i = 263$

tion was taken near the junction of the cylinder and flare. The CFD solutions predict a slightly thicker shock layer, and an overall thinner shock than does MONACO. The shock thickness in the case of both constant bulk viscosity and that of the temperature dependent model predict a slightly thicker shock, and a slightly thinner shock layer than . The MONACO solution predicts slightly higher pressure at the wall than that predicted by the three CFD solutions. There is a qualitative similarity of the four profiles not seen in the $i = 175$ cut of Figure 18. Figure 20 compares pressure profiles at $i = 348$, or slightly ahead of the shock-boundary layer interaction region, as seen in Figure 17. The three CFD solutions predict a thinner shock than does the MONACO DSMC, and here a slightly thicker shock layer. The presence of two shocks can be seen here. The outer, weak boundary layer shock of the cylinder region can be seen in the upper left. Note that the constant bulk viscosity and temperature dependent bulk viscosity have brought this shock, and hence the overall shock layer thickness down

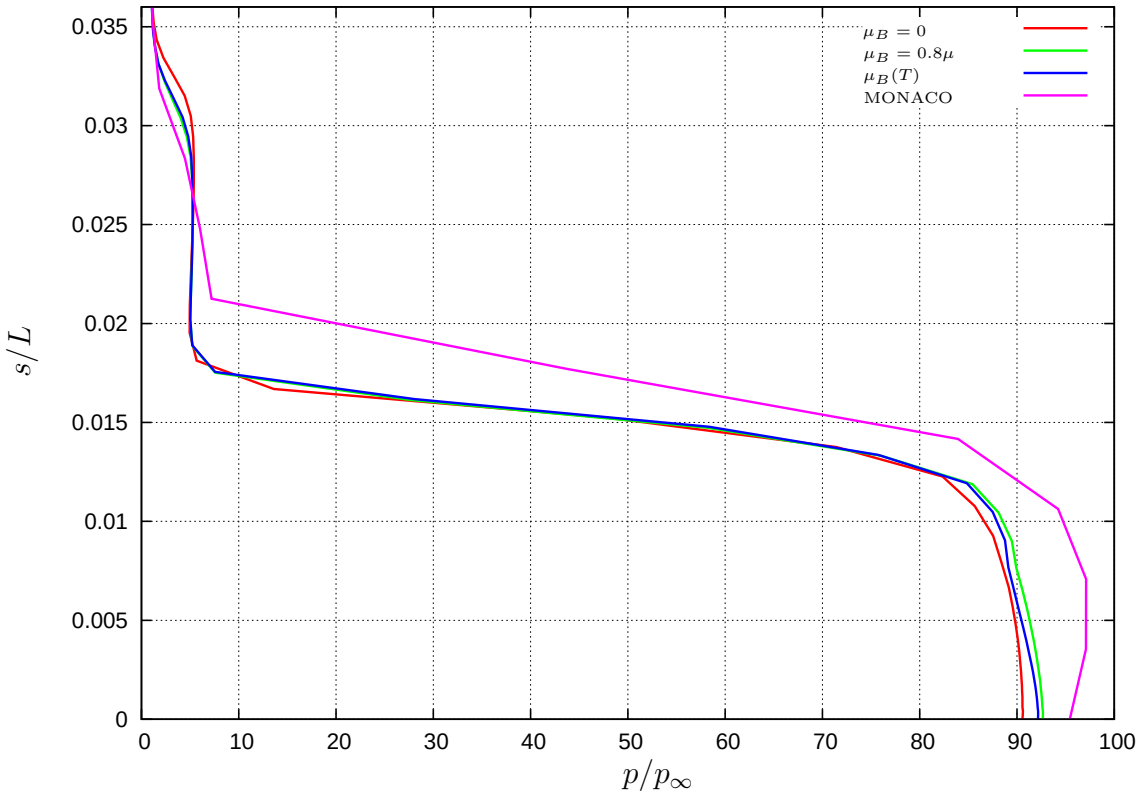

Figure 20: Extraction of pressure data, run 5, $x/L = 0.62$, $i = 348$

closer to that of the MONACO DSMC. This shock thickness is also slightly increased by the inclusion of bulk viscosity. The inner, stronger shock is predicted closer to the body than the DSMC solution by all three CFD solutions. The inner shock is also predicted to be thinner than the inner shock predicted by DSMC. The effect of bulk viscosity on this inner shocks thickness is minimal. The wall pressure predicted by CFD solutions including bulk viscosity is higher than without, and closer to that predicted by DSMC. Figure 21 compares pressure profiles in the shock impingement region, where pressure is expected to be highest, as depicted in Figure 17. The three CFD pressure profiles again show a similar shape to that of the DSMC. The shock predicted by DSMC is thicker, as is the shock layer. The constant and temperature-dependent bulk viscosity CFD solutions predict a thicker shock than does the CFD solution computed with no bulk viscosity. The pressure at the surface is predicted by all three CFD solutions is higher than that predicted by DSMC. It should be noted

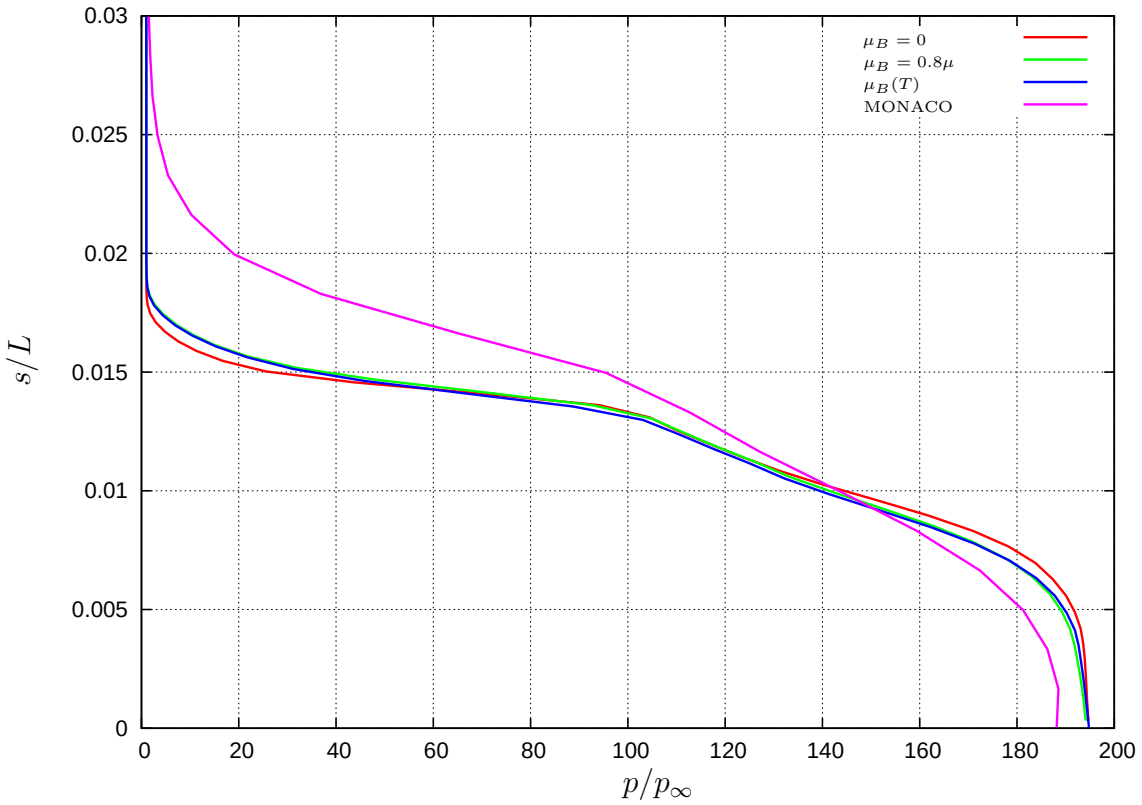

Figure 21: Extraction of pressure data, run 5, $x/L = 0.67$, $i = 380$

that the CFD surface pressure is in closer agreement to the experimentally observed surface pressure [11:52]. Figure 22 compares pressure profiles past the impingement point. This extraction is represented as the aft-most white line in Figure 17. It should be mentioned that at this point the CFD solution is in better agreement with experimental surface pressure than is the DSMC solution of Carr, and the DSMC solution predicts the shock-boundary layer interaction point to be farther upstream than do the CFD solutions [11:52]. The CFD solutions predict a slightly thinner shock and shock layer than does the DMSC. The effect of bulk viscosity in the CFD solutions is a thicker predicted shock than that predicted by the zero bulk viscosity CFD solution.

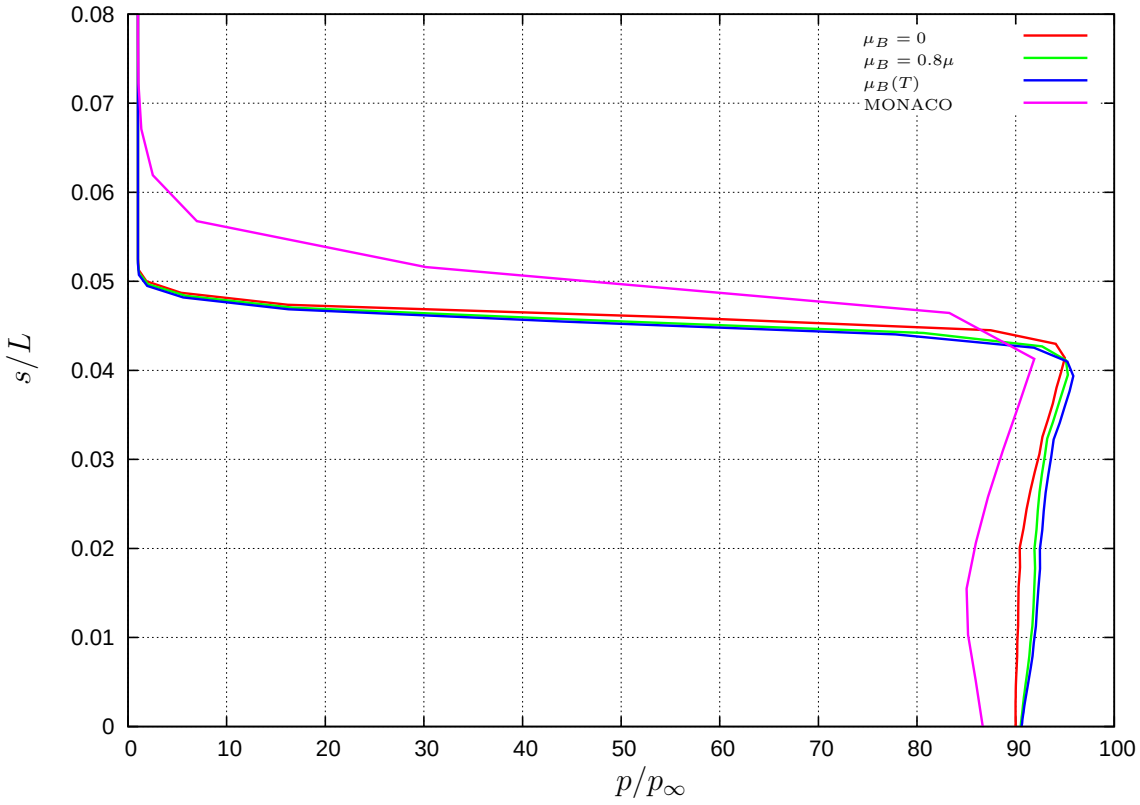

Figure 22: Extraction of pressure data, run 5, $x/L = 0.83$, $i = 450$

4.3 Double Cone Analysis

The double cone flow is slightly more complicated than that of the hollow cylinder flare. A thin shock layer is present on the forward 25° cone. As in the previous solution, the leading edge is sharp. It should be noted again that the continuum solutions presented here have been calculated on a model modified to have a very small nose radius. This choice was made to avoid creating a grid-singularity boundary condition, and modeling the nose as sharp. The nose radius used was 0.0625 inches. Approaching the corner to the 55° rear cone, an increase in pressure and density is seen ahead of the corner.

The shock that develops in this region interacts with the boundary layer flow, separating the flow into a laminar separation region. Figure 23 depicts this region with a velocity vector presentation. The blue lines in this figure represent the bounds of subsonic flow within the solution. As with most shock/boundary layer interactions, a clearly defined shock is not present near the wall, as can be seen in Figure 25. This shock feature is considerably thicker than that seen upstream.

Between the shock layer edge and the separated region, the mass and momentum of the forward shock layer flows. The forecone shock smoothly merges into the "separation shock," which bounds this region. The separated region can be seen in Figure 23

Near the end of the separated region, the shock layer edge splits. One branch becomes a nearly normal shock, ahead of the rear cone, and the other connects to the reattachment of the separated region. Nompelis et al [62] call this the "transmitted" shock. The point of maximum pressure is just aft of this transmitted shock. Downstream of this point, the maximum pressure region produces a "sheet" of high velocity, described by Nompelis et al as a jet. This sheet of high speed flow is much closer to the wall than that found in the hollow cylinder flare interaction. The upper surface of this jet or sheet is a contact surface.

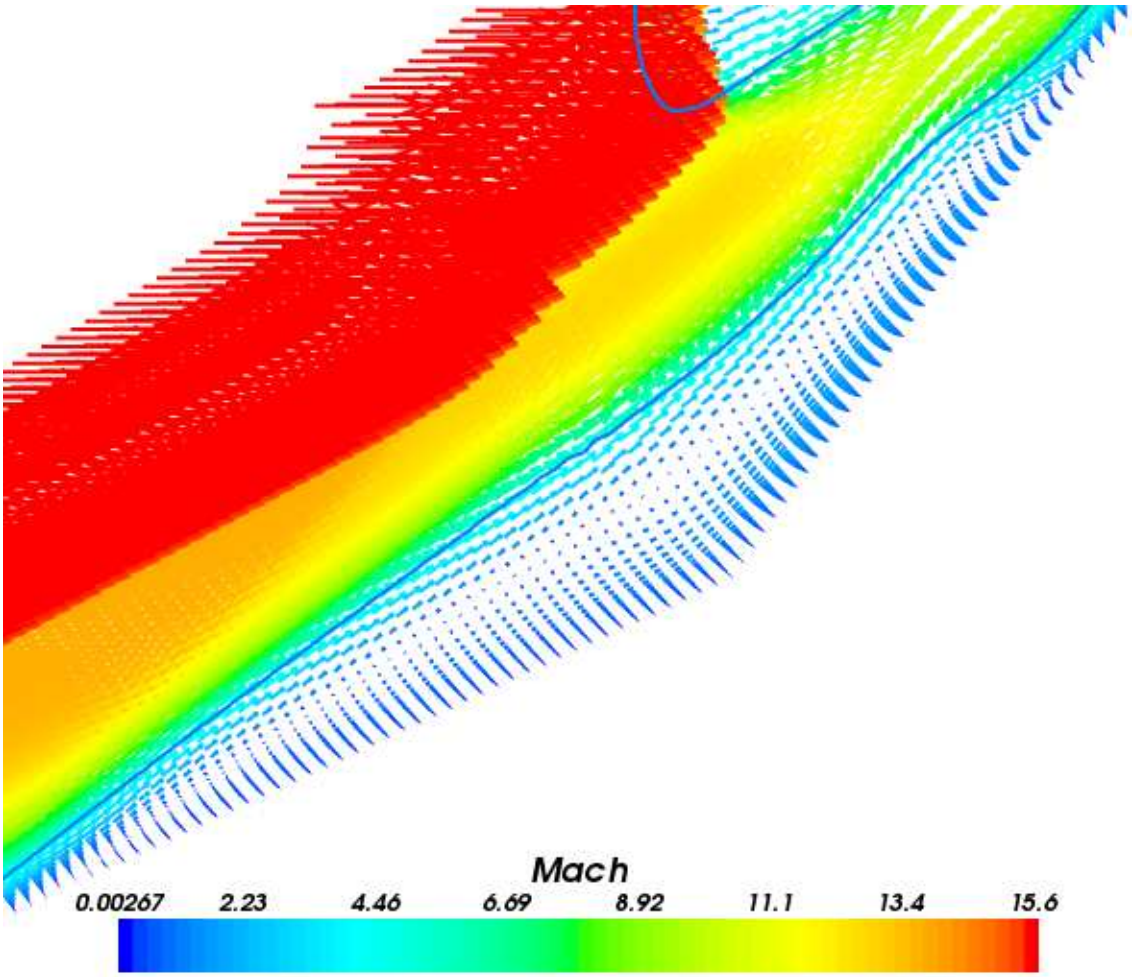

Figure 23: Double cone separation region detail

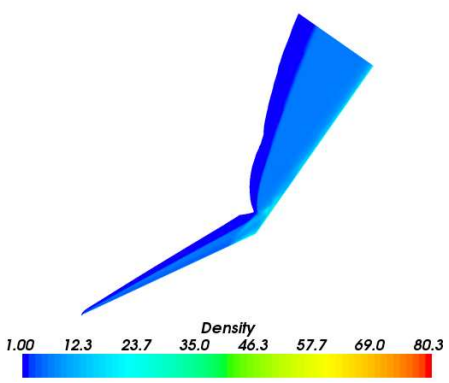

(a) $\mu_B = 0$

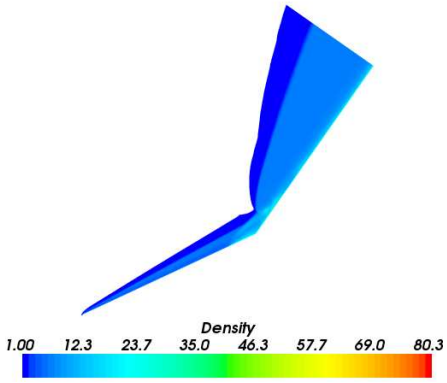

(b) $\mu_B = 0.8\mu$

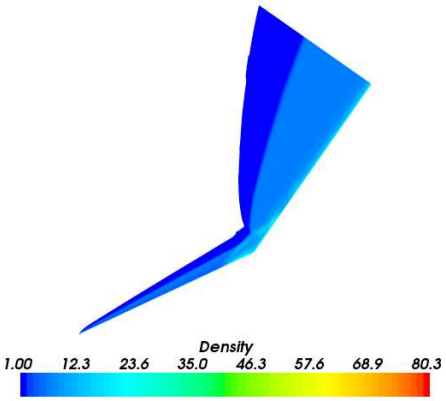

(c) μ_B from Cappelletti et al [36]

Figure 24: Double cone density

Figure 24 compares contours of density. The shock layer is progressively thicker on moving from the solution with no bulk viscosity, to the that of constant bulk viscosity and is thickest in the temperature-dependent model.

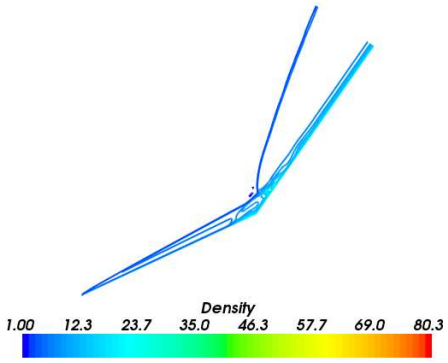

(a) $\mu_B = 0$

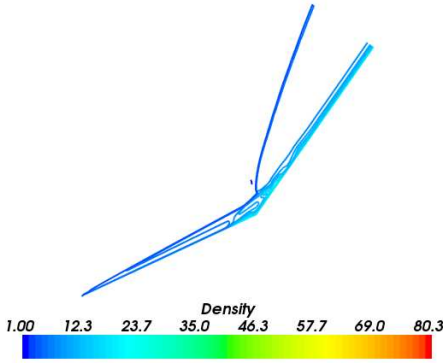

(b) $\mu_B = 0.8\mu$

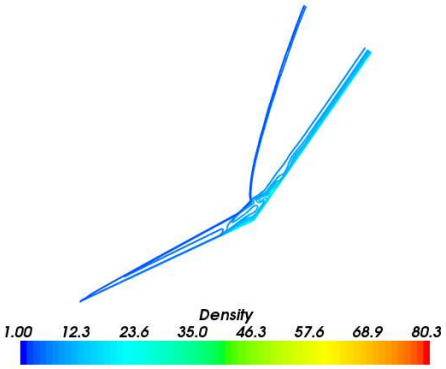

(c) μ_B from Cappelletti et al [36]

Figure 25: Double cone density contours

The shock thickness is most visible in Figure 25. The shock, and shock layer increases in thickness when moving from the zero velocity solution to that of the constant bulk viscosity, and finally to the temperature dependent bulk viscosity solution. The separation region forward of the corner can be seen in the density contour plot. The constant bulk viscosity solution predicts a larger separation region, extending slightly forward of that predicted by the zero bulk viscosity solution. The temperature dependent bulk viscosity solution extends even farther forward, and is larger.

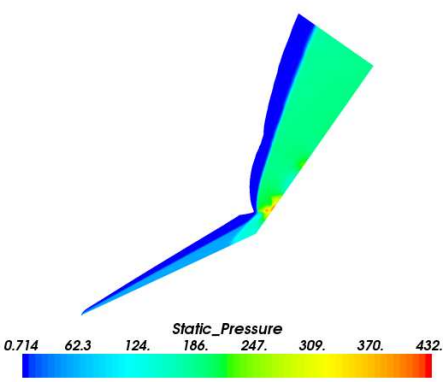

(a) $\mu_B = 0$

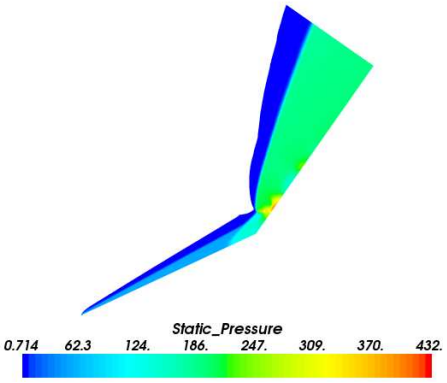

(b) $\mu_B = 0.8\mu$

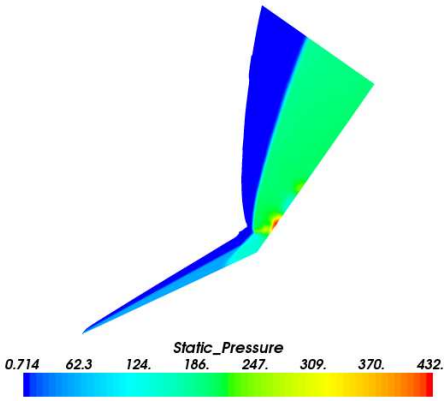

(c) μ_B from Cappelletti et al [36]

Figure 26: Double cone pressure

Figure 26 depicts the pressure field of the three CFD solutions. The separated flow region can be seen, as a region of increased pressure compared to the shock layer on the 25° forecone. The separated region is predicted to be larger in the constant bulk viscosity solution than in the zero bulk viscosity solution. The largest separation region can be seen in the temperature dependent bulk viscosity solution. The latter solution also predicts a higher maximum pressure, slightly aft of maximum pressure predicted by the zero and constant bulk viscosity solutions.

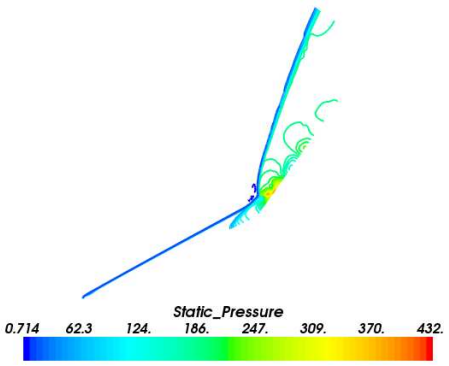

(a) $\mu_B = 0$

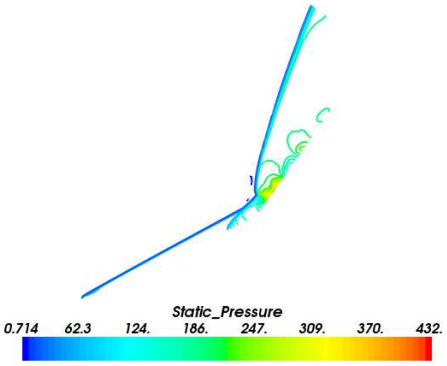

(b) $\mu_B = 0.8\mu$

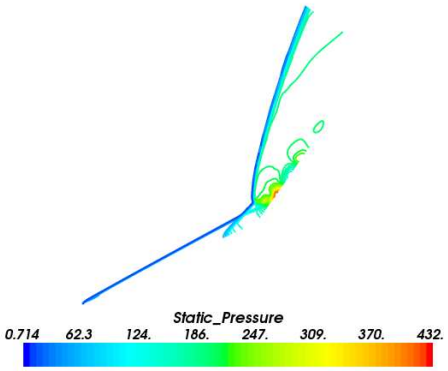

(c) μ_B from Cappelletti et al [36]

Figure 27: Double cone pressure contours

Figure 27 depicts pressure contours for the three CFD solutions. The shock layer thickness is greater in the temperature dependent bulk viscosity solution, than in the other two CFD solutions. The larger separated flow region near the corner can be seen in the nonzero bulk viscosity solutions, the largest seen in the case of the temperature dependent bulk viscosity. The highest peak pressure can also be seen clearly in Figure 27 (c).

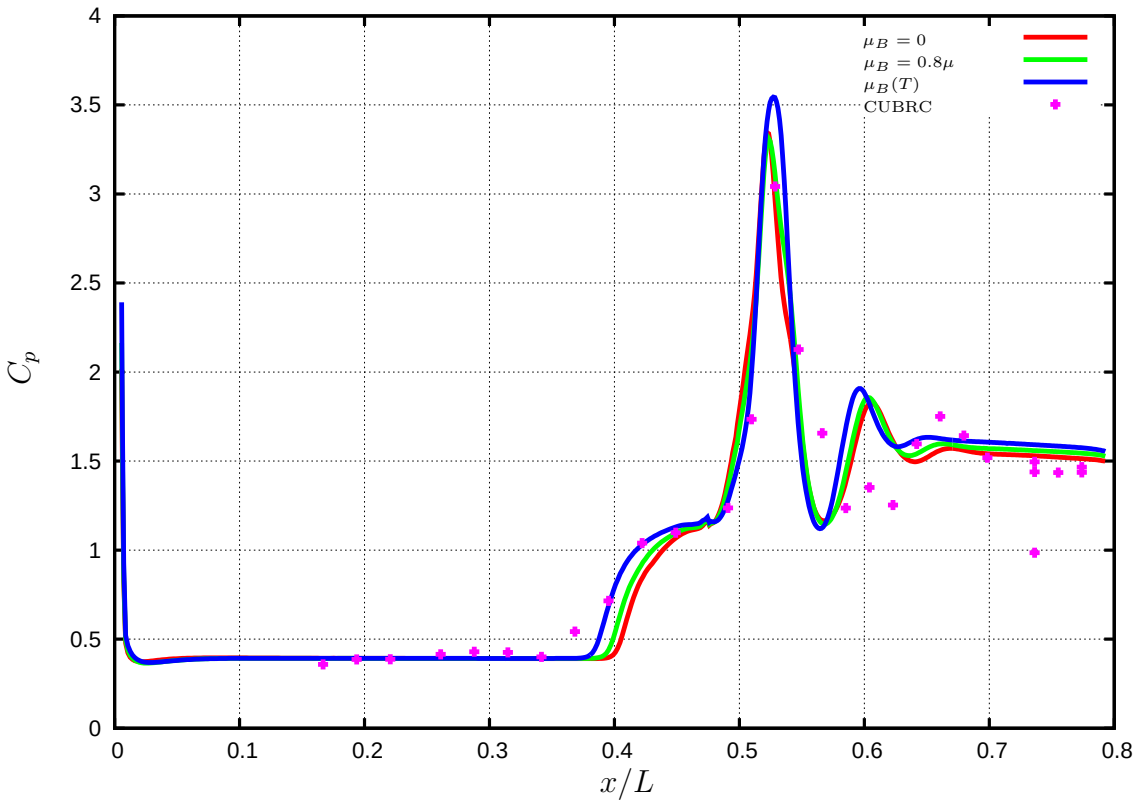

Figure 28: Double cone surface pressure coefficient

The pressure coefficient on the surface is depicted in Figure 28. Note, the separation region is slightly better predicted by the constant bulk viscosity model. The solution computed with temperature dependent bulk viscosity predicts slightly earlier separation, but still separates aft of the experimental measurements, as do the other CFD solutions, and the DSMC solutions of Carr [11:64]. The three pressures near and aft of $x/L = 0.4$ are predicted by the temperature dependent bulk viscosity in near perfect agreement with the observed pressures, as are the two pressures on the forward, rising pressure side of the impingement point near $x/L = 0.5$. Aft of the impingment point, the three CFD solutions exhibit more oscillation in pressure than that seen in the DSMC solutions. There appears to be some scatter in the experimental results in this region. The Stanton number is depicted in Figure 29. The three CFD solutions are depicted with dashed lines, to show that the associated predictions of heating are nearly identical. The heat transfer is underpredicted on

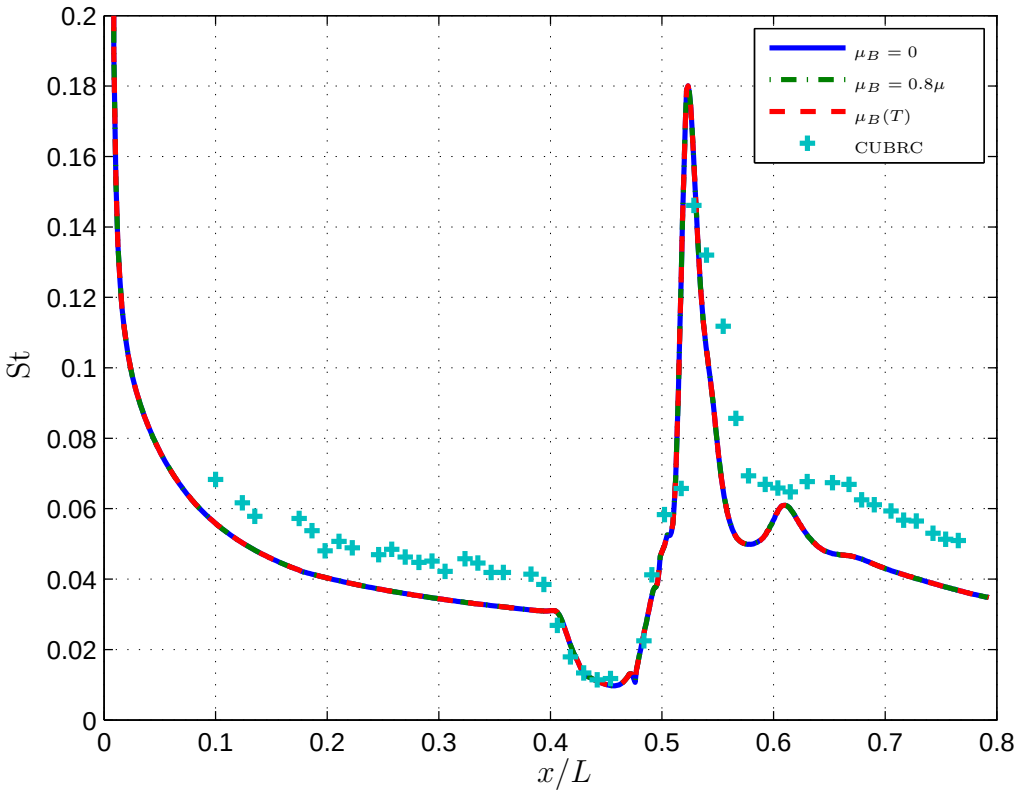

Figure 29: Double cone Stanton number

the forecone. The heat transfer predicted by CFD through the separation region, from $x/L = 0.4$ to $x/L = 0.5$ is in agreement with the observed heat transfer. The two heating predicitons just past $x/L = 0.5$ are in agreemement with the observed heat transfer. Unfortunately, no experimental point is located closer to the predicted maximum heat transfer. The heat transfer on the portion of the 55° cone aft of the impingement point is underpredicted by the three CFD solutions. Figure 30 depicts locations of pressure cuts taken to compare the CFD solutions to the DSMC solutions of Carr [11:64–65]. For the double cone case, solutions from both MONACO, which uses the Parker rotational relaxation model, and DS2V, Bird's solver (of [9]), using a constant rotational collision number, are available. Carr reports the latter solutions to be in closer agreement to experiment than the former [47]. Figures 31 through 36 contain selected pressure extractions at the locations depicted in Figure 30.

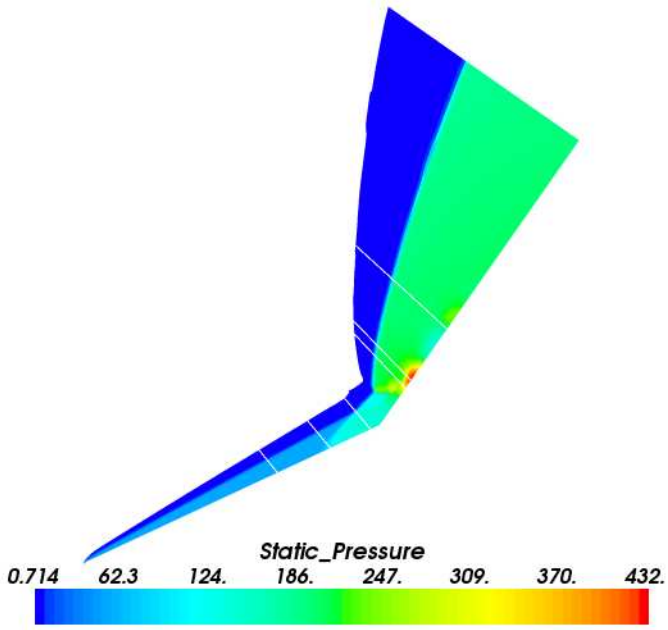

Figure 30: Double cone pressure comparison locations

Figure 31 depicts extractions of pressure data from the three CFD solutions, MONACO and DS2V DSMC codes. This extraction, as seen in Figure 30 is taken on the 25° forecone, ahead of the separation region. Both DSMC solvers predict a thicker shock layer, and thicker shock than that seen in the CFD solutions. The CFD solutions computed with constant and temperature dependent bulk viscosity predict a thicker shock than does the CFD solution computed with no bulk viscosity. Increased pressure at the wall is visible in the DS2V solution only. Note that the two DSMC solutions predict different pressure at this point.

Figure 31 depicts extractions of pressure data taken from near the forward end of the separation region. At this location, $x/L = 0.4$, the CFD solution computed-with temperature dependent bulk viscosity is the only solution which agrees with the observed pressure, as can be seen in Figure 28. The CFD solutions with bulk viscosity predict a thicker shock than does the CFD solution with no bulk viscosity. The pressure rise toward the surface is seen in the constant bulk viscosity CFD solution and the DS2V DSMC solution, to a lesser extent. Recall that the constant bulk viscosity

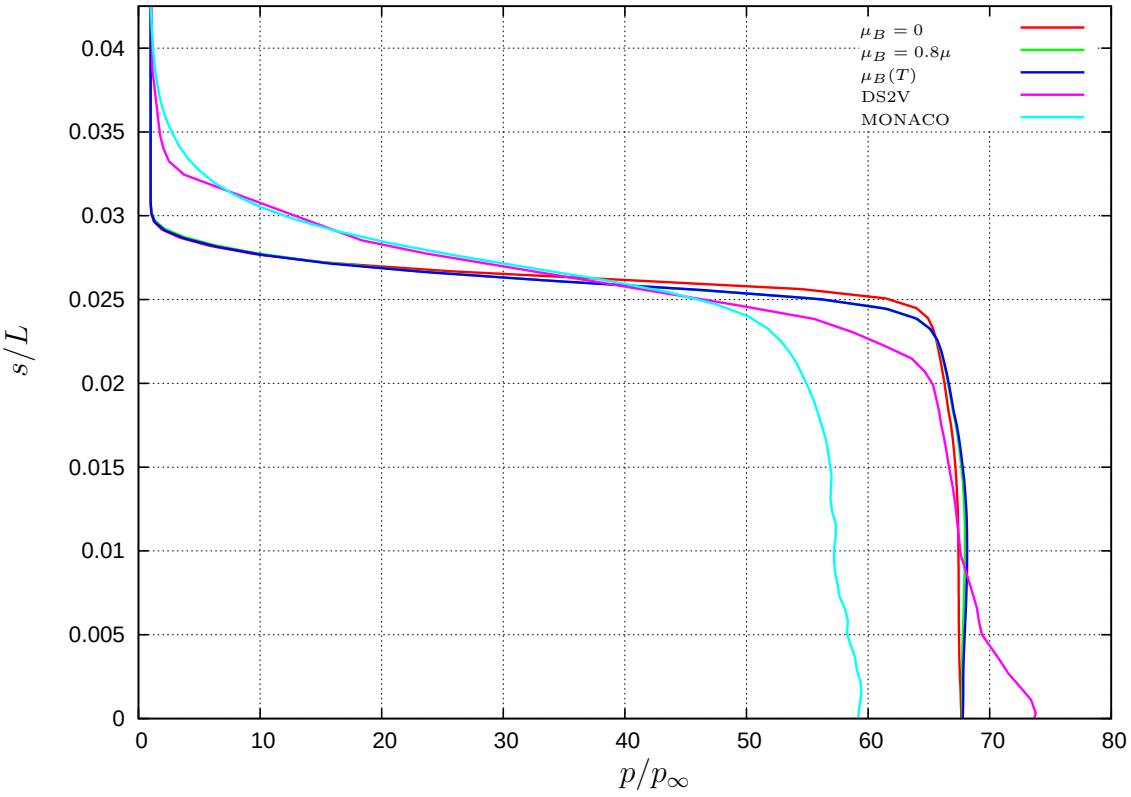

Figure 31: Extraction of pressure data, run 7, $x/L = 0.31$, $i = 169$

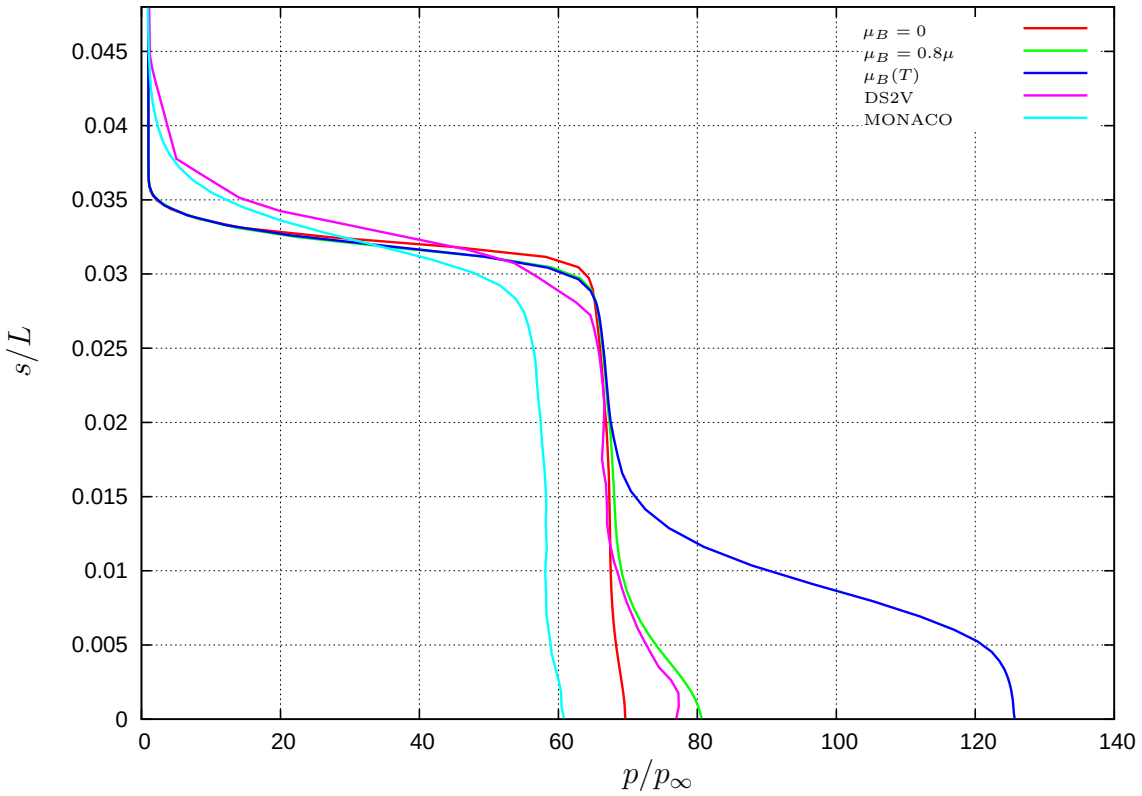

Figure 32: Extraction of pressure data, run 7, $x/L = 0.40$, $i = 215$

and a constant rotational collision number are similar phenomenological models for rotational relaxation, so some similarity is expected. The hot side of the shock is predicted to be thicker in DS2V than with the CFD solutions.

Figure 33 depicts pressure extractions taken at $x/L = 0.46$, within the separation region. As can be seen in Figure 28, the CFD solution computed with constant bulk viscosity nearly agrees with the observed surface pressure. The constant and temperature dependent bulk viscosity model and DS2V predict one shock, whereas the zero bulk viscosity CFD solution and MONACO solutions predict the forecone shockand separation shock as separate entities at this cut location.

Figure 34 depicts pressure extractions from $x/L = 0.52$, or the forward side of the shock impingement point. The CFD solution computed with temperature dependent bulk viscosity predicts the thickest shock layer, and thicker shocks than the other two CFD solutions. The thinnest shock layers are predicted by the two

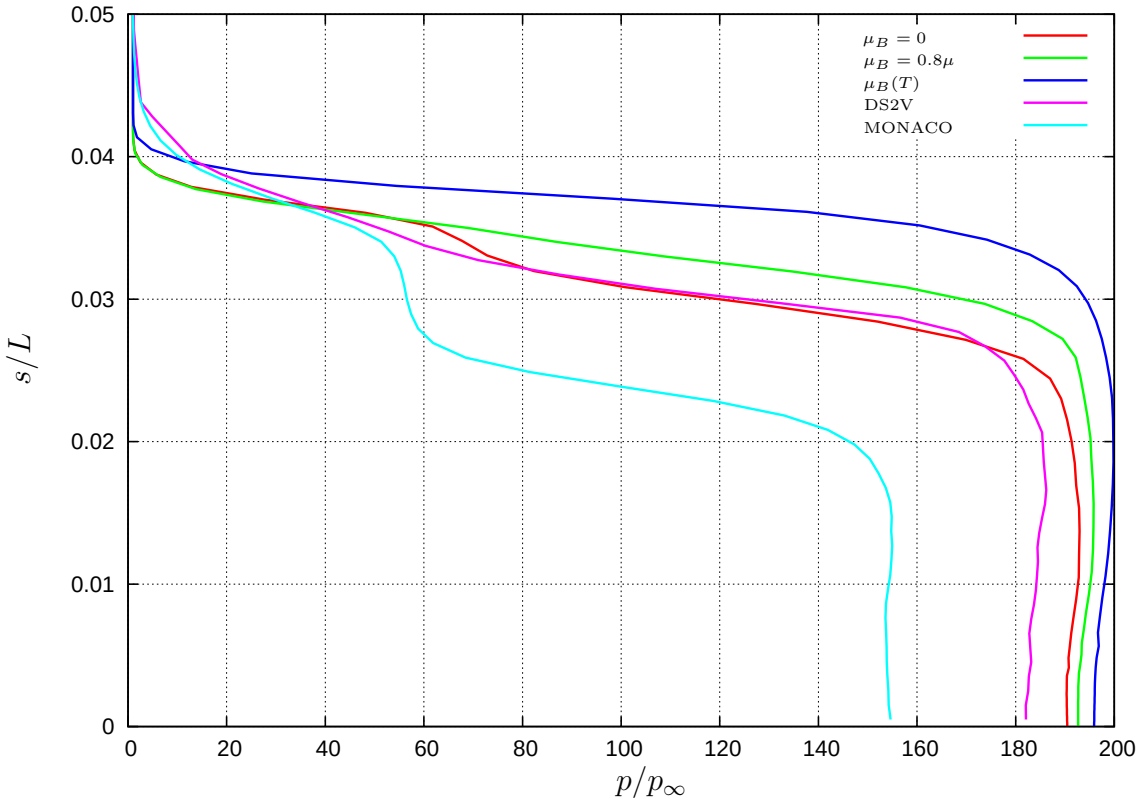

Figure 33: Extraction of pressure data, run 7, $x/L = 0.46$, $i = 250$

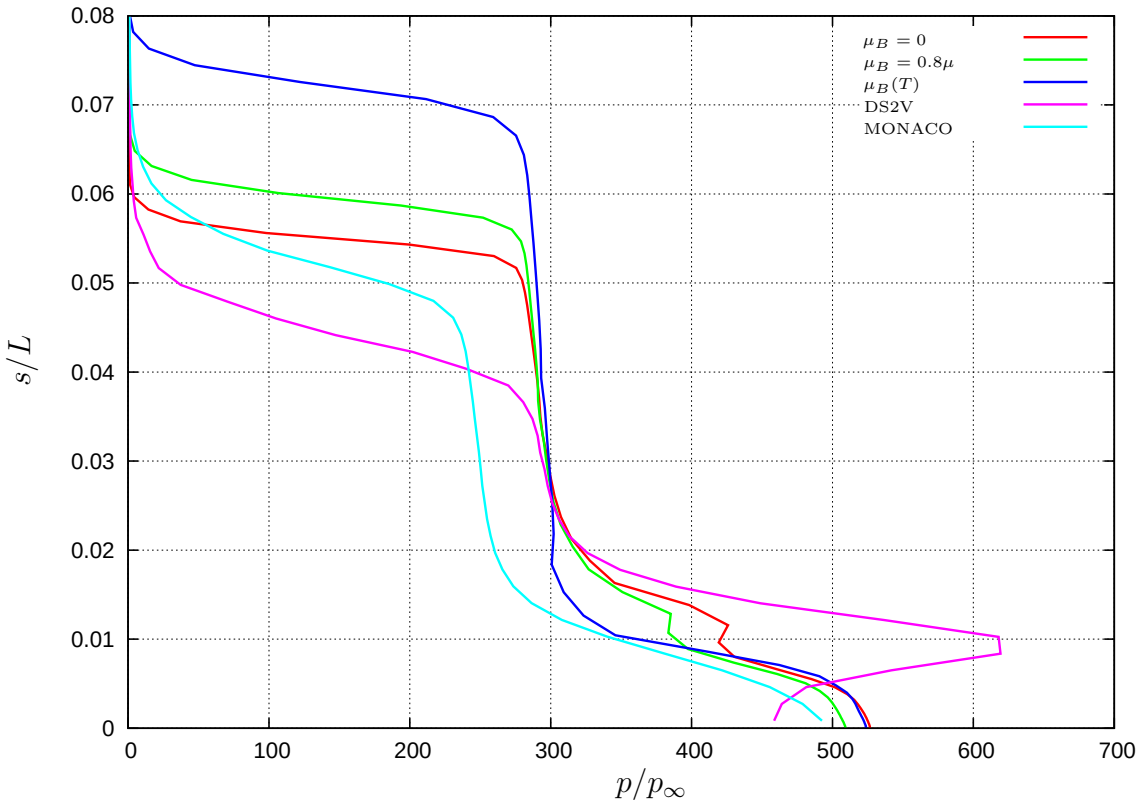

Figure 34: Extraction of pressure data, run 7, $x/L = 0.52$, $i = 292$

DSMC solutions. Note that DS2V predicts a pressure maximum above the surface at this location. A much smaller local pressure maximum at this point can be seen in the zero and constant bulk viscosity CFD solutions. There is some similarity of pressure profiles seen when comparing temperature depdendent bulk viscosity and MONACO, which uses a temperature dependent rotational collision number.

Figure 35 depicts pressure profiles slightly downstream, where the temperature dependent model overpredicts presssure, when compared to the observations of Holden and Wadhams [1]. Here this solution again predicts a thicker shock layer than do the other two CFD solutions. The zero bulk viscosity CFD solution nearly matches the shock location predicted by the MONACO solution, while DS2V predics a thinner shock layer. The DS2V and zero bulk viscosity CFD solutions predict a local pressure maximum at this cut location.

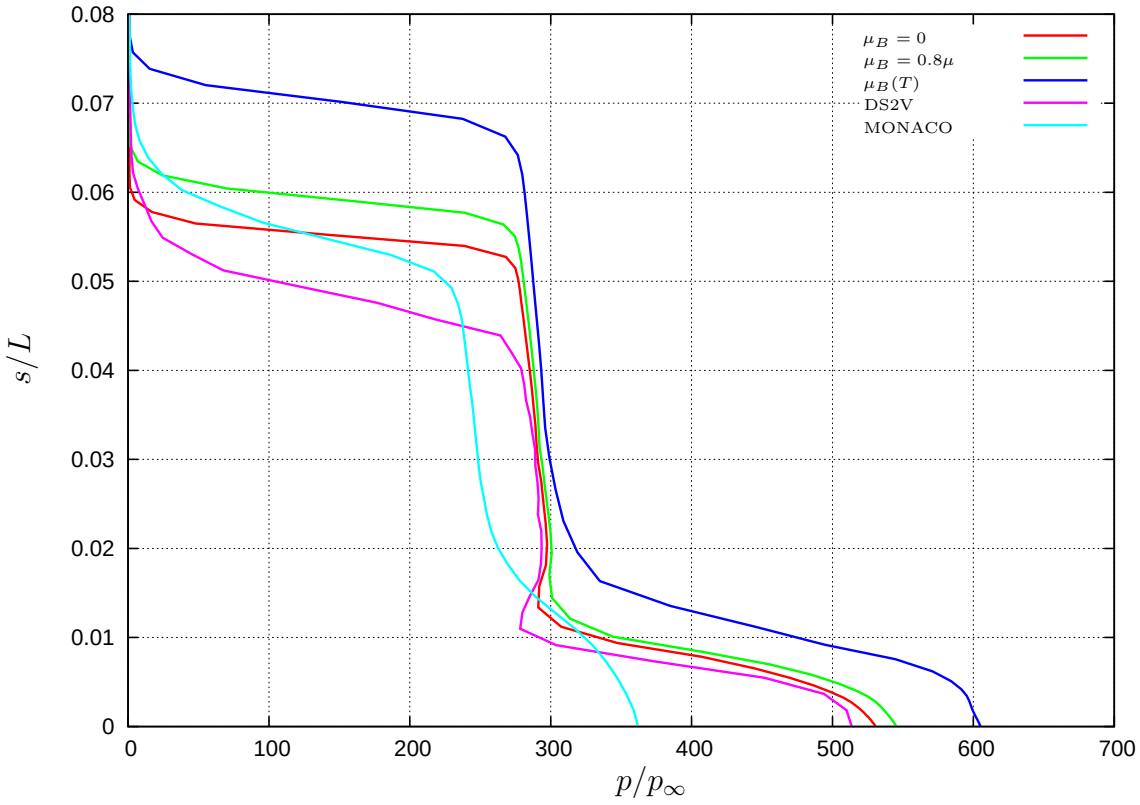

Figure 35: Extraction of pressure data, run 7, $x/L = 0.53$, $i = 299$

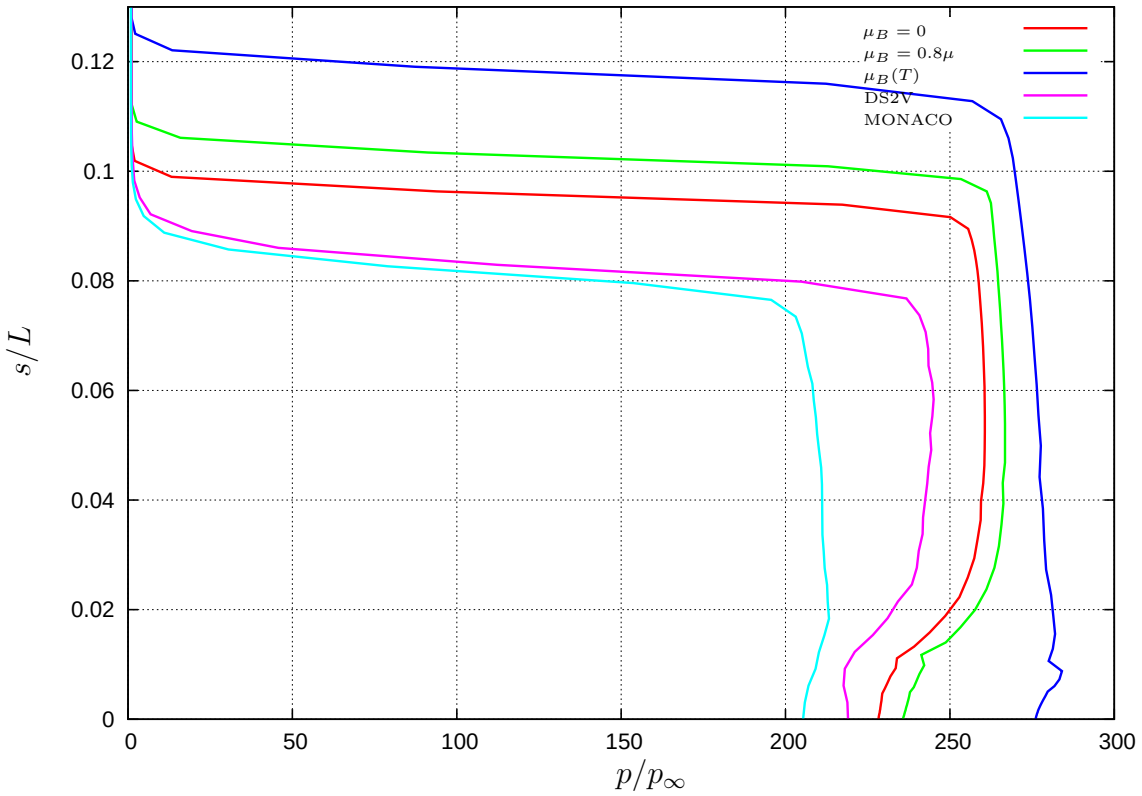

Figure 36: Extraction of pressure data, run 7, $x/L = 0.58$, $i = 344$

Figure 36 depicts the pressure profiles at $x/L = 0.58$, past the shock impingement point. The DSMC solutions predict the thinnest shock layer . The thickest shock and shock layer is predicted by the temperature dependent bulk viscosity model. A thinner shock layer is predicted by the constant bulk viscosity model, and the thinnest of the three CFD solutions was computed with zero bulk viscosity. The zero and constant bulk viscosity CFD solutions exhibit some similarities to the DS2V DSMC solution.

V. Conclusions

In studying high speed and high altitude flows, a means for accounting for non-equilibrium effects, such as the equilibration process between internal and translational modes of energy is desired. The geometry of the flow features in non-equilibrium situations is affected by this equilibration process. The shock layer thickness in high speed flight is affected by this process. Location of shock/boundary layer interaction points is also affected by this process.

The bulk viscosity, incorporated into CFD models, to some extent, accounts for the effect of the finite time of the rotation-translation energy transfer on the flow. There is a limit to how far from equilibrium bulk viscosity can be used to model this process.

The bulk viscosity has been shown here to improve, in some circumstances, the shock thickness and prediction of heat transfer on the body. Of the two-dimensional cases studied, the surface heat transfer distribution of the hollow cylinder flare shows improvement on including the bulk viscosity model from Cappelletti et al. The double cone case shows some improvement in the prediction of the onset of flow separation at the corner between front and rear cones.

The peak pressure tends to be slightly over-predicted when including bulk viscosity. The behavior in the post-shock-impingement region of the double cone case appears to be oscillatory, and this behavior is not in agreement with the experimental data. The pressure on the cylinder flare case aft of the impingement region "undershoots" the measured values, and thereafter remains lower. These two examples suggest that the bulk viscosity model is more suited to compressions, and behaves differently in expansion than compression. This result is not too surprising, given the disagreements in the literature over which rotational relaxation models are appropriate for a particular situation. The temperature dependent models here presented use "sudden" approximations, which assume a collision duration shorter than the rotational period of the molecule. Brau and Jonkman [30] and Wysong and Wadsworth [49] point out that if the opposite is assumed, the gas does not behave

as with a "single relaxation time." McCourt et al [2:496] describe the difficulties in measuring rotational relaxation with ultrasonic means, and the difficulty, at least in 1990, of determining the rotational temperature using light scattering methods, such as depolarized Rayleigh scattering. Successful determination of the behavior of rotational energy transfer of H_2 has been performed with light scattering, but it is reported that the greater number of rotational states and their tighter distribution for heavier molecules such as N_2 has made measurements more difficult. It is hoped that these methods will continue to improve, and be able to provide more information about rotational relaxation.

It has been remarked that the bulk viscosity is appropriate for "small" deviations from equilibrium [63]. In the axisymmetric solutions presented in this work, that assessment is supported. The weaker-shock run 5, the hollow cylinder flare, shows an improvement in agreement with observations when calculated with the bulk viscosity. The stronger-shock run 7, the double cone, shows less improvement. The Jeans or Jeans-Landau-Teller model is reported to be more appropriate for larger deviations from equilibrium [44].

The inclusion of the internal energy modes relaxation in determining the heat conduction would be a natural next step for future work. The shear viscosity and heat transfer cross sections are also calculated in the work of Cappelletti et al [36]. The effect of including this enhanced heat transfer treatment, and shear viscosity is expected to be small in the case of the conditions and geometries studied in this work.

In the work of Heck and Dickinson [24], on which the work of Cappelletti et al [36], it is mentioned that the transport coefficients, such as shear viscosity, bulk viscosity, and heat conduction were originally meant for a second order Chapman-Enskog expansion of a generalized Boltzmann Equation, known as the Curtiss-Kagan-Maksimov equation. Future work in this area should discover the form of these second order hydrodynamic equations, and determine how these equations behave, and if they share the same problems reported for their second-order hydrodynamics counterpart, the Burnett equations, obtained from a similar expansion process on the Boltzmann equation.

```
! Added 7 Oct 07 Capt Abram Claycomb

!******************************  ALIGN_SHOCK  ******************************!
! Aligns Grid to and clusters points around shock, keeping adequate boundary
! layer resolution.  Taken from Gnoffo, Hartung and Greendyke(AIAA-93-270-864)
!***************************************************************************!

subroutine align_shock()

  use runtime_module
  implicit none

  integer :: i, j, jt                          ! Index counters
  integer :: j_star, j_max                     ! j-location of end of b.l. cells
  integer :: ncells_i, nfaces_i
  integer :: ncells_j, nfaces_j
  integer :: cell_imin, cell_imax
  integer :: cell_jmin, cell_jmax

  ! node locations
  real(kind=RKIND), dimension(:,:), pointer :: x, y
  ! new face locations
  real(kind=RKIND), dimension(:,:), allocatable :: xfnew, yfnew
  ! cell centers
  real(kind=RKIND), dimension(:,:), allocatable :: xf_c, yf_c !, x_c, y_c
  ! change in x, y from face to face in j direction
  real(kind=RKIND), dimension(:,:), allocatable :: dnx, dny
  ! change in, 'curvilinear' normal distance in j away from wall
```

```
real(kind=RKIND), dimension(:,:), allocatable :: dnf, nold, noldf
real(kind=RKIND), dimension(:,:), allocatable :: dnhat, nhat, nnew, nnewf

! running total of distance to last cell center, outer face of grid
real(kind=RKIND), dimension(:), allocatable :: nlastcell, nlastface

! shock location array
real(kind=RKIND), dimension(:), allocatable :: nshk

! constants for the code
real(kind=RKIND) :: pi, dpi

! shock, b.l. fitting parameters
real(kind=RKIND) :: C1, C2, C2_max, hmin1, hmin2, rhowall, asnd, ep
real(kind=RKIND) :: nxyfactor

! grid metric computation... and j max node computation...
real(kind=RKIND) :: dx1, dy1, dx2, dy2, na

pi = acos(-ONE)

ncells_i = num_i_cells(grid)       ! internal cells only
nfaces_i = num_i_faces(grid)       ! faces  = # cells + n_ghost
cell_imin = CELL_MIN_INDEX         ! includes ghost cells (0 or 1 - nghost)
cell_imax = cell_max_i_index(grid) ! includes ghost cells (ncells_i + nghost)

ncells_j = num_j_cells(grid)
nfaces_j = num_j_faces(grid)
cell_jmin = CELL_MIN_INDEX
```

```
  cell_jmax = cell_max_j_index(grid)

  allocate( xf_c(1:ncells_i,1:nfaces_j) )
  allocate( yf_c(1:ncells_i,1:nfaces_j) )
  allocate( xfnew(1:ncells_i,1:nfaces_j) )
  allocate( yfnew(1:ncells_i,1:nfaces_j) )
!  allocate( x_c(1:ncells_i,1:ncells_j) )
!  allocate( y_c(1:ncells_i,1:ncells_j) )
  allocate( dnx(1:ncells_i,1:ncells_j) )
  allocate( dny(1:ncells_i,1:ncells_j) )
  allocate( dnf(1:ncells_i,1:ncells_j) )
  allocate( nold(1:ncells_i,1:ncells_j) )  ! dist from wall to this cell center
  allocate( noldf(1:ncells_i,1:nfaces_j) ) ! ...                    face
  allocate( dnhat(1:ncells_i,1:ncells_j) )
  allocate( nhat(1:ncells_i,1:nfaces_j) )
  allocate( nnew(1:ncells_i,1:ncells_j) )
  allocate( nnewf(1:ncells_i,1:nfaces_j) )
  allocate( nlastcell(1:ncells_i) )
  allocate( nlastface(1:ncells_i) )
  allocate( nshk(1:ncells_i) )

  x => grid%x
  y => grid%y

  ! get face center position of j-normal faces...
  xf_c = HALF*( x(2:nfaces_i,1:nfaces_j) + x(1:ncells_i,1:nfaces_j) )
  yf_c = HALF*( y(2:nfaces_i,1:nfaces_j) + y(1:ncells_i,1:nfaces_j) )

  ! get cell centers...
```

```
!  x_c = HALF*( xf_c(1:ncells_i,2:nfaces_j) + xf_c(1:ncells_i,1:ncells_j) )
!  y_c = HALF*( yf_c(1:ncells_i,2:nfaces_j) + yf_c(1:ncells_i,1:ncells_j) )

  ! get distance between j-face centers...
  dnx = xf_c(1:ncells_i,2:nfaces_j) - xf_c(1:ncells_i,1:ncells_j)
  dny = yf_c(1:ncells_i,2:nfaces_j) - yf_c(1:ncells_i,1:ncells_j)

  dnf = sqrt(dnx**2 + dny**2)

  nlastcell(:) = HALF*dnf(:,1)
  nlastface(:) = dnf(:,1)
  noldf(:,1) = ZERO

  nold(:,1) = nlastcell(:)
  noldf(:,2) = nlastface(:)

  ! get cumulative old curvilinear distance...
  do j = 2, ncells_j
     !jt = min(j-1,1)
     !nold(:,j) = HALF*(dnf(:,jt)+dnf(:,j)) + nlastcell(:)
     nold(:,j) = HALF*dnf(:,j) + nlastface(:)
     nlastcell(:) = nold(:,j)

     noldf(:,j+1) = dnf(:,j) + nlastface(:)
     nlastface(:) = noldf(:,j+1)

  end do

!!$  open(unit=101, file='ntest.dat', status = 'replace')
```

```
!!$
!!$  do j = 1, ncells_j
!!$     write(101, *) 'noldf(1,',j+1,') = ', noldf(1, j+1)
!!$     write(101, *) 'nold(1,',j,') = ', nold(1,j), ',rho = ', grid%Q(R_,1,j)
!!$  end do
!!$  !write(*, '(A)') 'outer face distance test complete'

  ! density hard-coded, could easily add runtime_module variable for this,
  ! initial_module input line for input file of which var. to sense...
  call shock_loc(nold, nshk, R_) ! locate s value of shock throughout grid...

  !do i = 1, ncells_i
  !   write(*, '(A, I, A, F8.3)') 'i ', i, ' nshk = ', nshk(i)
  !end do

  !write(*, '(A)') 'Shock Location Test Completed'

  j_star = f_star * ncells_j

  dpi = pi / j_star

  nhat(:,1) = ZERO  ! nondimensional distance of wall face from wall
  nnewf(:,1) = ZERO ! dimensional distance of wall face from wall (itself...)

  do i = ncells_i, 1, -1


     rhowall = grid%Q(R_,i,1)
```

```
asnd = sqrt(GAMMA*grid%Q(P_,i,1)/grid%Q(R_,i,1))

hmin1 = Re_cellw * grid%mu(i,1) / (rhowall * asnd * noldf(i,nfaces_j) )

!write(*,*) i, Re_cellw, grid%mu(i,1), hmin1

hmin2 = ONE / nfaces_j

hmin1 = min(hmin1, hmin2)

dnhat(i,1) = hmin1

nhat(i,2) = dnhat(i,1)

C1 = ( f_star / dnhat(i,1) ) ** ( ONE / j_star ) - ONE

!write(*,*) i, C1

C2 = max( ONE, (ONE + C1*sin(dpi)) )

C2_max = C2

!dnhat(i,2) = (ONE + C2)*dnhat(i,1)
dnhat(i,2) = C2*dnhat(i,1)

nhat(i,3) = dnhat(i,2) + nhat(i,2)

j_max = 3
```

```
do j = 4, nfaces_j


   C2 = max( ONE, (ONE + C1*sin((j - 2) * dpi)) )

   !write(*,*) i, j, C2

   dnhat(i,j-1) = min( (C2*(nhat(i,j-1) - nhat(i,j-2))), &
                       ((ONE - nhat(i,j-1))/(nfaces_j - j + 1)) )

   !write(*,*) i, j-1, dnhat(i,j-1)

   nhat(i,j) = dnhat(i,j-1) + nhat(i,j-1)

   !write(*,*) i, j, nhat(i,j)

   if ( C2 > C2_max ) then

      C2_max = C2
      j_max = j

   end if


end do


if ( nhat(i,nfaces_j) /= ONE ) then
```

```
         nhat(i,2:nfaces_j) = nhat(i,2:nfaces_j) / nhat(i,nfaces_j)

      end if


      if ( ep0 /= 0 ) then


         do j = 2, nfaces_j

            ep = nhat(i,j)**2 * ( 1 - nhat(i,j) ) * ep0

            nhat(i,j) = ( ONE - ep ) * nhat(i,j) + fsh * ep

            !write(*,*) 'i','j','ep','nhat'
            !write(*,*) i, j, ep, nhat(i,j)

         end do


      end if


      nxyfactor = noldf(i,nfaces_j) * nshk(i)
      !nxyfactor = nshk(i)
      !nxyfactor = min( nxyfactor, C2_max )

!!$     write(101, *) 'nxyfactor(i=1) = ', nxyfactor
```

```
do j = 2, nfaces_j

   nnewf(i,j) = nhat(i,j) * nxyfactor

   nnew(i,j-1) = HALF*(nnewf(i,j) + nnewf(i,j-1))

end do

! for inflow boundary meeting directly with body, keeps grid from
! collapsing
if ((algn_exclude /= 0) .and. (i < algn_exclude)) then

   nnewf(i,:) = nnewf(i+1,:)
   nnew(i,:) = nnew(i+1,:)

end if

! interpolate solution into new cell center positions
call interpextr(nold(i,1:ncells_j),grid%Q(R_,i,1:ncells_j),nnew(i,1:ncells_j),xf
                1,ncells_j,1,ncells_j)
grid%Q(R_,i,1:ncells_j) = xfnew(i,1:ncells_j)

call interpextr(nold(i,1:ncells_j),grid%Q(RU_,i,1:ncells_j),nnew(i,1:ncells_j),x
                1,ncells_j,1,ncells_j)
grid%Q(RU_,i,1:ncells_j) = xfnew(i,1:ncells_j)
call interpextr(nold(i,1:ncells_j),grid%Q(RV_,i,1:ncells_j),nnew(i,1:ncells_j),x
                1,ncells_j,1,ncells_j)
grid%Q(RV_,i,1:ncells_j) = xfnew(i,1:ncells_j)
```

```
      call interpextr(nold(i,1:ncells_j),grid%Q(E_,i,1:ncells_j),nnew(i,1:ncells_j),xf
                      1,ncells_j,1,ncells_j)
      grid%Q(E_,i,1:ncells_j) = xfnew(i,1:ncells_j)
      call interpextr(nold(i,1:ncells_j),grid%Q(P_,i,1:ncells_j),nnew(i,1:ncells_j),xf
                      1,ncells_j,1,ncells_j)
      grid%Q(P_,i,1:ncells_j) = xfnew(i,1:ncells_j)
      call interpextr(nold(i,1:ncells_j),grid%mu(i,1:ncells_j),nnew(i,1:ncells_j),xfne
                      1,ncells_j,1,ncells_j)
      grid%mu(i,1:ncells_j) = xfnew(i,1:ncells_j)
      call interpextr(nold(i,1:ncells_j),grid%lambda(i,1:ncells_j),nnew(i,1:ncells_j),
                      1,ncells_j,1,ncells_j)
      grid%lambda(i,1:ncells_j) = xfnew(i,1:ncells_j)

!!$     grid%Q(R_,CELL_MIN_INDEX:(ncells_j+1),CELL_MIN_INDEX:(ncells_j+1)) &
!!$           = q_freestream(R_)
!!$     grid%Q(RU_,CELL_MIN_INDEX:(ncells_j+1),CELL_MIN_INDEX:(ncells_j+1)) &
!!$           = q_freestream(RU_)
!!$     grid%Q(RV_,CELL_MIN_INDEX:(ncells_j+1),CELL_MIN_INDEX:(ncells_j+1)) &
!!$           = q_freestream(RV_)
!!$     grid%Q(E_,CELL_MIN_INDEX:(ncells_j+1),CELL_MIN_INDEX:(ncells_j+1)) &
!!$           = q_freestream(E_)
!!$     grid%Q(P_,CELL_MIN_INDEX:(ncells_j+1),CELL_MIN_INDEX:(ncells_j+1)) &
!!$           = q_freestream(P_)

      ! interpolate face center positions...
      call interpextr(noldf(i,:),xf_c(i,:),nnewf(i,:),xfnew(i,:), &
                      1,nfaces_j,1,nfaces_j)
      call interpextr(noldf(i,:),yf_c(i,:),nnewf(i,:),yfnew(i,:), &
                      1,nfaces_j,1,nfaces_j)
```

```
end do

if(vec_preserve .eq. 1) then

   do i = 1, ncells_i

      ! Keep all points on same vector as original grid
      dx1 = -grid%A_i(Y_,i,1)
      dy1 = grid%A_i(X_,i,1)
      dx2 = xfnew(i,2) - xfnew(i,1)
      dy2 = yfnew(i,2) - yfnew(i,1)

      na = (dx1*dx2 + dy1*dy2)/((dx1*dx1 + dy1*dy1)*sqrt(dx2*dx2 + dy2*dy2))

      !write(*,*)'dx1', dx1, 'dx2', dx2, 'dy1', dy1, 'dy2', dy2, 'na', na

      grid%x(i,2:nfaces_j) = na*nnewf(i,2:nfaces_j)*dx1 &
           + grid%x(i,1)
      grid%y(i,2:nfaces_j) = na*nnewf(i,2:nfaces_j)*dy1 &
           + grid%y(i,1)


   end do

   ! Keep jmax points on same vector as original grid
   dx1 = -grid%A_i(Y_,nfaces_i,1)
   dy1 = grid%A_i(X_,nfaces_i,1)
   dx2 = xfnew(ncells_i,2) - xfnew(ncells_i,1)
```

```
   dy2 = yfnew(ncells_i,2) - yfnew(ncells_i,1)

   na = (dx1*dx2 + dy1*dy2)/((dx1*dx1 + dy1*dy1)*sqrt(dx2*dx2 + dy2*dy2))

   !write(*,*)'dx1', dx1, 'dx2', dx2, 'dy1', dy1, 'dy2', dy2, 'na', na

   grid%x(nfaces_i,2:nfaces_j) = na*nnewf(ncells_i,2:nfaces_j)*dx1 &
        + grid%x(nfaces_i,1)
   grid%y(nfaces_i,2:nfaces_j) = na*nnewf(ncells_i,2:nfaces_j)*dy1 &
        + grid%y(nfaces_i,1)


else

   ! interpolate interior grid points, jmax ...  from new face centers

   grid%x(2:(nfaces_i-1),2:nfaces_j) &
        = HALF*(xfnew(1:ncells_i,2:nfaces_j) + xfnew(2:nfaces_i,2:nfaces_j))
   grid%y(2:(nfaces_i-1),2:nfaces_j) &
        = HALF*(yfnew(1:ncells_i,2:nfaces_j) + yfnew(2:nfaces_i,2:nfaces_j))

   ! extrapolate x coordinates of imin surface, y coordinates of imax surface
   ! (hardcoding for axisymmetric, positive x direction flow, orthogonal
   !  outflow face...)
   !  grid%x(1,2:nfaces_j) = TWO*xfnew(1,2:nfaces_j) - grid%x(2,2:nfaces_j)
   !  grid%y(nfaces_i,2:nfaces_j) = TWO*yfnew(ncells_i,2:nfaces_j) &
   !                              - grid%y(ncells_i,2:nfaces_j)

   ! Keep imax points same as adjacent to keep normal to flow...
```

```
      grid%x(1,2:nfaces_j) = grid%x(2,2:nfaces_j)

      ! Keep jmax points on same vector as original grid
      dx1 = -grid%A_i(Y_,nfaces_i,1)
      dy1 = grid%A_i(X_,nfaces_i,1)
      dx2 = xfnew(ncells_i,2) - xfnew(ncells_i,1)
      dy2 = yfnew(ncells_i,2) - yfnew(ncells_i,1)

      na = (dx1*dx2 + dy1*dy2)/((dx1*dx1 + dy1*dy1)*sqrt(dx2*dx2 + dy2*dy2))

      !write(*,*)'dx1', dx1, 'dx2', dx2, 'dy1', dy1, 'dy2', dy2, 'na', na

      grid%x(nfaces_i,2:nfaces_j) = na*nnewf(ncells_i,2:nfaces_j)*dx1 &
           + grid%x(nfaces_i,1)
      grid%y(nfaces_i,2:nfaces_j) = na*nnewf(ncells_i,2:nfaces_j)*dy1 &
           + grid%y(nfaces_i,1)

   end if

! Compute the grid metrics

   do j = 1, ncells_j
      do i = 1, nfaces_i
         grid%A_i(X_,i,j) = grid%y(i,j+1) - grid%y(i,j)
         grid%A_i(Y_,i,j) = -(grid%x(i,j+1) - grid%x(i,j))
         grid%A_i(AMAG_,i,j) = sqrt(sum(grid%A_i(1:DOMAIN_DIM,i,j)**2))
      end do
   end do
```

```
  do i = 1, ncells_i
     do j = 1, nfaces_j
        grid%A_j(X_,i,j) = grid%y(i,j) - grid%y(i+1,j)
        grid%A_j(Y_,i,j) = -(grid%x(i,j) - grid%x(i+1,j))
        grid%A_j(AMAG_,i,j) = sqrt(sum(grid%A_j(1:DOMAIN_DIM,i,j)**2))
     end do
  end do

  do j = 1, ncells_j
     do i = 1, ncells_i
        dx1 = grid%x(i+1,j+1) - grid%x(i,j)
        dy1 = grid%y(i+1,j+1) - grid%y(i,j)
        dx2 = grid%x(i,j+1) - grid%x(i+1,j)
        dy2 = grid%y(i,j+1) - grid%y(i+1,j)
        grid%vol(i,j) = HALF*(dx1*dy2 - dx2*dy1)
     end do
  end do

  if( Reynolds_num /= ZERO ) then
     call calc_viscous_metrics()
  end if

!!$  write(101, *) 'nshk(1) = ', nshk(1)
!!$
!!$  do j = 1, ncells_j
!!$     write(101, *) 'nnewf(1,',j+1,') = ', nnewf(1, j+1)
!!$     write(101, *) 'nnew(1,',j, ') = ', nnew(1,j), ',rho = ', grid%Q(R_,1,j)
!!$  end do
```

```
  !write(*,*) 'Old curvilinear distance from wall of face centers'
  !write(*,*) noldf(:,:)
  !write(*,*) 'nhat -- nondimensional new curvilinear distance'
  !write(*,*) nhat(:,:)
  !write(*,*) 'New curvilinear distance from wall of face centers'
  !write(*,*) nnewf(:,:)

!!$  write(*,*) 'Old Face Center X-Coordinate'
!!$  write(*,*) xf_c(:,:)
!!$  write(*,*) 'Old Face Center Y-Coordinate'
!!$  write(*,*) yf_c(:,:)
!!$  write(*,*) 'New Face Center X-Coordinate'
!!$  write(*,*) xfnew(:,:)
!!$  write(*,*) 'New Face Center Y-Coordinate'
!!$  write(*,*) yfnew(:,:)

!!$  close(101)

  deallocate( xf_c )
  deallocate( yf_c )
  deallocate( xfnew )
  deallocate( yfnew )
  !  deallocate( x_c )
  !  deallocate( y_c )
  deallocate( dnx )
  deallocate( dny )
  deallocate( dnf )
  deallocate( nold )
```

```
  deallocate( noldf )
  deallocate( dnhat )
  deallocate( nhat )
  deallocate( nnew )
  deallocate( nnewf )
  deallocate( nlastcell )
  deallocate( nlastface )
  deallocate( nshk )

end subroutine align_shock
```

A.1 Shock Location Subroutine

```
!*******************************  SHOCK_LOC  *******************************!
! Aligns Grid to and clusters points around shock, keeping adequate boundary
! layer resolution.  Taken from Gnoffo, Hartung and Greendyke(AIAA-93-270-864)
!*************************************************************************!

subroutine shock_loc(s, sshk, comp)

  use runtime_module
  use constant_module
  use ErrorOut_module
  implicit none

  integer :: i, j                    ! counters
  integer :: ncells_i, nfaces_i
  integer :: ncells_j, nfaces_j
  integer :: cell_imin, cell_imax
  integer :: cell_jmin, cell_jmax
```

```
integer, intent(in) :: comp        ! component of solution vector to sense
                                   ! shock

real(kind=RKIND), dimension(:,:), intent(in) :: s ! cell curvil. dist. array
real(kind=RKIND), dimension(:), intent(out) :: sshk ! shock location array

real(kind=RKIND) :: atest, dtest, propty, proprty, dtestref, proprty1

ncells_i = num_i_cells(grid)       ! internal cells only
nfaces_i = num_i_faces(grid)       ! faces  = # cells + n_ghost
cell_imin = CELL_MIN_INDEX         ! includes ghost cells (0 or 1 - nghost)
cell_imax = cell_max_i_index(grid) ! includes ghost cells (ncells_i + nghost)

ncells_j = num_j_cells(grid)
nfaces_j = num_j_faces(grid)
cell_jmin = CELL_MIN_INDEX
cell_jmax = cell_max_j_index(grid)

sshk = ZERO

select case (comp)
case ( R_ )
   propty = ONE
case ( P_ )
   propty = ONE/GAMMA
case default
   call error2scr("improper shock location sense variable: must be p or rho")
```

```
end select

dtestref = fctrjmp * propty

do i = 1, ncells_i

   proprty = propty

   do j = ncells_j, 2, -1

      proprty1 = proprty
      proprty = grid%Q(comp,i,j)
      dtest = dtestref - proprty

      if ( dtest < -1.0e-6_RKIND ) then

         atest = dtest * ( s(i,j+1) - s(i,j) ) &
               / ( proprty1 - proprty ) + s(i,j)     ! interp shk s-value

         sshk(i) = atest / ( fsh * s(i,ncells_j) )   ! stretch/compression
                                                     ! factor

         !write(*, '(A, I, A, I, A, F8.3, A, F8.3)') 's(', i, ',', j, ') = ', s(i,j

         !write(*, '(A, F8.3, A, F8.3, A, F8.3, A, F8.3)') 'proprty1 = ', proprty1,

         exit

      end if
```

```
     end do

  end do

  !write(*, '(A)') 'sshk test completed'

  !

end subroutine shock_loc
```

A.2 Interpolation and Extrapolation Subroutine

```
!******************************  INTERPEXTR  *******************************!
! Interpolation/extrapolation subroutine to support align_shock
! Arguments:
!     xold, yold, xnew, ynew  ... x indep variable y dependent var, old to new
!     [old|new]low - low index to start in x...  [old|new]high
!     assumes x is increasing, indices are increasing from low to high
!*************************************************************************!
subroutine interpextr(xold, yold, xnew, ynew, oldlow, oldhigh, newlow, newhigh)

  implicit none

  integer :: i, j        ! counters
  integer, intent(in) :: oldlow, oldhigh, newlow, newhigh ! indicial extents
  integer :: oldlow2    ! temporary lower extent of old data....

  real(kind=RKIND) :: dxi ! denominator for xold difference
  real(kind=RKIND), dimension(:), intent(in) :: xold, yold, xnew
```

```
real(kind=RKIND), dimension(:), intent(inout) :: ynew

oldlow2 = oldlow

do i = newlow, newhigh

   if ( xnew(i) <= xold(oldlow) ) then    ! extrapolate low side

      dxi = ONE / ( xold(oldlow+1) - xold(oldlow) )
      ynew(i) = yold(oldlow) &
              - (yold(oldlow+1) - yold(oldlow))*dxi*(xold(oldlow) - xnew(i))

   elseif (xnew(i) >= xold(oldhigh) ) then ! extrapolate high side

      dxi = ONE / ( xold(oldhigh) - xold(oldhigh-1) )
      ynew(i) = yold(oldhigh) &
              + (yold(oldhigh)-yold(oldhigh-1))*dxi*(xnew(i)-xold(oldhigh))

   else                                    ! interpolate from low to high

      do j = oldlow2, oldhigh

         if ( xnew(i) < xold(j+1) ) then

            dxi = ONE / ( xold(j+1) - xold(j) )
            ynew(i) = yold(j) &
                    + (yold(j+1) - yold(j))*dxi*(xnew(i) - xold(j))

            exit
```

```
            else

               oldlow2 = oldlow2 + 1

            end if

         end do

      end if

   end do

end subroutine interpextr
```

Bibliography

1. Holden, M. S. and Wadhams, T. P., "CUBDAT Database v4.0," Database of Hypersonic Flows [CD-ROM], Calspan University of Buffalo Research Center, 2007.

2. McCourt, F. R., Beenakker, J. J., Köhler, W. E., and Kuščer, I., *Nonequilibrium Phenomena in Polyatomic Gases*, Oxford University Press, Oxford, 1990.

3. United States Air Force Scientific Advisory Board, "Report on Why and Whither Hypersonics Research in the US Air Force," Technical Report SAB-TR-00-03, United States Air Force, 2000.

4. "Honest Broker for Science and Technology, The", *Defense AT&L*, January–February 2007, pp. 2–11.

5. Moseley, G. T. M., "The Nation's Guardians: America's 21st Century Air Force," CSAF white paper, United States Air Force, December 2007.

6. Final Program, "Advancing the Science of Flight Technology," *46th AIAA Aerospace Sciences Meeting and Exhibit*, Reno NV, January 2008.

7. Berger, K. T., Greene, F. A., and Kimmel, R., "Aerothemodynamic Testing and Boundary Layer Trip Sizing of the HIFiRE Flight 1 Vehicle," *46th AIAA Aerospace Sciences Meeting and Exhibit*, Reno NV, January 2008, (AIAA-2008-640).

8. Staff, "U.S. Standard Atmosphere, 1976," Tech. rep., Government Printing Office, Washington DC, December 1976.

9. Bird, G. A., *Molecular Gas Dynamics and the Direct Simulations of Gas Flows*, Oxford University Press, Oxford, 1995.

10. Schwartzentruber, T., Scalabrin, L., and Boyd, I., "Hybrid Particle-Continuum Simulations of Non-Equilibrium Hypersonic Blunt Body Flow Fields," *9th AIAA/ASME Joint Thermophysics and Heat Transfer Conference*, San Francisco CA, June 2006, (AIAA-2006-3602).

11. Carr, R. W., *Quantifying Non-Equilibrium in Hypersonic Flows Using Entropy Generation*, Master's thesis, AFIT/GAE/ENY/07-M07, School of Engineering and Management, , Air Force Institute of Technology (AU), Wright Patterson Air Force Base OH, March 2007, (ADA468381).

12. Al-Ghoul, M. and Eu, B. C., "Generalized Hydrodynamic Theory of Shock Waves: Mach-Number Dependence of Inverse Shock Width for Nitrogen Gas," *Physical Review Letters*, Vol. 86, 2001, pp. 4294–4297.

13. Myong, R. S., "Eu's Generalized Hydrodynamic Computational Models for Nonequilibrium Diatomic Gas Flows," *40th Aerospace Sciences Meeting and Exhibit*, Reno NV, 2002, (AIAA-2002-0649).

14. Daso, E. O. and Blankson, I. M., "New Generalized Thermo-Fluid Dynamic Equations for Perfect, Real Gas, High Temperature, and Nonequilibrium Flows," *37th AIAA Aerospace Sciences Meeting and Exhibit*, Reno NV, 1999, (AIAA-1999-0417).

15. Chapman, S. and Cowling, T. G., *The Mathematical Theory of Non-Uniform Gases*, Cambridge University Press, London, 1952.

16. Balakrishnan, R. and Agarwal, R. K., "A Technique for Developing an Entropy-Consistent System of Second-Order Hydrodynamic Equations," *Rarefied Gas Dynamics: 22nd International Symposium*, edited by T. Bartel and M. Gallis, No. CP585, American Institute of Physics, 2001.

17. Bertin, J. J., *Hypersonic Aerothermodynamics*, American Institute of Aeronautics and Astronautics, Inc., Washington DC, 1994.

18. Moss, J. N. and Bird, G. A., "Direct Simulation of Transitional Flow for Hypersonic Re-Entry Conditions," *22nd Aerospace Sciences Meeting*, AIAA, Reno NV, Jan. 1984, (AIAA-1984-223).

19. Haile, J. M., *Molecular Dynamics Simulation: Elementary Methods*, John Wiley & Sons, Inc., New York, 1992.

20. Hicks, B. L., Yen, S.-M., and Reilly, B. J., "The internal structure of shock waves," *Journal of Fluid Mechanics*, Vol. 53, 1972, pp. 85–111.

21. Lumpkin, F. E. I., *Development and Evaluation of Continuum Models for Translational-Rotational Nonequilibrium.*, Ph.D. thesis, Stanford University, Palo Alto CA, March 1990, (SDIO/IST Army Research Office Contract DAALO3-86K-0139) (ONR/AFOSR/NASA Hypersonic Training and Research Grant NAGW-965).

22. Xu, K. and Liu, H., "Multiscale Gas-Kinetic Simulation for Continuum and Near-Continuum Flows," *Physical Review E*, Vol. 75, 2007, (16306).

23. Curtiss, C., "The Classical Boltzmann Equation of a Gas of Diatomic Molecules," *Journal of Chemical Physics*, Vol. 75, 1981, pp. 376–378.

24. Heck, E. L. and Dickinson, A. S., "Transport and Relaxation Properties of N_2," *Molecular Physics*, Vol. 81, 1994, pp. 1325–1352.

25. Alsmeyer, H., "Density Profiles in Argon and Nitrogen Shock Waves Measured by the Absorption of an Electron Beam," *Journal of Fluid Mechanics*, Vol. 74, No. 3, 1976, pp. 497–513.

26. Carnevale, E., Carey, C., and Larson, G., "Ultrasonic Determination of Rotational Collision Numbers and Vibrational Relaxation Times of Polyatomic Gases

at High Temperatures," *Journal of Chemical Physics*, Vol. 47, 1967, pp. 2829–2835.

27. Prangsma, G., Alberga, A., and Beenakker, J., "Ultrasonic Determination of the Volume Viscosity of N_2, CO, CH_4 and CD_4 Between 77 and 300 K," *Physica*, Vol. 64, 1973, pp. 278–288.

28. Belikov, A. E., Sharafutdinov, R. G., and Strekalov, M. L., "Temperature Dependence of the Rotational Relaxation Time in Nitrogen," *Chemical Physics Letters*, Vol. 231, December 1994, pp. 444–448.

29. Parker, J., "Rotational and Vibrational Relaxation in Diatomic Gases," *Physics of Fluids*, Vol. 2, No. 4, 1959, pp. 449–462.

30. Brau, C. and Jonkman, R., "Classical Theory of Rotational Relaxation in Diatomic Molecules," *Journal of Chemical Physics*, Vol. 52, No. 2, January 1970, pp. 477–484.

31. Vincenti, W. G. and Kruger, Jr., C. H., *Introduction to Physical Gas Dynamcs*, John Wiley & Sons, Inc., New York, 1967.

32. Truesdell, C., "The Present Status of the Controversy Regarding the Bulk Viscosity of Liquids," *Proceedings of the Royal Society of London Series A*, Vol. 226, 1954, pp. 1–69.

33. Graves, R. E. and Argrow, B. M., "Bulk Viscosity: Past to Present," *Journal of Thermophysics and Heat Transfer*, Vol. 13, No. 3, 1999, pp. 337–342, (AIAA-6443-440).

34. Meador, W. E., Miner, G. A., and Townsend, L. W., "Bulk Viscosity as a Relaxation Parameter: Fact or Fiction?" *Physics of Fluids*, Vol. 8, No. 1, January 1996, pp. 258–261.

35. Emanuel, G., ""Bulk Viscosity as a Relaxation Parameter: Fact or Fiction?"," *Physics of Fluids Comment*, Vol. 8, 1996, pp. 1984.

36. Cappelletti, D., Vecchiocattivi, F., Pirani, F., Heck, E., and Dickinson, A., "An Intermolecular Potential for Nitrogen from a Multi-Property Analysis," *Molecular Physics*, Vol. 93, No. 3, 1998, pp. 485–499.

37. Gilbarg, D. and Paolucci, D., "The Structure of Shock Waves in the Continuum Theory of Fluids," *Journal of Rational Mechanics and Analysis*, Vol. 2, 1953, pp. 617–642.

38. Gnoffo, P., Hartung, L., and Greendyke, R., "Heating Analysis for a Lunar Transfer Vehicle at Near-Equilibrium Conditions," *31st Aerospace Sciences Meeting and Exhibit*, Reno NV, 1993, (AIAA-1993-0270).

39. White, F. M., *Viscous Fluid Flow*, McGraw-Hill, New York, 3rd ed., 2006.

40. Rah, K. and Eu, B. C., "Analog of the Stokes-Einstein Relation for Bulk Viscosity," *Physical Review Letters*, Vol. 83, No. 22, November 1999, pp. 4566–4569.

41. Anderson, Jr., J. D., *Modern Compressible Flow: with Historical Perspective*, McGraw–Hill, New York, Third ed., 2003.

42. Heck, E., Dickinson, A., and Vesovic, V., "Second-Order Corrections for Transport Properties of Pure Diatomic Gases," *Molecular Physics*, Vol. 83, No. 5, 1994, pp. 907–932.

43. Sone, Y., *Kinetic Theory and Fluid Dynamics*, Modeling and Simulation in Science, Engineering and Technology, Birkhäuser, Boston, 2002.

44. Jeans, J. H., *The Dynamical Theory of Gases*, Cambridge University Press, London, 1904.

45. Boyd, I., Zhong, J., Levin, D. A., and Jenniskens, P., "Flow and Radiation Analyses for Stardust Entry at High Altitude," *46th AIAA Aerospace Sciences Meeting and Exhibit*, Reno NV, January 2008, (AIAA-2008-1215).

46. Bird, G., "Recent Advances and Current Challenges for DSMC," *Computers Math. Applic.*, Vol. 35, No. 1/2, 1998, pp. 1–14.

47. Carr, R. W., "Personal Communication," .

48. Lumpkin III, F. E., Haas, B. L., and Boyd, I. D., "Resolution of Differences Between Collision Number Definitions in Particle and Continuum Simulations," *Physics of Fluids A*, Vol. 3, No. 9, September 1991, pp. 2282–2284.

49. Wysong, I. J. and Wadsworth, D. C., "Assessment of direct simulation Monte Carlo phenomenological rotational relaxation models." *Physics of Fluids*, Vol. 10, No. 11, November 1998, pp. 2983–2994, (411525219981101).

50. Cheremisin, F. G. and Agarwal, R. K., "Computation of Hypersonic Shock Structure in Diatomic Gases with Rotational and Vibrational Relaxation Using the Generalized Boltzmann Equation," *46th AIAA Aerospace Sciences Meeting and Exhibit*, Reno NV, January 2008, (AIAA-2008-1269).

51. Wang Chang, C. and Uhlenbeck, G., "Transport Phenomena in Polyatomic Gases," Tech. Rep. CM-681, Engineering Research Institute, University of Michigan, Ann Arbor, MI, July 1951.

52. Park, C., "Rotational Relaxation of N_2 Behind a Strong Shock Wave," *Journal of Thermophysics and Heat Transfer*, Vol. 18, No. 4, October-December 2004, pp. 527–533, (AIAA-11442-279).

53. Hoffman, K. A. and Chiang, S. T., *Computational Fluid Dynamics*, Vol. II, Engineering Education System, Wichita KS, 2000.

54. Toro, E. F., Spruce, M., and Speares, W., "Restoration of the contact surface in the HLL Riemann solver," *Shock Waves*, Vol. 4, 1994, pp. 25–34.

55. Batten, P., Clarke, N., Lambert, C., and Causon, D. M., "On the choice of wavespeeds for the HLLC Riemann solver," *SIAM Journal of Scientific Computing*, Vol. 18, Nov. 1997, pp. 1553–1570.

56. Harten, A., Lax, P. D., and van Leer, B., "On Upstream Differencing and Godunov-Type Schemes for Hyperbolic Conservation Laws," *SIAM Review*, Vol. 25, No. 1, January 1983, pp. 35–61.

57. Blazek, J., *Computational Fluid Dynamics: Principles and Applications*, Elsevier Ltd, Kidlington, Oxford, Second ed., 2005.

58. Yoon, S. and Jameson, A., "Lower-upper Symmetric-Gauss-Seidel Method for the Euler and Navier-Stokes Equations," *AIAA Journal*, Vol. 26, No. 9, September 1988, pp. 1025–1026, (AIAA-0001-1452).

59. Xu, K., "A Gas-Kinetic BGK Scheme for the Navier-Stokes Equations and Its Connection with Artificial Dissipation and Godunov Method," *Journal of Computational Physics*, Vol. 171, 2001, pp. 289–335.

60. Camberos, J. and Chen, P., "Continuum Breakdown Parameter Based on Entropy Generation Rates," *41st Aerospace Sciences Meeting and Exhibit*, Reno NV, January 2003, (AIAA-2003-0157).

61. Kannenberg, K., Boyd, I., and Dietrich, S., "Development of an Object-Oriented Parallel DSMC Code for Plume Impingement Studies," *30th Thermophysics Conference*, San Diego CA, June 2001, (AIAA-1995-2052).

62. Nompelis, I., Candler, G. V., and Holden, M. S., "Effect of Vibrational Nonequilibrium on Hypersonic Double-Cone Experiments," *AIAA Journal*, Vol. 41, No. 11, November 2003, pp. 2162–2169.

63. De Groot, S. R. and Mazur, P., *Non-Equilibrium Thermodynamics*, Dover Publications Inc., New York, 1984.

Vita

Captain Abram E. Claycomb graduated from Jefferson County Open School in Lakewood, Colorado. He entered undergraduate studies at Rensselaer Polytechnic Institute in Troy, New York where he graduated with a Bachelor of Science Degree in both Aeronautical Engineering and Mechanical Engineering in May 2000. He was commissioned through Officer Training School at Maxwell Air Force Base in Montgomery, Alabama in February 2003.

His first assignment was at Tyndall AFB, Florida as F-16 avionics test engineer. He later completed flying requirements and was attached to the 85th Test and Evaluation Squadron as a flight test engineer. In September 2006, he entered the Graduate School of Engineering and Management, Air Force Institute of Technology. Upon graduation, he will be assigned to the Propulsion Directorate of the Air Force Research Laboratory.

REPORT DOCUMENTATION PAGE

Form Approved
OMB No. 0704–0188

1. REPORT DATE (DD–MM–YYYY)	2. REPORT TYPE	3. DATES COVERED *(From — To)*
27–03–2008	Master's Thesis	Jan 2007 — Mar 2008

4. TITLE AND SUBTITLE

Extending CFD Modeling to Near-Continuum Flows Using Enhanced Thermophysical Modeling

5a. CONTRACT NUMBER

5b. GRANT NUMBER

5c. PROGRAM ELEMENT NUMBER

6. AUTHOR(S)

Abram E. Claycomb, Capt, USAF

5d. PROJECT NUMBER

5e. TASK NUMBER

5f. WORK UNIT NUMBER

7. PERFORMING ORGANIZATION NAME(S) AND ADDRESS(ES)

Air Force Institute of Technology
Graduate School of Engineering and Management (AFIT/EN)
2950 Hobson Way
WPAFB OH 45433-7765

8. PERFORMING ORGANIZATION REPORT NUMBER

AFIT/GAE/ENY/08-M04

9. SPONSORING / MONITORING AGENCY NAME(S) AND ADDRESS(ES)

Dr. José A. Camberos, (937)
AFRL/RBSD Bldg 146, Rm 218, Wright-Patterson AFB, OH

10. SPONSOR/MONITOR'S ACRONYM(S)

11. SPONSOR/MONITOR'S REPORT NUMBER(S)

12. DISTRIBUTION / AVAILABILITY STATEMENT

APPROVED FOR PUBLIC RELEASE; DISTRIBUTION UNLIMITED

13. SUPPLEMENTARY NOTES

14. ABSTRACT

The constitutive relations found in traditional Navier-Stokes-based computational fluid dynamics solvers are known to be limited in altitude. The presence of nonequilibrium phenomena beyond what these methods are able to predict becomes more prevalent at higher altitudes, or increasing Knudsen number. The bulk viscosity, normally assumed to be zero in most computational fluid dynamics applications, is examined as a means of increasing the range of applicability of computational fluid dynamics. The bulk viscosity model used was from recent calculations available in the literature, from a new anisotropic potential energy surface, and is restricted to temperatures below 2000 K. The normal shock problem was solved for Mach numbers up to ten, using the bulk viscosity model. The bulk viscosity provided improvement in the agreement with observations of normal shock thickness for Mach numbers up to ten. Two axisymmetric, experimentally observed flows were solved with and without the bulk viscosity, and compared to DSMC solutions of a previous work. Improvement of surface heat transfer agreement with observation was found for a hollow-cylinder flare axisymmetric body. Improvement of separation point prediction was found for an axisymmetric double cone.

15. SUBJECT TERMS

Hypersonic Flow, Hypersonic Vehicles, Rarefied Gas Dynamics, Nonequilibrium Flow, High Altitude

16. SECURITY CLASSIFICATION OF:			17. LIMITATION OF ABSTRACT	18. NUMBER OF PAGES	19a. NAME OF RESPONSIBLE PERSON
a. REPORT	b. ABSTRACT	c. THIS PAGE			Dr. Robert B. Greendyke
U	U	U	UU	118	19b. TELEPHONE NUMBER (Include Area Code) (937) 255-3636, ext 4567; e-mail: Robert.greendyke@afit.edu

Standard Form 298 (Rev. 8–98)
Prescribed by ANSI Std. Z39.18